UNIVERSIDADE D
COIMBRA

André Marques Silva

DEVELOPMENT OF METHODOLOGIES FOR THE ANALYSIS AND DESIGN OPTIMIZATION OF AC ELECTRIC ROTATING MACHINES

Ph.D. Thesis in Electrical and Computer Engineering, specialization in Energy, supervised by Professor Doctor Fernando José Teixeira Estêvão Ferreira and co-supervised by Professor Doctor Carlos Alberto Henggeler de Carvalho Antunes, presented to the Department of Electrical and Computer Engineering of the Faculty of Sciences and Technology of the University of Coimbra.

December 2022

Development of Methodologies for the Analysis and Design Optimization of AC Electric Rotating Machines

FACULDADE DE
CIÊNCIAS E TECNOLOGIA
UNIVERSIDADE D
COIMBRA

André Marques Silva

Ph.D. Thesis in Electrical and Computer Engineering, specialization in Energy, supervised by Professor Doctor Fernando José Teixeira Estêvão Ferreira and co-supervised by Professor Doctor Carlos Alberto Henggeler de Carvalho Antunes, presented to the Department of Electrical and Computer Engineering of the Faculty of Sciences and Technology of the University of Coimbra.

December 2022

Declaration

I hereby declare that except where specific reference is made to the work of others, the contents of this dissertation are original and have not been submitted in whole or in part for consideration for any other degree or qualification in this, or any other university. This dissertation is my own work and contains nothing which is the outcome of work done in collaboration with others, except as specified in the text and Acknowledgements.

I hereby present my Doctoral dissertation which resulted from work carried from September 2018 to March 2022 under the supervision of Professor Fernando José Teixeira Estêvão Ferreira and Professor Carlos Alberto Henggeler de Carvalho Antunes. This work was supported financially by Fundação para a Ciência e Tecnologia under the fellowship SFRH/BD/137880/2018, and technically by Instituto de Sistemas e Robótica – Coimbra, Instituto de Engenharia de Sistemas e Computadores - Coimbra, and the Department of Electrical and Computer Engineering of the Faculty of Science and Technology of the University of Coimbra. The originality and scientific validity of my work is sustained by a series of conference and journal papers published during my doctoral studies. The preparation of other papers based on the research work reported in this thesis is underway, to be submitted to scientific journals or conferences.

André Marques Silva
December 2022

Acknowledgements

To my parents, family, and friends for their unconditional love and continuous support, without whom I would have never become who I am today.

A very special thanks is own to my supervisor Professor Fernando José Teixeira Estêvão Ferreira. It was a profound honor having met him back in 2015, when he introduced me to Electrical Machinery, the subject which led me to the position I am today and the reason for this document being presented to the academical world. Since then, we worked together uninterruptedly for many fruitful years and I will never make up for everything he taught me. Besides being technically sound, Professor Ferreira is an excellent person to work with, his excellent leadership attributes allowed me to go all this way through, keeping me always motivated and allowing my creativity to flourish.

Another also very special thanks is own to my co-supervisor Professor Carlos Henggeler Antunes. I will always remember the day when I asked him to be my supervisor, it was one week before the fellowship application deadline, nevertheless he immediately accepted and in no time he provided me the comments and suggestions which improved the research work I was proposing. And this is reason I suddenly started to admire Professor Antunes, as a reachable, relentless, and truly dedicated and methodical person. Without him I would have never discovered the magic of Metaheuristics, which is still fascinating me. I will never truly compensate the expertise he enlightened me.

I am also very thankful to Professor André Manuel dos Santos Mendes, who introduced me to electric machine finite element analysis and provided this research work the Altair-Flux simulation software, which was vital.

Finally, I would like to thank Continental Engineering Services for the recognition of my potential. I am truly realized in my first professional experience, as I am continuing the research work I was developing and materializing all my accumulated knowledge into the motors of the future.

At last but not least, I am deeply thankful for the financial support Fundação para a Ciência e Tecnologia granted me under the fellowship SFRH/BD/137880/2018.

Abstract

In recent years, concerns regarding resources availability, environmental preservation, and economical sustainability are motivating increasing research in electric machinery, since the electrification of crucial economic sectors, such as the transport and agriculture/industrial sectors. As a result, these new trends in traction applications place a great challenge on the electric machine design for cutting edge power/weight and volume ratios, overload capability, efficiency, operation range, sturdiness, reliability, and fault tolerance requirements. Hence, in high performance applications, the design analysis must address a wide range of operating regimes for the correct estimation of magnetic field saturation and eddy currents. Most common approaches are analytical methods, which allow for fast computation, but at costs of low accuracy; conversely, numerical based methods, such as the finite element method, can be very accurate, but at the expense of high computational complexity. As an alternative, the magnetic equivalent circuit is becoming more relevant in modern design trends, as it features an excellent compromise between accuracy and computational complexity.

In order to contribute with solutions to this relevant research topic, this thesis is dedicated to the study and development of novel general and comprehensive methodologies for the analysis and optimization at two different life stages of radial flux electric rotating machines.

On one hand, stator winding failures represent one of the most common failures in direct-on-line electric rotating machines. This machine component contributes the most for the Joule loss generation, magnetomotive force, torque, and power factor, which are highly related to the machine performance. Therefore, currently operating electric machines offer several efficiency improvement opportunities which may arise with repair/rewinding needs. For this reason, in this thesis, a novel comprehensive winding design strategy is proposed for a controlled and reduced airgap magnetomotive force spatial harmonic content, electrical resistance and copper utilization, and magnetizing flux level. The winding designs are obtained by an evolutionary algorithm, thus the objective functions and constraints of the optimization model can adapt with ease to achieve different performance goals. Experimental and simulation case studies demonstrate the relevance and applicability of the proposed methodology to promote energy savings and circular economy, by avoiding the acquisition of new machines. Moreover, the methodology can be massively adopted by technicians, as it

is computationally efficient and it requires readily available geometrical data, such as core radii, stack length, and rated electrical operation characteristics.

On the other hand, new challenges in high performance electric machine applications require cutting edge design optimization strategies since the early design stages, which are capable to investigate the optimal candidates suiting the performance requirements through many design parameters. Whenever finite element analysis fails to ensure convergence within a reasonable timespan, magnetic equivalent circuits become a preferable choice for the performance analysis of the candidates. For these reasons, a non-parametric magnetic equivalent circuit is proposed for a simplified and automatic mesh generation to cope with modern design optimization strategies. The proposed method is thoroughly validated for the three main electric rotating machine technologies: asynchronous induction, synchronous permanent magnet, and synchronous reluctance. Simulation results for motoring and generation operation are compared with finite element analysis. The proposed magnetic circuit displays a good compromise between accuracy and computational time.

Moreover, mesh refinements for accuracy improvements can be obtained by an increased number of tangential mesh elements. Then, methodologies for the topological optimization of different electric motoring technologies at early design conception are proposed. The aim of these optimization methodologies is to allow for the investigation of a very wide range of geometries, and, for this purpose, non-parametric design strategies are proposed. Additionally, a vast set of design decision variables is for the first time utilized to promote design comprehensiveness at every single component of the machine, from the stator and rotor geometries and airgap to the stator winding number of turns. The optimizations were conducted to maximize efficiency and power density, limiting the winding current to a maximum industrial grade current density. The resulting designs demonstrate the capability of the methodologies developed to generate high performance and diversified candidates, thus validating the proposed application as of most relevance for initial design concept studies.

Resumo

Atualmente, a investigação e desenvolvimento na área das máquinas elétricas é cada vez mais impulsionada pelas necessidades em sectores económicos relevantes, como o dos transportes, agrícola e industrial, devido à crescente preocupação com a disponibilidade de matérias-primas, sustentabilidade dos ecossistemas e económica. Como resultado, a transição das tecnologias de tração baseadas em motores de combustão para máquinas elétricas coloca novos desafios de projeto, nomeadamente ao nível de densidade de potência, capacidade de sobrecarga, eficiência, gama de operação, robustez e tolerância a falhas. Portanto, para aplicações de elevado desempenho, a análise eletromagnética da máquina elétrica, incluindo o cálculo adequado da saturação magnética e de correntes de Foucault, torna-se estritamente necessária para uma correta avaliação dos pontos de operação mais exigentes. As técnicas comuns para o projeto das máquinas são baseados em métodos analíticos, que permitem tempos de cálculo muito curtos, mas, em contrapartida, a precisão das grandezas eletromagnéticas avaliadas é insuficiente para a análise pretendida. Por outro lado, a análise numérica baseada em elementos finitos é muito precisa, mas o elevado tempo de computação necessário pode impossibilitar procedimentos sistemáticos de otimização. Os métodos baseados em circuitos magnéticos equivalentes estão a ganhar maior relevância no projeto moderno de máquinas elétricas, uma vez que oferecem um bom compromisso entre precisão e tempo de computação.

De modo a contribuir com soluções inovadoras para este relevante tópico de investigação, esta tese é dedicada ao estudo e desenvolvimento de novas metodologias de natureza abrangente para a análise e a otimização quer no projeto inicial quer durante o tempo de vida útil de máquinas elétricas rotativas de fluxo radial.

Por um lado, uma das componentes que mais contribui para falhas na operação de máquinas elétricas rotativas alimentadas diretamente da rede é o enrolamento estatórico, sendo também esta componente a que mais concorre para as perdas totais da máquina. Portanto, o momento de reparação/recondicionamento oferece uma excelente oportunidade de melhoria da eficiência da máquina elétrica rotativa. Neste contexto, nesta tese é proposta uma nova estratégia global de otimização de projeto de enrolamento para a minimização do conteúdo espacial harmónico da força magnetomotriz no entreferro, da resistência elétrica

e do peso do enrolamento. A estratégia desenvolvida utiliza um algoritmo evolucionário que permite que outros objetivos e restrições sejam facilmente definidos para a obtenção de outras características de performance desejadas. Os estudos de caso de experimentação e de simulação apresentados demonstram a relevância e aplicabilidade da metodologia desenvolvida, ao permitir o aumento da eficiência da máquina e a redução da quantidade de condutor necessária, promovendo a economia circular pela reutilização da máquina danificada ou obsoleta.

Por outro lado, os novos desafios colocados por aplicações de elevado desempenho requerem metodologias de otimização de projeto de ponta, a fim de permitir avaliar sistematicamente a topologia que conduz a maior densidade de potência e rendimento para um dado volume admissível. Para este objetivo, é necessário dotar o algoritmo de otimização de uma metodologia de análise eletromagnética de precisão e requisitos computacionais suficientes que permitam a avaliação correta da performance de um elevado número de candidatos num tempo admissível. Assim, é desenvolvida uma metodologia de desenho de um circuito magnético equivalente não-paramétrico para servir um algoritmo de otimização topológica. Esta metodologia foi validada pela comparação com análise de elementos finitos da simulação eletromagnética em regime de motor e gerador das três tecnologias principais de máquinas elétricas rotativas: assíncrona de indução, síncrona de ímanes permanentes e síncrona de relutância. O circuito magnético equivalente desenvolvido constitui um bom compromisso entre precisão e tempo computacional, podendo este compromisso ser ainda mais bem balanceado de acordo com o grau de definição da malha de relutâncias, tal como se um método de análise de elementos finitos se tratasse. Seguidamente, são propostas metodologias de otimização topológica de máquinas elétricas rotativas para uma fase de projeto inicial. O objetivo destas metodologias é permitir a investigação geral e quase universal de topologias geométricas ao nível do estator e do rotor para as diferentes tecnologias de motorização, e, portanto, as estratégias envolvidas utilizam preferencialmente métodos de desenho não-paramétricos. Os projetos obtidos demonstram a capacidade das metodologias em gerar candidatos admissíveis de elevada performance e promover diversidade de opções, validando, assim, a relevância da aplicação destas metodologias na fase de projeto inicial de máquinas elétricas rotativas de fluxo radial.

Contents

List of Figures

List of Tables

Nomenclature

List of Acronyms

AC	Alternating current
AEC	Analytical equivalent circuit
BDCM	Brushed direct current machine
BLDCM	Brushless direct current machine
CAD	Computer aided design
CPU	Central processing unit
DC	Direct current
DE	Differential evolution
DOL	Direct on-line
EA	Evolutionary algorithm
EEC	Equivalent Electric circuit
EMF	Electromotive force
ESS	Efficient set space
EV	Electric vehicle
FEA	Finite element analysis
FPGA	Field-programmable gate array
FSCW	Fractional-slot concentrated winding

FSW	Fractional-slot winding
GA	Genetic algorithm
GHG	Greenhouse gas
ISW	Integer-slot winding
MEC	Magnetic equivalent circuit
MMF	Magnetomotive force
MODE	Multiobjective differential evolution
MOGA	Multiobjective genetic algorithm
MOSA	Multiobjective simulating annealing
MST	Maxwell stress tensor
NASA	National Aeronautics and Space Administration
PAES	Pareto archived evolution strategy
PM	Permanent magnet
PMSM	Permanent magnet synchronous machine
PSO	Particle swarm optimization
RAM	Random access memory
SA	Simulated annealing
SCIM	Squirrel-cage induction machine
SI	Statistical Interpolation
SPEA	Strength Pareto evolutionary algorithm
SRM	Switched reluctance machine
SUS	Stochastic universal sampling
SynRM	Synchronous reluctance machine
THA	Time-harmonic analysis

THD	Total harmonic distortion
UNDX	Unimodal normal distribution crossover
VSD	Variable speed drive

List of Symbols

α	Arc of a magnetic equivalent circuit sector element	rad
ε	Electrical permittivity	F/m
γ	Permanent magnet angle of polarization	rad
Λ	Branch permeance	H^{-1}
μ	Magnetic permeability	H/m
μ_0	Vacuum permeability	$4\pi \cdot 10^{-7}$H/m
ω	Angular frequency	Hz
Φ	Magnetic flux	Wb
ρ	Electrical resistivity	Ω/m
σ	Maxwell stress tensor component, misalignment	
φ	Phase angle	rad
B	Magnetic flux density	T
D	Damping factor, number of decision variables, mass density	
E	Electromotive force	V
E_w	Winding phase electromotive force	V
f	Electrical frequency	Hz
G_m	Element magnetic permeance	H^{-1}
h	Height	m
h_s	Slot/tooth height	m
I	Current	A

I_0	Magnetization current	A
k_c	Eddy current iron losses coefficient	
k_{ewh}	End-winding height shape coefficient	
k_{ews}	End-winding flattening coefficient	
k_e	Excess iron losses coefficient	
k_h	Hysteresis iron losses coefficient	
k_{sff}	Slot fill factor	
k_w	Winding factor	
l	Length	m
L_{ew}	End-winding phase inductance	H
l_{ew}	Coil-side end-winding length	m
l_s	Core stack length	m
m	Number of phases	
N_{pp}	Number of winding parallel paths	
p	Number of poles	
P_{fe}	Iron losses	W
P_{in}	Motor input power	W
P_{mech}	Machine shaft power	W
$p_{p,eff}$	Effective number of pole pairs	
P_{pm}	Permanent magnet Joule losses (due to eddy currents)	W
P_{sl}	Stray load losses	W
P_{wj}	Winding Joule losses	W
q	Number of slots per pole and per phase	
R	Electrical resistance	Ω

r	Radius	m
r_{i}	Inner radius	m
R_{m}	Element magnetic reluctance	H^{-1}
S	Cross-sectional area	m^2
S_{slot}	Slot useful cross-sectional area	m^2
S_{wire}	Wire cross-sectional area	m^2
T_{em}	Electromagnetic torque	N.m
u	Instantaneous Voltage	V
V	Volume, voltage	m^3, V
v	Magnetic reluctivity	m/H
V_{m}	Magnetic scalar potential	A
w	Width	m
Z	Number of slots, teeth or slices	

List of Subscripts

0	Vacuum or free space
ag	Airgap
B	Rotor bar
b	Bottom
cgl	Cage layer
c	Eddy current
d	Design region
ER	Rotor end-ring
ew	End-winding
e	Excess

h	Hysteresis
m	Magnetic element
o	Slot opening
ph	Phase
pm	Permanent magnet
rml	Reluctance middle layer
r	Rotor, radial direction
s	Stator, slot, supply
t	Tooth, top
wnd	Winding
y	Yoke/Back-iron
θ	Tangential direction
z	Axial direction

List of Superscripts

(k)	Time step, iteration

List of Number Sets

$\mathbb{N}$	Natural
$\mathbb{Z}$	Integer

List of Operands

$\lceil\,\rceil$	Ceiling function
$\lfloor\,\rfloor$	Floor function
exp	Natural exponential function
mod	Remainder of the division function
Re{ }	Real part of a complex number

T	Transposed vector

Variables Presentation Method

$\mathbf{X}, \mathbf{x}$	Vector of quantity
$\widehat{x}$	Peak amplitude of a given quantity, unit vector
X, x	Quantity

Chapter 1

Introduction

1.1 Background

1.1.1 Historical overview of electric rotating machinery

The first electromagnetic motors were developed to operate on electrostatic field interactions. The first experiments were conducted by Benjamin Franklin in the 1740s, functioning on the principle of the Coulomb's law [1]. Such electrostatic interaction has only been mathematically described and documented a few years later, in 1785, by Charles-Augustin de Coulomb [2]. However, due to the difficulty of generating the high voltage necessary to create a practical force value, electrostatic motors were never used for practical purposes, being only used as academic demonstration apparatus or in micro-mechanical systems. In fact, modern electric motoring technologies rely on the magnetic field as the energy conversion medium. This becomes evident when comparing the physics definition for the stored energy in electric and magnetic fields. Hence, assuming the same field strength for both electric and magnetic fields in free space, it is possible to store $\mu_0/\varepsilon_0 \approx 142000$ more energy per volume in the magnetic than in the electric field.

Magnetostatic field experiments began with the invention of the electrochemical battery by Alessandro Volta, in 1799, which allowed the generation of steady electric currents. It was then a question of time for the first electromechanical devices starting to appear. Hans Christian Orsted discovered in 1820 that an electric current creates a magnetic field, which can exert a force on a magnet. By the time of this discovery, André-Marie Ampère in 1821 started to develop the first formulation for the electromagnetic interactions, which later resulted in the Ampère's force law [3]. The first demonstration of that effect with a rotary motion was demonstrated by Michael Faraday in 1821. While in 1822, Peter Barlow proposed the first motor solely operating on magnetostatic field interactions. The proposed

apparatus consisted of a suspended conducting disk partially submerged in a conducting liquid, which allowed a uniform and constant electric current to flow and interact with the magnetic field produced by a nearby permanent magnet, thus producing a constant force that forced the disk to rotate. This Barlow's wheel was an early demonstration of a homopolar motor which became practical late in the century. In order to achieve higher magnetic flux densities, the Hungarian physicist Anyos Jedlik introduced in 1827 the first electromagnetic coils. However, it was in 1828, that after solving the problem of continuous rotation with the invention of the commutator, Jedlik was able to propose the three main components of the practical brushed direct current (DC) motor known nowadays: the stator, the rotor and the commutator [4]. The first brushed DC motors, despite being able to power industrial machinery tools, were not financially practical, due to the high cost of the power batteries, as no electricity distribution system network was available at that time.

In the 1880s, many inventors were trying to realize workable alternating current (AC) generators to allow for electricity transmission at long distance to spark off the second industrial revolution [5]. The solution was thought more than a half century earlier, when in 1824 the French physicist François Arago envisioned the existence of rotating magnetic fields and, in 1879, Walter Baily demonstrated the first primitive induction motor. The first workable induction motor was invented by Galileo Ferraris in 1885. Later, an industrial grade version of an induction motor was developed by Nikola Tesla in 1887. Also in that year, Tesla published three patents for two-phase four-pole motor types: the first, was a non-self-starting four-pole synchronous reluctance motor; the second, a self-starting wound-rotor induction motor; and the third, a synchronous motor with separated DC excitation. Mikhail Dolivo-Dobrovolsky, who invented the three-phase induction motor in 1889, claimed that Tesla's motor was not practical because of the large torque pulsations inherent to the two-phase system, which prompted him to persist in his three-phase work. Owing to the success of Dobrovolsky designs, in 1891, the General Electric company promptly began to develop three-phase induction motors. In 1896, General Electric and Westinghouse signed a cross-licensing agreement for the bar-winding-rotor design, known today as the squirrel-cage rotor. Since then, exceptional engineering advancements allowed that, in less than a century, a 100 horsepower induction motor occupied the same volume as a 7.5 horsepower machine did back in 1897 [6].

1.1.2 Modern electric rotating machines

Many topologies of electric rotating machines have been proposed over the past decades and many of them were only realizable with the advent of modern power electronics. For many decades, the brushed DC machines (BDCM) with the mechanical commutator of the

rotor winding served many applications, comprising in the transportation sector. However, nowadays this technology has become obsolete due to demanding maintenance and relatively poor performance when compared to more recent technologies. Available since more than a century, the squirrel-cage induction machine (SCIM), which produces torque from induced currents in rotor bars, has established itself as the reference for simplicity, robustness, dynamic response, high efficiency and cost effectiveness. This machine can be operated direct online (DOL), which makes it the dominating motor technology in the industrial sector [7]. Operated by electronic drivers, the following list of machines is gaining more relevance as more challenging applications are now switching to electric power drive systems. Permanent magnet synchronous machines (PMSM) rely on magnets to produce a permanent rotor magnetic field which interacts with the field of the stator to produce torque. Therefore, since no power is necessary to excite the rotor field, these machines feature superior efficiency and torque/power density characteristics. The only major disadvantages of this machine are the magnets cost and scarcity, and the inherent demagnetization issues concerning temperature and current surges, which inevitably limit their range of operation. As an alternative, synchronous reluctance machine (SynRM) rely on a complex structure of reluctance paths in the rotor to produce reluctance torque. This no permanent magnet alternative outstands in simplicity, robustness and it has the possibility to become even more cost-effective than SCIMs. The major disadvantages are the high-torque ripple and relative lower power density when compared to PMSMs. Therefore, permanent magnet assisted SynRM with non-rare-earth magnets configurations are expected to significantly increase their market share over the next years, due to limited resources and cost fluctuation of the permanent magnet materials [8]. Trapezoidal current driven variations of the PMSM and SynRM machines, namely the brushless DC machine (BLDCM) and the switched reluctance machine (SRM), respectively, have been envisioned as more fault tolerant and fast response alternatives. In Table 1.1, a comparison of the main characteristics of the most common electric rotating machines is provided.

Electric rotating machines are mainly realized in a radial-flux configuration. In Fig. 1.1, the cross sections of the most common radial-flux electric rotating machines are shown. However, more recent designs are suggesting an axial-flux trend as a solution for applications demanding extremely high power density and efficiency characteristics [9]. This machine configuration can also include squirrel-cage, reluctance, or permanent magnet rotor configurations. The main advantages of axial-flux over radial-flux machines are: (i) the higher torque/power density capability (usually, single-sided rotor configurations are employed, however double-sided configurations are more fitted for high torque-to-volume requirements); (ii) the better thermal dissipation characteristics; (iii) very compact volume; and (iv) power up

Table 1.1 Comparison of the main characteristics of the most common electric rotating machines [8].

Indicator	**Machine type**					
	BDCM	SCIM	PMSM	SynRM	BLDCM	SRM
Acquisition cost	0	++	−	++	−	++
Maintenance cost	−−	++	+	++	+	++
Torque/power density	−	0	++	0	++	0
Efficiency	−	+	++	+	++	+
Manufacturability	++	++	0	++	+	++
Controllability	++	+	+	+	+	+
Reliability	−	++	+	++	+	++
Weight/Volume	−	+	++	+	++	+
Overload capacity	−	+	+	++	+	+
Robustness	0	++	+	++	+	++
Field weakening	++	++	+	++	−	++
Fault tolerant	+	++	−	+	−	++
Thermal limitations	0	+	−	++	−	++
Torque ripple/noise	−	++	++	−	0	−
Lifetime	−	++	+	++	+	++
Maturity	++	++	+	+	+	+

Note: '+' denotes advantage, '0' denotes neutral, and '−' denotes disadvantage. Motor technologies: BDCM as brushed DC machine; SCIM as squirrel-cage induction machine; PMSM as permanent magnet synchronous machine; SynRM as synchronous reluctance machine; BLDCM as brushless DC machine; and SRM as switched reluctance machine.

scaling can be easily achieved by stacking multiple machine stages axially. Moreover, in [10], a unique coreless axial-flux structure allowed for cutting-edge performance achievements, featuring extreme low weight and very high power density levels. The main disadvantages are of axial-flux machines are: (i) the high manufacturing cost; (ii) the low magnetization inductance, due to the relatively large airgap, which drastically reduces the machine power factor; (iii) the relatively higher cogging torque when compared to radial-flux configurations, since slot to pole ratio is low; (iv) the high radial and axial forces require stiffer bearings; and (v) the analytical simulations of this type of machines are very expensive, due to the 3-D characteristics of the active magnetic flux, thus making the design optimization much more difficult.

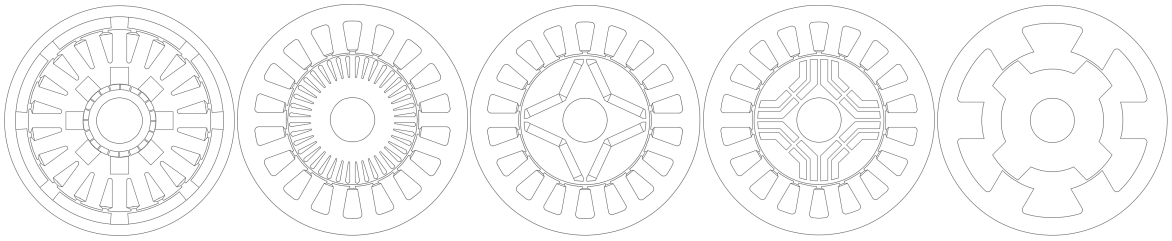

Figure 1.1 Cross sections of typical radial-flux electric rotating machines.

1.1.3 Technological roadmap - trends, opportunities and challenges

Environmental and economic challenges

Electric machinery has advanced significantly in the recent years, since a growing global preoccupation on climate change and greenhouse gases (GHGs) emissions is forcing governments to take actions into swiftly switch to less polluting and more environmentally sustainable energy conversion systems. Considering the global GHG emission contributions by sector displayed in Fig. 1.2, the upcoming challenges for a more sustainable future can be discussed.

Challenges and opportunities in the electricity generation sector

In all electrical energy generation processes, electric machines are the ultimate component in the chain, converting mechanical power, which usually resulted from a thermodynamic process, into electric power. The exception is the photovoltaic energy conversion, were electromagnetic energy is directly converted into electrical energy. Considering that global photovoltaic energy production is still below 5% of all electrical energy produced [12], thus the role of the electric rotating machinery in this sector is of paramount importance. Moreover, in heat production, gas is used as the primary energy source. This process account for a quarter of all global GHG emissions. However, not only due to environmental concerns, but also due to recent interruptions in gas and oil derivatives supply chains, it is inevitable and urgent an accelerated transition into heat pump systems, where also electric rotating machinery is a vital component.

Challenges and opportunities in the agriculture sector

The agriculture and forest sector roughly contributes for a quarter of all global GHG emissions. The electrification and digital transformation of this sector's major activities can

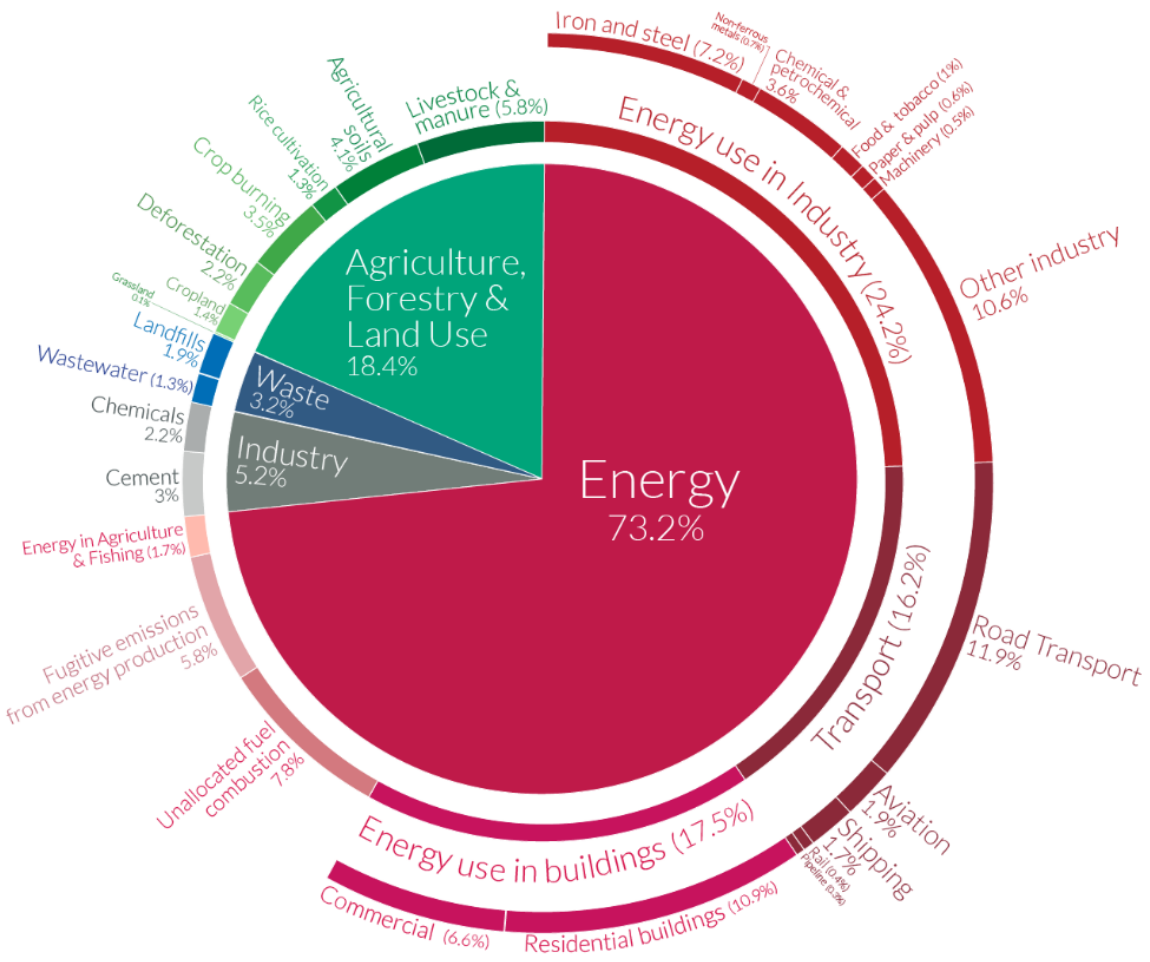

Figure 1.2 GHGs emissions by sector [11]. This is shown for the year 2016 - total global GHGs emissions were 49.4 billion tonnes CO_2 eq.

enable a better usage of space, higher production efficiency, lower utilization of fertilizers and pesticides, reduced waste and pollution, and higher farm profitability [13]. The agricultural machinery readaptation from internal combustion engines to hybrid or full-electric technologies is fundamental to enable this sector's digital transformation, owing to improved controllability, automatization, and efficient usage of resources. Many challenges related to electric machinery research and development are pointed out in [14]. The most relevant challenge is the power density related to the limited size available in hybrid technologies, which will still dominate, since full-electric solutions are still rare mainly due to energy storage limitations. Hence, as machines get smaller and the rated power increases, heat dissipation concerns make for the second design challenge, which generally can only be addressed by adopting novel liquid cooling solutions. Therefore, efficiency is also extremely important to cope with this issue. Hairpin winding configurations may be employed to

improve slot fill factor and reduce winding Joule losses. Last but not the least, another very important challenge in the design of the machine is the lack of representative duty cycles, due to the wide variety of operations. Especially, the torque requirement profile is usually very demanding and for some rated specifications it may lead the design out of size constraints. When this occurs, the machine design must exploit maximum torque density within the volume permitted and rely on short overload operation periods to fulfill specific torque demand. However, this overload capability makes even more complicated the thermal-electromagnetic management of the machine design process [14].

Challenges and opportunities in the industrial sector

The industrial activity accounts for 30% of all the global GHG emissions. GHG emissions in this sector result from burning fossil fuels for heating purposes, namely foundries and ceramics industries, as well as other emissions caused by certain chemical reactions for some products manufacturing. In terms of rated performance characteristics of the electric machinery currently in use, further significant technological advances for improved efficiency and emissions mitigation are unlikely, due to high technological maturity. Hence, achieving relevant efficiency improvements require reviewing all components of the industrial machinery as well as data collection and analysis for potential efficiency improvement opportunities.

With concern to electric rotating machinery solely, in industrial facilities electric motors are operating on average with a load factor of 60% [15]. Considering that most part of these electric motors are line-operated induction motors, the reasons for such reduced load factor can be related to the following: (i) manufacturers apply a significant safety margin to avoid any chances of motor driving inability; (ii) quite often, the motor real load operation profile can only be accurately known after the motor installation; (iii) even when the rated operation conditions are known, matching the manufacturers available offers may not be possible, due to discontinuities in the power range, hence a machine with a rated power level above the required is selected; (iv) in variable load applications, namely convoys, lifts, escalators, and pressers, even if the machine is well sized, partial load periods of operation may also be effectively long [16]. For such low load factor operation scenarios, induction motors are subject to a significant efficiency and power factor drop.

Immediate solutions are to control the machine with an electronic variable speed drive (VSD) or, once the real load operating conditions are known, to replace the oversized machine with a better fitted one. Nevertheless, both solutions may require a large financial investment.

The readaptation of a SCIM efficiency curve as a function of the load factor, as proposed in [16], is an effective and cheap solution to resize the machine and improve efficiency and power factor. This is achievable by modifying the machine average flux level in such a way

that on-site measured terminal voltage and load-cycle profiles are considered [17]. In strongly oversized SCIMs, by having the load factor below 40%, significant efficiency and power factor improvements can be obtained by simply modifying the connection mode from delta to star. For the other cases, flux adaption in DOL operated machines is achievable by modifying the winding pattern and/or the winding number of turns. In fact, replacing the winding of a machine is still an affordable solution, as its complete replacement may cost 30-50% the price of a new machine and no mounting adaptations are required because the same frame size is kept [16]. Since this strategy requires moderate investment and the resulting energy savings can be significant, it is particularly interesting for developing countries. Moreover, owing to the large number of winding failures in SCIMs with rated power above 4 kW which require replacement, this rehabilitation strategy can represent an excellent opportunity to improve circular economy and energy savings [16].

Challenges and opportunities in the transport sector

The transport sector accounts for 16% of all the global GHG emissions. The relevance of electric machinery in the electrification of this sector is substantial and the challenges ahead are of great complexity. The revolution already started. From 2016 to 2017, electric vehicle (EV) sales grew by 54% [18] and, in Europe, EV sales represented 19% of total car sales in 2021 [19]. It is estimated that there could be over 200 million EV sales by 2030 [20]. As a result of such dissemination of electric mobility, the total GHG emissions of this sector can be reduced up to 75% by 2050 [21]. Despite the high degree of maturity of electric rotating machinery, very specific and challenging performance characteristics of the electric propulsion require further research and development, namely (i) very high torque/power density characteristics; (ii) the high overload power that the propulsion system must be able to deliver for a wide speed range; (iii) the high torque capability at low speed for starting and climbing periods; and (iv) the high power at high speed for cruising [22].

In the aviation sector, considering the propulsion technologies currently available, the perspectives of efficiency improvements for further environmentally and economically sustainable changes are plateauing out. The electrical transformation of the current propulsion systems is the most promising disruptive technology to address the required changes. Excluding the development of enhanced electrical energy storage systems, which is by far the most difficult technological leap necessary to accomplish the transition, achieving the necessary cutting edge electric machine performance levels require to solve complex research and development topics as well. NASA Research Announcement set minimum performance requirements of MW-class machines featuring power densities above 13 kW/kg and efficiency greater than 96% in the next decade for the non-cryogenic segment [23]. In [23], a list of

the most promising non-cryogenic opportunities for significant performance improvements concerns novel materials, such as enhanced conductive and low weight carbon nanotubes for the windings, composite materials embedding hard and soft magnetic materials for low loss and lighter lamination, and higher remanence flux nanocomposite magnetic materials. Moreover, a multidisciplinary optimization of the complete propulsion system is of paramount importance for efficiency and power density maximization.

1.1.4 Design trends and challenges in electric rotating machinery

The first design stage of an electric rotating machine includes the complete reviewing of the requirements and the selection of the most appropriate tools and methodologies to assist the design and guarantee the fulfillment of the required performance characteristics. Depending on the application, the design process may be completely different, for example when comparing the industrial and propulsion motoring applications, where the first mostly operates at rated speed and torque. Therefore, for the most demanding applications, cutting-edge design methodologies are equally required.

When designing a machine, usually the targets are to realize it as more compact, efficient, and economical as possible. Achieving these goals simultaneously is not possible in general, since power is proportional to size and larger volumes are equally more expensive. Hence, the delicate trade-off between power density, efficiency, and size/weight require advanced technical expertise and the following topics are generally considered:

- The selection of materials is critical for the machine performance characteristics; and high performance materials will cost more and often they arise other design concerns. For instance, amorphous electrical steel features extremely low iron losses; however, it saturates earlier, it is mechanically more fragile, and its lamination is generally very thin, which increases manufacturing difficulty [24]. Additionally, high energy density permanent magnets, such as neodymium magnets, are more susceptible to temperature than other materials, as energy reduces drastically and sharply at relatively lower temperatures [25]

- Increasing the electric machine power density is usually achievable by increasing the rotational speed. However, for a given speed, the machine terminal voltage reaches the variable speed driver (VSD) nominal voltage and from this operating point on, torque capability is reduced and no or very little power is further produced. This flux-weakening limitation is usually tackled by injecting a demagnetizing current, which places additional preoccupations concerning permanent magnet demagnetization,

additional winding losses, and raises the current capability requirement for inverter sizing

- Improving torque capability generally requires higher current density and, at the most challenging scenario, the selection of an electrical steel grade with higher magnetic flux density saturation. Higher current density levels significantly increase the winding Joule losses. The adoption of solid rectangular-section wires, commonly known as hairpin winding, has been introduced in high power density machines, due to the possibility to achieve slot fill factors up to 0.7, when usually stranded winding topologies only achieve slot fill factors below 0.5. This superior slot fill factor reduces the winding Joule losses by featuring a lower DC resistance. Nevertheless, special care should be taken in order to avoid relevant parasitic AC Joule losses, due to eddy current effect in the conductors. This drawback is usually mitigated by employing multiple strands of insulated wires and by curling them [26]

- Considering the envelope performance characteristics of a design is essential to ensure the application feasibility. However, when designing the machine, it is equally necessary to optimize efficiency at low torque/power operation to promote enhanced overall energy savings. This is especially relevant in propulsion applications, where a very wide operation range is expected, and by allowing overall minimal energy loss the machine cooling management system may also be more compact.

- The development of new materials and new techniques for the manufacturing of electric rotating machines is of paramount importance. High performance and high power density machines employ rare-earth materials, which are mainly available in China. Therefore, there are strong strategical and political reasons to promote research on rare-earth-free motor designs [27]. Novel additive manufacturing techniques enable more efficient thermal solutions to be implemented, for example by allowing the manufacturing of complex thermal management structures, which by traditional means are difficult or even impossible to achieve, thus admitting higher power density levels to be unlocked [28].

1.1.5 Electromagnetic modeling strategies

Machine modeling is certainly the most important design tool. The ideal numerical model should be time-efficient and accurate. Additionaly, it should consider relevant physical characteristics, such as magnetic nonlinearity and eddy current effect, as well as to provide detailed field information for torque and iron losses computation. The three most common

modeling approaches are analytical equivalent circuit (AEC), finite element analysis (FEA), and magnetic equivalent circuit (MEC).

Analytical models were introduced in the 1970s and supported many design optimization efforts for many years afterwards [29]. Their wide adoption owed to simplicity and the low computational requirements. Machine parameters and performance characteristics, such as magnetization inductance, leakage flux inductances, input power, torque and winding Joule losses are calculated based on the airgap average magnetic flux density. These methods neglect the magnetic saturation, the eddy current effect in the conductors, the iron losses, and the local leakage flux paths are coarsely estimated. Thus, the accuracy of AEC models is relatively low. Moreover, modern design trends deal with complex geometrical characteristics, which limits the applicability of these methods due to their inherent inability to consider such detailed structures [30–32]. As a result, despite being a very computational efficient analysis tool, AEC models cannot delivery enough accuracy to cope with modern design optimization trends [33–36].

In the opposite case, FEA is the most accurate numerical method for modeling electric machines [31, 37]. It has been widely adopted in design optimization applications, since it outperforms any other modeling method in terms of accuracy. However, it requires very high computational resources, especially when 3-D simulations are carried out. Therefore, this model method is mainly used in final designs validation or in design refinement processes, where the number and range of design parameters is rather small [8]. The accuracy of the method is highly dependent on the geometrical discretization of the device, where a coarser meshing results in lesser accuracy, but higher computational speed, while a finer meshing results in higher accuracy, but lower computational speed. Usually, a finer mesh is adopted in high gradient flux regions, such as airgap and tooth tip regions, and a coarser mesh is employed in back-iron and teeth regions. In this way, a more efficient model allows for memory and computational time savings, while maintaining high accuracy. Moreover, FEA effectively takes into account the eddy current effect by embedding its mathematical description in the global system of equations [38]. Therefore, the resulting magnetic flux takes into account the contribution of eddy current effects.

Conversely, MEC models are a good compromise between the high accuracy of FEA and the low computational time of AEC models. Developed in the beginnings of the past century [39], the method was then adapted into a computer based application for the analysis of electric rotating machines in the 1980s [40]. The method discretirizes the machine geometry into a mesh/network of simpler shaped elements, which concentrate the permeance characteristics of each shape. Unlike FEA, where node-based vector magnetic potentials allow for the magnetic flux to point to any direction within an element, in traditional MEC

methods the flux can only flow within one flux tube. However, with the introduction of bidirectional elements [41], improved accuracy and mesh flexibility was possible in MEC models. Depending on mesh characteristics, magnetic nonlinearity and flux leakage characteristics can be accurately modeled by MEC methods. Unlike FEA, eddy current effects cannot be easily included without significantly increasing the complexity of the model, since the magnetomotive force formulation and geometrical characteristics of the elements do not support the induction of eddy currents [8]. Likewise, nonlinearities within MEC are not always possible to be solved with accelerated convergence algorithms such the Newton-Raphson method. In fact, only unidirectional element based MECs or Kirchhoff mesh law based solvers can support the definition of the Newton-Raphson Jacobian matrix [42]. For the other cases, fixed-point iterative solvers may be used [43], which in general require more computational time to converge.

Table 1.2 summarizes the advantages and disadvantages of each method from a design optimization application perspective.

Table 1.2 Comparison of the main characteristics of the most common electric rotating machine modeling methods.

Criterion	**AEC**	**FEA**	**MEC**
Simplicity	$++$	$--$	0
Computational resources	$++$	$--$	$+$
Accuracy	$--$	$++$	$+$
Iron loss modeling	$--$	$++$	$++$
Eddy current modeling	$--$	$++$	0
Design optimization applicability	$+$	$++$	$++$

Note: '$+$' denotes advantage, '0' denotes neutral, and '$-$' denotes disadvantage; additionally, (AEC) analytical equivalent circuit, (FEA) finite element analysis, and (MEC) magnetic equivalent circuit.

1.1.6 Multiobjective optimization with evolutionary algorithms

Solving such complex optimization problems requires very efficient optimizers capable of generating optimal (nondominated) solutions with a reduced number of objective function(s) evaluations and low computational effort needed [44]. Mathematical programming algorithms and metaheuristics (and even hybrid approaches) have been proposed in the literature to search for optimal solutions (in single objective model) and nondominated solutions (in multiple objective models). These approaches may be deterministic (when data can be obtained in a relatively precise manner) or stochastic (attempting to cope with uncertain

data). Metaheuristics generally involve some stochastic techniques to cope with very large, nonlinear and/or combinatorial search spaces, with the aim to avoid the search process to be trapped in local optima/nondominated solutions by balancing search exploration (diversification) and exploitation (intensification) procedures. Metaheuristics can be tailored to solve any type of optimization problem, even not requiring a complete mathematical model of the problem, featuring a high level adaptive search space procedure in combination with low level heuristics tailored to the characteristics of the problem. These features allow for very complex multiobjective and constrained nonlinear problems to be addressed, using randomly guided mechanisms, which expectedly converge into optimal or near-optimal (-nondominated) solutions. Metaheuristics serve three main goals: to solve problems faster, to solve large problems, and to be simple to design and implement [45]. Metaheuristics can be either population-based methods, which is the case of well-known algorithms such as: Differential Evolution (DE), Particle Swarm Optimization (PSO), Genetic/Evolutionary Algorithms (GA/EA), or single-point based methods, which is the case of Simulated Annealing (SA) or Tabu search.

Population-based methods consist of a set of individuals, each one representing a potential solution to the problem being optimized. Very commonly, this kind of evolutionary algorithms are bio-inspired [45]. In [46], a comparative study of the performance of population-based metaheuristics, namely DE, PSO and a custom EA, is carried out on numerical benchmark problems. The results showed a clear overall best performance of DE, while the proposed EA only outperformed the DE algorithm in noisy problems. Nevertheless, DE was able to reproduce the same results consistently over many runs, which means less dependency on the random initialization. Conversely, in the PSO algorithm a high dependency on the initial population and the algorithm parameterization was observed; however, it was always the fastest algorithm, despite requiring several runs to ensure convergence.

Single-point based techniques, such as SA, are also well-established metaheuristics that, for some problems, may outperform population-based techniques. In [47], a novel multiobjective SA algorithm (AMOSA) is proposed. AMOSA employs an archive to store nondominated solutions and the concept of amount of domination is introduced. The results are compared with other well-known EA, namely NSGA-II [48] and PAES [49]. A set of complex benchmark problems, for two and three objectives, was used for performance comparison purposes. The AMOSA showed the overall better performance in a series of optimization benchmark problems compared to other EA.

1.2 Research motivation and targets

As previously mentioned, the accelerated electrification of several sectors is pushing forward the performance requirements expected in electric rotating machinery. In order to cope with these new challenges in design, in this Thesis, novel strategies are investigated for the analysis and design optimization of electric rotating machine at two different life-cycle periods: one for repair/rewinding opportunities and the other for the design stage.

In a repair/rewinding perspective, significant efficiency improvement opportunities in the machines already in use can be taken, especially in the industrial sector as it has been previously referred to, by redesigning the stator winding to match a desired average airgap magnetic flux density. In this Thesis, general muliphase and multilayer winding design optimization strategies are investigated and implemented to further improve efficiency by reducing end-winding volume, thus reducing phase resistance and conductor material cost; and by attenuating magnetomotive force spatial harmonic content, leading to lower iron and stray load losses.

From a design concept stage perspective, taking into account the challenges ahead that will require enormous research efforts to develop new cutting-edge design optimization strategies, this thesis addresses novel general electromagnetic design optimization methodologies which manipulate a very wide range of machine parameters. For these purposes, first, a state-of-the-art magnetic equivalent circuit for the electromagnetic analysis of electric machines, featuring high computational-speed and accuracy, is investigated and implemented. Then, novel design strategies for wide topological replication range of squirrel-cage, salient pole, air-barrier/slit, and air-barrier/slit permanent magnet assisted rotor configurations are investigated and implemented.

A specially tailored metaheuristic demonstrating outstanding convergence and computational efficiency characteristics developed and implemented in the optimization scenarios tackled herein.

All methodologies developed within the scope of this Thesis are intended to be disseminated through software applications and/or software frameworks freely provided in online code hosting platforms for replication purposes.

1.3 Thesis structure

This document is organized in five chapters. In this introduction chapter the research background, motivation and aims of the Thesis are presented. The next chapters start with an introductory section referring to a survey of the state-of-the-art contributions of the related

research field, the main contributions are presented, including experimental and simulation case studies for validation purposes, and they finalize with a summary comprising the chapter main conclusions.

In chapter 2, the development of a general multiphase, multilayer winding design optimization methodology is proposed for machine efficiency improvements by attenuating the airgap magnetomotive force spatial harmonic content and the end-winding electrical resistance. The proposed methodology is validated using an experimental case study where a three-phase single-layer regular winding is compared with a multilayer optimized winding. Additionally, in a six-phase multilayer winding case study, a comparison by means of FEA of the optimal solution of the proposed strategy with an optimized winding design proposed in the literature is provided.

In chapter 3, a non-parametric MEC for a fast and accurate electromagnetic analysis of electric machines is developed. The most relevant contributions of the proposed reluctance network are the trapezoidal sector shaped element, the airgap permeance function, and the multiple rotor bar model. The method is thoroughly validated through 2-D FEA comparison of a SCIM, PMSM, and SynRM technologies, including time-harmonic and time-step analyses. Moreover, a vast collection of relevant electromagnetic quantities for design optimization purposes, such as efficiency, shaft power, shaft torque, power factor, iron losses, permanent magnet eddy current losses, and winding Joule losses is provided for a complete and robust assessment of the proposed method. This research work lays the foundations of chapter 4.

In chapter 4, general parametric and non-parametric topological optimization methodologies are developed for the design of electric rotating machines. The proposed topological optimization strategies are a non-parametric bar design strategy for the rotor of SCIMs, a non-parametric salient pole design strategy for the rotor of SynRMs, and a non-parametric air-barrier design strategy for the rotor of SynRMs and PMSMs. The stator configuration for all these technologies is obtained by a parameterized parallel slot design strategy. The same differential evolution algorithm developed in chapter 2 was employed to solve this chapter's optimization problems. A case study including the topological optimization of the SCIM simulated in chapter 3, and a case study comparing the topological optimization of the three motor technologies analyzed are presented for validation purposes. The performance of the optimized machines have been validated through 2-D FEA.

In chapter 5, the main conclusions of this Thesis are drawn and proposals for future work in this research field are provided.

In appendix A, the algorithms developed to solve the optimization problem of chapter 2 are explained in detail and the justification for the adoption of the DE algorithm as the

optimization solver is supported by the performance comparison in the case study provided in the final section of this appendix.

Chapter 2

Winding Analysis and Optimization Methodologies

2.1 Introduction

The armature winding can be considered one of the most import components of an electric rotating machine, owing to the largest loss share and the impact on the quality of the torque produced. Ideally, it would create a pure sinusoidal MMF traveling through the airgap region to produce rippleless torque and its whole conduction length would produce active magnetic flux. This ideal winding would only exist for an infinite number of slots and phases. Given the impossibility to manufacture such winding, many works in the literature have investigated novel constructions to cope with the ideal features of a rotating-field winding and manufacturing limitations.

From a design perspective, a winding consists of the connection of the conductors assigned to the different slots of the stator and the final connection of the whole arrangement to the electric power supply. Generically, these connections define the decision variables set of the winding design, whose performance goals very often aim at a sinusoidal MMF. Therefore, the most common objective of winding design techniques is related to the suppression of MMF harmonic components, as this harmonic distortion is directly associated with torque ripple, mechanical vibration, acoustic noise, iron losses, stray-load losses, localized saturation, and non-sinusoidal back electromotive force (back-EMF) [50–53]. Recently, many contributions for the improvement of the winding design have been proposed to cope the more and more exigent performance requirements, forcing manufacturers to strive for optimization opportunities at every design detail of the machine.

Traditionally, methods for the attenuation of the MMF space harmonic content include the selection of a higher number of slots per pole and per phase (q) and/or the adoption of multilayer short-pitched/chorded winding configurations [54, 51, 55, 56] (Fig. 2.1). The first method is by far the most effective, as it does not only reduce the low-order harmonics, but it also attenuates the effect of the harmonic components due to the slotting effect, which includes harmonics of order $2k \cdot Z_s/p \pm 1$ and amplitude equal to the fundamental component divided by the harmonic order, where $k \in \mathbb{N}$, Z_s is the stator number of slots, and p is the number of poles. The second method is particularly effective in the attenuation of specific low-order harmonics, but the fundamental winding factor is also significantly attenuated, while other harmonics may even be magnified. Moreover, any additional layer beyond the single-layer configuration requires additional insulation concerns, which increases the cost and the manufacturing complexity of the winding.

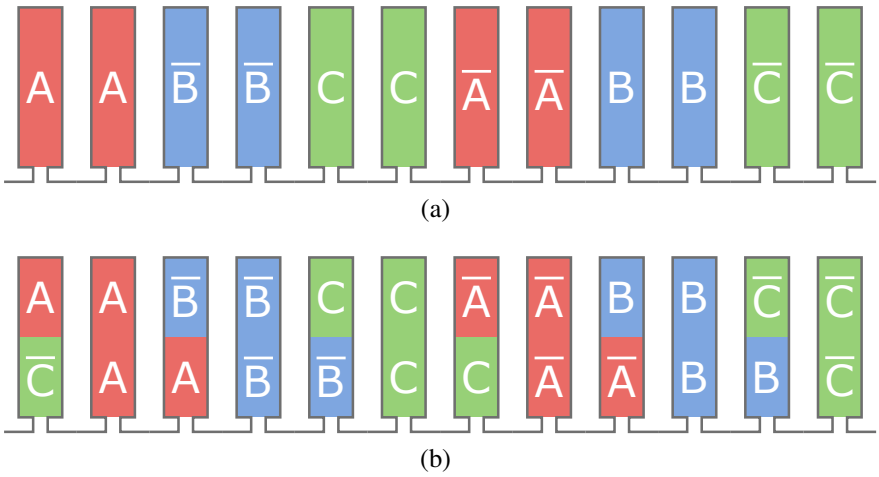

Figure 2.1 Three-phase 12-slot and 4-pole: (a) single-layer winding configuration; (b) double-layer 60 degrees (one slot) chorded winding configuration. The over-line represents a returning conductor set.

Multiphase winding configurations have become more relevant to this subject, offering not only the advantages related to a more sinusoidal MMF waveform, but also the benefits regarding increased fault-tolerance capabilities and lower current rating per phase, which are appealing characteristics for high power density and redundancy applications [57–64]. Depending on the displacement between phases or subsets of phases, the multiphase winding configurations are referred to as symmetric, if the displacement between any two consecutive phases is equal, or asymmetric otherwise. When comparing both configurations, asymmetric winding designs offer more opportunities for the elimination of certain MMF harmonic orders [65–67].

Techniques incorporating both multilayer and multiphase winding configurations have recently been proposed for improved power density, efficiency, torque ripple, fault tolerance capability, and flux weakening performance. The stator-shift concept proposed in [68–71] employs two identical windings shifted by an electrical angle, which is denoted as the shift-angle (Fig. 2.2). During the combination of the two stators, the slots of one stator may overlap the other stator slots; in this case, the resulting number of slots/teeth of the stator is maintained, for all the other cases the number of slots doubles and uneven tooth widths may occur. Either way, the number of coils doubles and both winding sets must be connected in series. The whole concept of the stator-shift aims at reducing the MMF spatial harmonics. However, the effect of localized magnetic saturation should be accounted for when the stator-shift produces unequal tooth widths, thus preventing counterproductive results. Moreover, the same principle of the stator-shift can be applied to the different phases of a winding. In this case, the phase-shift concept, as proposed in [72], is applied to possible asymmetrical winding configurations by manipulating the displacement between the winding subsets of each phase. Likewise, the whole concept of the phase-shift aims at reducing the MMF spatial harmonics.

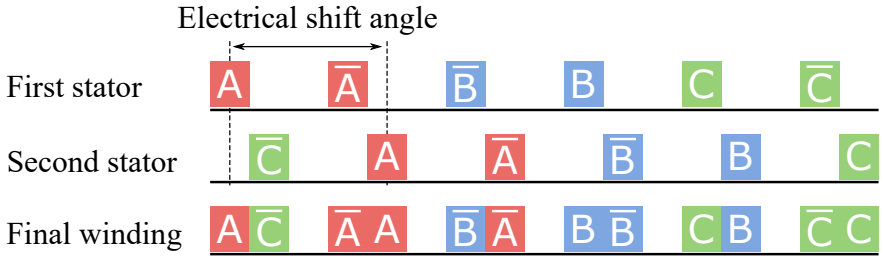

Figure 2.2 Stator shift concept - the final winding design results from two identical single-layer winding configurations shifted by an angle.

From a different and unusual perspective, the same low MMF harmonic content goal can be attained by disaggregating the phase-belts of a winding (Fig. 2.3). The resulting winding configurations are referred to as interspersed [73–76]. The technique consists of interchanging each coil-side of one phase-belt with the corresponding coil-side from the adjacent phase-belt and repeating this cyclic interchange throughout the whole winding [73]. Instead of symmetrically interchanging the coil-sides of two layered phase-belts the top and bottom coil-sides can be interchanged separately [76]. Another possibility consists of doubling the given number of layers of a winding and shifting the two halves, series connected, by a given number of slots [74].

The previous techniques mentioned so far only deal with equal number of turns per coil. Conversely, unequal turn patterns increase the number of design variables for enhanced and

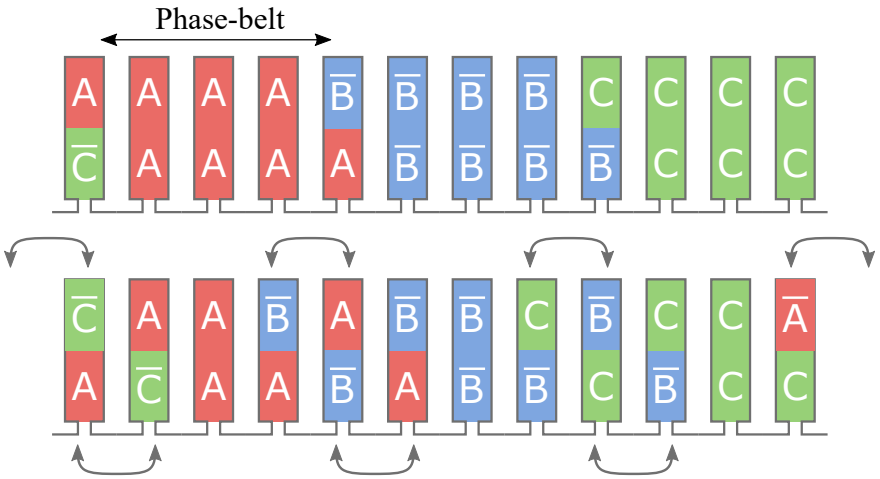

Figure 2.3 Three-phase 24 slot, 4 pole interspersed winding construction example with only the phase-belt tips interchanged.

more compact winding solutions with low MMF spatial harmonic content [77–89]. The combination of multilayer winding configurations with unequal turns per slot enables novel solutions for the minimization of the eddy current losses in permanent-magnets [79–81, 86–88], and the winding resistance [82–84]. Another research avenue combines unequal turn patterns with uneven tooth widths to further reduce the THD of the airgap MMF, allowing for the attenuation of the MMF harmonic components due to the slotting effect [77, 78]. However the effect of the magnetic nonlinearity is disregarded.

Such complex optimization formulations require efficient optimization solvers, including deterministic and stochastic algorithms, to deal with multiple objective functions for which solutions are computed through aggregation (scalarizing) methods (such as optimizing weighted-sum of the objectives or minimizing the distance to a reference design) or using the nondominance (Pareto optimality) concept [45]. In [79], a quadratic programming approach is used to maximize the airgap MMF fundamental term and minimize the total rotor losses of multilayer fractional-slot concentrated winding configurations (FSCW) PM machines. In [78], the winding design is optimized by minimizing the MMF total harmonic distortion (THD) and maximizing its fundamental term, by means of a multiobjective genetic algorithm. In [85], a particle swarm algorithm is specifically tailored for the minimization of the MMF and the EMF THD values through a weighted sum of the objectives, with constraints applied to limit the maximum MMF THD and increased current. In [82–84], a genetic algorithm is employed for the weighted sum minimization of the MMF THD and phase resistance, with constraints establishing a minimum value of the MMF and a maximum value of end-winding phase resistance.

All mentioned works propose novel solutions for specific applications. Despite the relevance of these contributions, it has never been verified whether for the given slot, pole, and phase combinations the proposed winding configurations are unequivocally the best. Therefore, the development of a more general design methodology is fundamental to strive for additional performance levels and material costs control, which are becoming more difficult to achieve. This problem is only tackled in [82–84], where the authors propose a general decision variable matrix to allow for an optimizer to design any multilayer symmetric winding. However, the end-winding connections are fixed, thus limiting the variety of solutions.

For this reason, in this chapter, a framework encompassing a range of different optimization techniques presented in literature was developed, resulting in a unified winding design optimization methodology. Increased generalization is achieved through a convenient set of design variables, covering multiphase symmetric and asymmetrical configurations for improved sinusoidal MMF of any slot, pole, and phase combination, as well as an iterative mechanism for the selection of shorter end-winding connections, these unique features will enable new opportunities for further diminishing the winding resistance and manufacturing material.

2.2 A general winding design methodology

2.2.1 General mathematical modeling of a winding

The AC winding theory recognizes three winding configurations based on the number of slots per pole and per phase. Thus, an integer q defines the class of integer-slot winding configurations (ISW), a $q > 1, q \notin \mathbb{N}$, defines the fractional-slot winding configurations (FSW), and a $q < 1$ determines the fractional-slot concentrated winding configurations (FSCW). As an example, Fig. 2.4a shows a 18-slot, 2-pole and three-phase ISW, Fig. 2.4b shows a 18-slot, 4-pole, three-phase FSW, and Fig. 2.4c shows a 18-slot, 8-pole, three-phase FSCW.

Commonly, two end-winding connection patterns are identified based q: (i) distributed, where the coil-pitch usually spans more than one slot-pitch, which is the case for the ISW and the FSW configurations; and (ii) concentrated, where coils are usually wound around the stator teeth, which is the case for the FSCW configuration. For distributed winding configurations, the winding can assume two additional patterns: (i) imbricated pattern, where the coil-pitch is uniform; (ii) concentric pattern, where different coils share the same geometrical center, but have different coil-pitches.

A winding of series-connected coils can be conveniently represented in a matrix form. For a core with Z slots, the in-slot coil-side pattern of a winding with m phases can be mathematically described by

$$\mathbf{N} = \begin{bmatrix} n_{1,1} & n_{1,2} & \dots & n_{1,Z} \\ n_{2,1} & n_{2,2} & \dots & n_{2,Z} \\ \vdots & \vdots & \ddots & \vdots \\ n_{m,1} & n_{m,2} & \dots & n_{m,Z} \end{bmatrix}, n_{i,j} \in \mathbb{Z}, \tag{2.1}$$

In each element of $\mathbf{N}$, the positive or negative values define of n the respective coil-side number of conductors in series and their polarity, while a zero value means no coil-side. For slotless machines [90, 91], Z corresponds to the resolution of the MMF defined by a desired number of slopes.

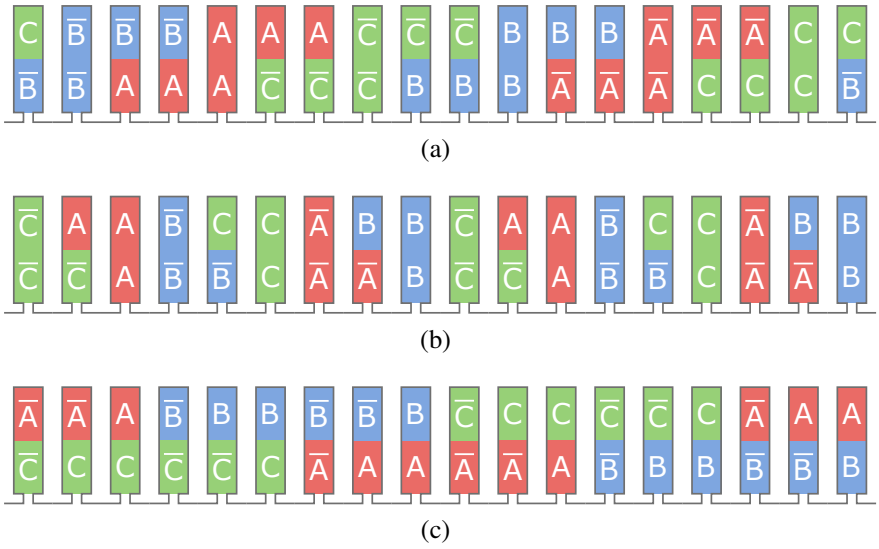

Figure 2.4 In-slot diagrams of 18-slot, three-phase symmetric winding configurations. In (a) a 2-pole ISW configuration ($q = 3$), (b) a 4-pole FSW configuration ($q = 1.5$), (c) a 8-pole FSCW configuration ($q = 0.75$).

2.2.2 Winding design decision variables

The in-slot distribution of the winding conductors described by (2.1) would be the most general set of decision variables if the number of rows corresponded to Z parallel paths. In this case, depending on the electrical connection between those paths and the power supply system, there can be up to Z distinct current-paths flowing in the winding conductors. Therefore, a vector comprising $Z^2 + Z$ decision variables (Z^2 for all coil-sides number of

conductors plus the definition of Z current sources) allows for a universal winding design optimization methodology to be built on. From there on, design requirements could be attained by a suitable set of objective functions and constraints. However, developing an optimizer capable to handle the vast search space created by such optimization problem is still not practical, due to convergence issues owing to the large share of unfeasible solutions, as well as the complete electromagnetic analysis required to determine the current values in each parallel path.

In order to overcome the convergence and electromagnetic analysis issues, a compromise between generalization and available computational resources should be sought. For this reason, only a single current-path per phase is allowed, therefore the resulting decision variables set is defined as the matrix form of (2.1). Another issue regarding convergence consists of the solutions that do not guarantee the same number of going and returning conductors, as one coil is the combination of two coil-sides with opposite polarities and equal number of conductors. To overcome this construction issue, half of the conductors of one phase must be symmetrical to the other half. Notice that for the cases of an odd number of stator slots, a single conductor is left without a symmetrical pair. This intrinsically unconnected conductor is later solved by the proposed end-winding connection strategy.

The resulting winding patterns may lead to coil-pitches of even and odd numbers of slots separately. Figs. 2.5a and 2.5b illustrate the even and odd coil-pitch symmetries, respectively, applied to a 8-slot, three-phase machine. Finally, a last constraint ensures a balanced phase system of the winding, by repeating the same phase pattern throughout the phases, but displaced by one or more phase shifts, thus allowing for the design of asymmetrical winding configurations.

Hence, the decision variable vector for the proposed winding design methodology is given by

$$\mathbf{x} = \begin{bmatrix} \mathbf{t} & \mathbf{s} \end{bmatrix}, \tag{2.2}$$

where

$$\mathbf{t} = \begin{bmatrix} t_1 & t_2 & \cdots & t_{\lceil Z/2 \rceil} \end{bmatrix}, t_i \in \mathbb{Z}, \tag{2.3}$$

is the decision vector containing the number of turns of the coil-sides,

$$\mathbf{s} = \begin{bmatrix} s_1 & s_2 & \cdots & s_{m-1} \end{bmatrix}, s_i \in \mathbb{Z}^+, \tag{2.4}$$

is the decision vector containing the phase shifts of all winding phase subsets, where s_i, $i = 1, ..., m-1$, is the phase shift in slots between the phase i and the first phase.

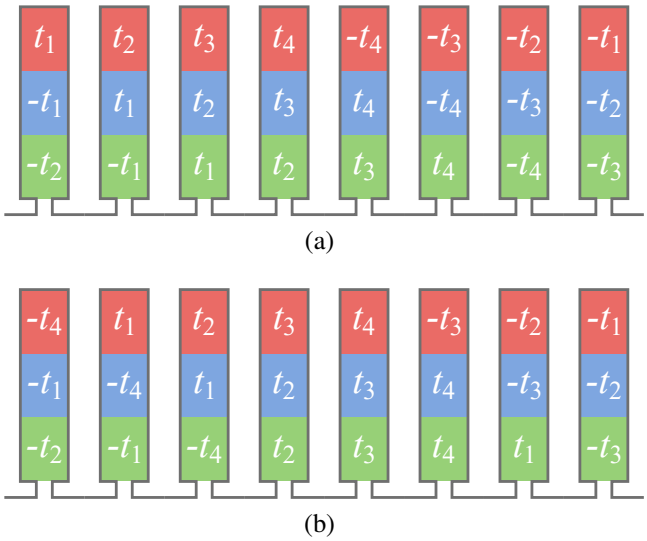

Figure 2.5 Symmetry conditions for winding configurations with coil-pitches with: (a) odd number of slots (1 and 3), and (b) even number of slots (2 and 4).

Given the aforementioned odd and even coil-pitch symmetry constraints, the elements of $\mathbf{N}$ are mapped to $\mathbf{t}$, in such way that the odd coil-pitch symmetry can be indexed by

$$n_{i,j}^{(\text{odd})} = \begin{cases} t_{\text{h}(i,j)} & ,\text{h}(i,j) \leqslant \lceil Z/2 \rceil \\ -t_{[Z-\text{h}(i,j)+1]} & ,\text{h}(i,j) > \lceil Z/2 \rceil \end{cases}, \tag{2.5}$$

and the even coil-pitch symmetry can be indexed by

$$n_{i,j}^{(\text{even})} = \begin{cases} -t_{\lceil Z/2 \rceil} & ,\text{h}(i,j) = 1 \\ t_{[\text{h}(i,j)-1]} & ,1 < \text{h}(i,k) \leqslant \lceil Z/2 \rceil + 1 \\ -t_{[Z-\text{h}(i,j)+1]} & ,\text{h}(i,j) > \lceil Z/2 \rceil + 1 \end{cases}, \tag{2.6}$$

where the phase shift offset is set by

$$\text{h}(i,j) = \text{mod}\,(j-1+s_i, Z)+1. \tag{2.7}$$

2.2.3 End-winding connection strategy

The resulting in-slot winding model described by $\mathbf{N}$ defines the coil-side structure for the active MMF. The complete winding model requires the concretization of a end-winding that connects these coil-sides together. The proposed strategy is an iterative method that searches and connects the maximum number of conductors of one coil-side to the nearest possible with opposite polarity, thus defining a coil.

The proposed end-winding connection mechanism, which is fully described in Algorithm 1, can be summarized in three steps:

1. the first coil-side selected has the smallest number of conductors (line 6);
2. the second coil-side selected has opposite polarity, equal or larger number of conductors, with respect to the first coil-side, and its position leads to minimal coil-pitch, calculated by the pitch function (line 7);
3. if the second coil-side was found (line 8) a coil is consolidated comprising the first and the second coil-sides and its information is removed from the in-slot model (line 16).

The process is repeated until there is no possible coil-sides to be arranged (line 5). At the process completion, if any coil-side remains unconsolidated it is removed from the **N** matrix (line 21). Then, **N** corresponds to a feasible winding design in terms of manufacturing. Moreover, it is possible the resulting winding configuration to have simultaneously odd and even coil-pitches, particularly in the case of odd number of slots.

The end-winding and the coils information is stored in matrices. The slot positions of the coil-sides are saved in the $\mathbf{W}^{\text{iwrd}}$ and $\mathbf{W}^{\text{owrd}}$ matrices with respect to their polarities (lines 9-13); the coils number of turns are saved in the $\mathbf{W}^{\text{turn}}$ matrix (line 14); and the coils coil-pitches are saved in the $\mathbf{W}^{\text{pitch}}$ matrix (line 15).

2.2.4 Airgap magnetomotive force function

In this chapter, the following considerations are assumed for the quick analysis of the airgap MMF:

- the magnetic nonlinearity of the ferromagnetic core is neglected;
- the winding electric current system is balanced;
- the fringing flux, due to the slot openings is neglected;
- the rotor geometry is neglected, only the MMF produced by the stator winding is analyzed;

Therefore, given the consolidated winding model, the MMF as a function of time and angular position can be obtained by

$$\mathrm{M}(\theta,t) = \mathrm{Re}\left\{ \frac{1}{2\pi} \sum_{k=1}^{\infty} V_k e^{j\left[k\theta+\frac{\pi}{2}\right]} \right\}, \tag{2.8}$$

Algorithm 1 end-winding connection strategy.

Inputs: $\mathbf{N}$, Z, and m
Outputs: $\mathbf{N}$, $\mathbf{W}^{\text{iwrd}}$, $\mathbf{W}^{\text{owrd}}$, $\mathbf{W}^{\text{turn}}$, and $\mathbf{W}^{\text{pitch}}$
$\mathbf{N}^{\text{eff}} \leftarrow \mathbf{N}$ and $c \leftarrow 0$
for $i \leftarrow 1$ to m **do**
    while $\mathbf{N}^{\text{eff}}$ has more than one null element in the row i **do**
        $k_1 \leftarrow j : \min_j \left\{ |n_{i,j}^{\text{eff}}| \right\}, n_{i,j}^{\text{eff}} \neq 0$
        $k_2 \leftarrow j : \min_j \{\text{pitch}(j,k_1)\}, n_{i,j}^{\text{eff}} \cdot n_{i,k_1}^{\text{eff}} < 0$
        if k_2 exists **then**
            if $n_{i,k_1}^{\text{eff}} > 0$ **then**
                $w_{i,c}^{\text{iwrd}} \leftarrow k_1$; $w_{i,c}^{\text{owrd}} \leftarrow k_2$
            else
                $w_{i,c}^{\text{iwrd}} \leftarrow k_2$; $w_{i,c}^{\text{owrd}} \leftarrow k_1$
            end if
            $w_{i,c}^{\text{turn}} \leftarrow |n_{k_1,k_2}^{\text{eff}}|$
            $w_{i,c}^{\text{pitch}} \leftarrow \text{pitch}(k_1,k_2)$
            $n_{i,k_1}^{\text{eff}} \leftarrow 0$; $n_{i,k_2}^{\text{eff}} \leftarrow n_{i,k_1}^{\text{eff}} + n_{i,k_2}^{\text{eff}}$
            $c \leftarrow c+1$
        end if
    end while
end for
$\mathbf{N} \leftarrow \mathbf{N} - \mathbf{N}^{\text{eff}}$

where

$$V_k = \frac{I_0 D_k}{k} \sum_{j=1}^{Z} \left[\sum_{i=1}^{m} n_{i,j} \cdot \sin(\omega_0 t - \varphi_i) \right] e^{-jk\theta_j}, \tag{2.9}$$

I_0 is the magnetizing current, assuming a balanced system of currents,

$$D_k = \frac{2}{k\beta} \sin\left(\frac{k\beta}{2}\right) \tag{2.10}$$

is the damping factor due to the slot angular opening (β) [29], ω_0 is the fundamental angular frequency of the current system, $\varphi_i = s_i \cdot p\,(\pi/Z)$. Moreover, in slotless machines $\beta = 2\pi/Z$.

When the aim is only to compute the airgap MMF spatial harmonic content, the following expression can be used.

$$\mathrm{H}_k = \frac{D_k}{k} (\mathbf{u} \cdot \mathbf{v}), \tag{2.11}$$

where the row vector $\mathbf{u}$ is given by

$$\mathbf{u} = \sin(\varphi_{\lfloor i/Z \rfloor + 1}) e^{-jk\frac{2\pi}{Z}\mathrm{mod}(i,Z)},\ i = \{1, ..., mZ\}, \tag{2.12}$$

and

$$\mathbf{v} = \begin{bmatrix} n_{1,1} & \cdots & n_{1,Z} & \cdots & n_{m,1} & \cdots & n_{m,Z} \end{bmatrix}^{\mathrm{T}}, \tag{2.13}$$

where the superscript T denotes transpose.

2.2.5 Winding phase resistance computation

The winding electric resistance is calculated considering the end-winding circular shape as described in [92] and depicted in Fig. 2.6. Hence, for the resulting winding pattern with a total of N_c coils per phase, the stator winding phase resistance is given by

$$R_{\mathrm{ph,s}} = \frac{2\rho}{S_{\mathrm{wire}}} \sum_{k=1}^{N_\mathrm{c}} \left(l_{\mathrm{s,s}} + l_{\mathrm{ew,k}} \right) w_{1,k}^{\mathrm{turn}}, \tag{2.14}$$

where ρ is the conductor material resistivity, $l_{\mathrm{s,s}}$ is the stator stack length, $l_{\mathrm{ew},k}$ is the end-winding length of the k-coil, S_{wire} is the conduction cross-sectional area given by

$$S_{\mathrm{wire}} = \frac{S_{\mathrm{slot}} k_{\mathrm{sff}}}{\max\limits_{j} \left\{ \sum\limits_{i=1}^{m} \left| n_{i,j} \right| \right\}},\ j = \{1, ..., Z\}, \tag{2.15}$$

where S_{slot} is the slot useful cross section, k_{sff} is the maximum slot-fill factor allowed, and

$$l_{\text{ew},k} = w_{1,k}^{\text{pitch}} \cdot k_{\text{ew}} 2\pi \left(r_{\text{i,s}} + h_{\text{s,s}}/2\right)/Z, \tag{2.16}$$

where k_{ew} is the end-winding circular shape coefficient ($k_{\text{ew}} = \pi/2$), $r_{\text{i,s}}$ is the stator inner radius, and $h_{\text{s,s}}$ is the stator slot height [92].

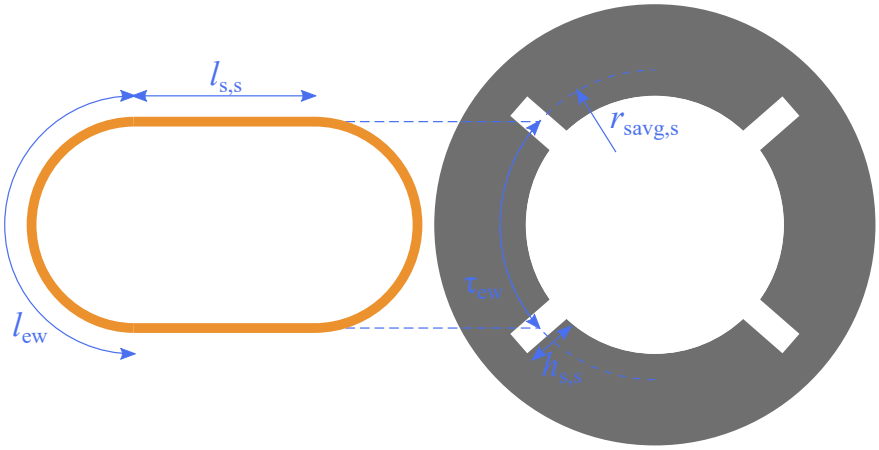

Figure 2.6 Dimensions of a coil with end-winding circular shape.

2.2.6 End-winding leakage inductance computation

The computation of the end-winding leakage inductance is based on the solutions of Neumann's integrals as in [93, 94]. When compared to 3-D FEA computations, this method showed satisfactory accuracy and reduced computational effort. The method here applied is fully described in [93] and it can be applied to any arbitrary 3-D end-coil shape, which has been discretized into a finite number of linear segments. Therefore, depending on the required accuracy, the number of segments may change.

The 3-D contour of an end-coil is herein approximated by N_{ewseg} linear segments, connected in series, which can be defined by a set of points given by

$$\begin{aligned} P_c^i(x,y,z) &= r_c \cos\left(\theta_c^i\right) \cdot \hat{\text{e}}_x + r_c \sin\left(\theta_c^i\right) \cdot \hat{\text{e}}_y + \\ &+ h_c^{\text{ew}} k_{\text{ewh}} \tanh\left(k_{\text{ews}} \sin\left(i\pi/N_{\text{ewseg}}\right)\right) \cdot \hat{\text{e}}_z \end{aligned}, \tag{2.17}$$

where $c = \{1,2,...,N_{\text{c}}\}$, $i = \{0,1,...,N_{\text{ewseg}}\}$, r_c is the radius of the layer where the c-coil lies, and the k_{ewh} and k_{ews} coefficients are used to adjust the end-coils flattening and length. k_{ewh} controls the end-coils height and k_{ews} controls the end-coils curvature (the higher the

value is the sharper the curvature will be). In addition

$$\theta_c^i = \theta_c^{\text{init}} + i\frac{\theta_c^{\text{end}} - \theta_c^{\text{init}}}{N_{\text{ewseg}}}, \tag{2.18}$$

and

$$h_c^{\text{ew}} = \left| \frac{r_{\text{i,s}} + h_{\text{s,s}}/2}{2} \left(\theta_c^{\text{end}} - \theta_c^{\text{init}} \right) \right|, \tag{2.19}$$

where $|\theta_c^{\text{end}} - \theta_c^{\text{init}}|$ is the c-coil angular span. An example of the 3-D end-coil shape of a 36-slot, 4-pole, three-phase integer-slot winding (ISW), computed by (2.17), is displayed in Fig. 2.7.

A coil-side total inductance ($L_{\text{ew,s}}$) is equal to the summation of its self-inductance and the mutual inductances between it and all other end-coils. Thus, the end-winding total leakage inductance per phase is equal to the summation of all end-coil inductances belonging to a given phase [95]. In this method, the self-inductance is due to the flux linkage inside and outside a coil filament.

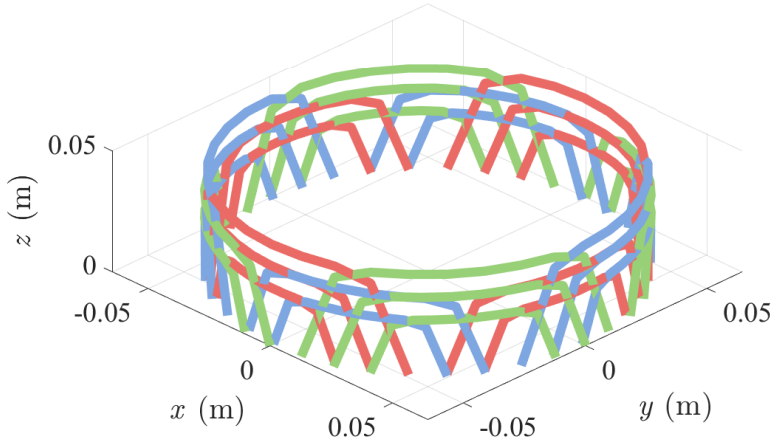

Figure 2.7 End-winding 3-D layout of a 36-slot, 4-pole, three-phase ISW.

2.3 Winding design multiobjective optimization

Ideally, from the manufacturer's and consumer's point of views, the winding must produce minimal losses and promote maximum machine performance for minimal material and manufacturing costs. These objectives are definitely incompatible, owing to either the higher costs of more efficient materials or the complexity of optimal winding configurations that

can negatively affect their production. Concerning the first objective, higher efficiency can be achieved by winding configurations featuring lower MMF harmonic content and reduced winding resistance, as it has been mentioned earlier in this chapter. Since the slot cross-sectional area, the slot-fill factor, and the materials of the conductors are given constants in this methodology, the minimization of the stator resistance is only to be achieved by means of the manipulation of winding configuration. The analysis of manufacturing complexity and costs associated is difficult to ascertain, as varied production processes and technologies dictate the limitations of each manufacturer. However, an increased number of layers generally leads to more complex and expensive manufacturing. For these reasons, an economic analysis of the winding configurations is not performed.

2.3.1 Objective functions

The first objective function is the minimization of the MMF spatial harmonic content, which can be expressed by the total harmonic distortion

$$\mathrm{THD}_{\mathrm{MMF}} = \frac{\sqrt{\sum_{\substack{n=1 \\ n \neq p_{\mathrm{p}}}}^{\infty} |\mathrm{H}_n|^2}}{\left|\mathrm{H}_{[p_{\mathrm{p}}]}\right|}. \tag{2.20}$$

In this equation, the maximization of the MMF fundamental term is already expected, since its absolute value is the denominator function.

The second objective function is the winding electrical resistance calculated by means of (2.14). Bearing in mind the fixed geometry entities for the optimization methodology, namely stack length, slot cross sectional area, and slot-fill factor, the minimization of the winding resistance results in reduced winding weight and conductor material costs.

2.3.2 Constraints

A set of constraints is required to ensure optimization output feasibility regarding the design preferences. Thus, the first constraint limits the level of airgap induction, which is given by

$$B_{\mathrm{ag}}^{\mathrm{l}} \leq \mathrm{B}_{\mathrm{ag}} = \frac{p_{\mathrm{p,eff}} k_{\mathrm{ind}}}{\left|\mathrm{H}_{p_{\mathrm{p,eff}}}\right|} \leq B_{\mathrm{ag}}^{\mathrm{u}}, \tag{2.21}$$

where $B_{\mathrm{ag}}^{\mathrm{l}}$ and $B_{\mathrm{ag}}^{\mathrm{u}}$ are the desired airgap induction lower and upper bounds, respectively, $p_{\mathrm{p,eff}}$ is the winding effective number of pole pairs, which corresponds to the order of the highest non-normalized (i.e. not divided by n) spatial harmonic term in (2.11). The induction

constant k_{ind} is obtained by

$$k_{\text{ind}} = \frac{E_{\text{w}} N_{\text{pp}}}{\pi\sqrt{2} f} \cdot \frac{m}{4 r_{\text{i,s}} l_{\text{s}}}, \tag{2.22}$$

where E_{w} is the winding electromotive force, N_{pp} is the number of winding parallel paths, and f is the voltage frequency.

By allowing the optimizer to control the winding phase shifts, the balance of the whole winding system is no longer granted. Therefore, the balance quality of a winding phase system is herein evaluated by the resulting ellipse for an electric cycle of the direct and quadrature components of the fundamental airgap magnetic flux, produced by a balanced multiphase system of currents. Hence, the winding is balanced for the evaluated winding configuration if such ellipse is a circle. The second constraint discards unbalanced winding designs by evaluating the boolean function, given by

$$Q_{\text{wnd}} = \begin{cases} 1 & , \delta_1 = \delta_2 = \delta_3 \\ 0 & , \text{otherwise} \end{cases}, \tag{2.23}$$

where $\delta_t = \sqrt{{r_{\text{d}}^t}^2 + {r_{\text{q}}^t}^2}$, $t = 1,2,3$, and

$$\begin{bmatrix} r_{\text{d}}^t \\ r_{\text{q}}^t \end{bmatrix} = \begin{bmatrix} \cos(\theta_1) & \cdots & \cos(\theta_m) \\ \sin(\theta_1) & \cdots & \sin(\theta_m) \end{bmatrix} \times \begin{bmatrix} k_{\phi,1} \sin(\alpha_t + \theta_1) \\ \vdots \\ k_{\phi,M} \sin(\alpha_t + \theta_M) \end{bmatrix}, \tag{2.24}$$

where $\theta_p = \mathbf{p}_p \cdot p_{\text{p,eff}} 2\pi/Z,\ p = 1,...,m$, and k_ϕ is the airgap magnetic flux constant, which for this purpose can be assumed neutral. For instance, the angles α_1, α_2, and α_3 can be assessed at 0, 45, and 90 degrees, respectively. Therefore, if Q_{wnd} is 1 the winding system is balanced and MMF function is verified.

2.3.3 A multiobjective Differential Evolution approach

The minimization of the airgap MMF harmonic content and winding resistance are two optimization problem's objectives which are constrained by the airgap magnetic flux density and winding balance characteristic.

A Differential Evolution (DE) [96] based algorithm is used to solve the optimization problem. Other stochastic algorithms, such as multiobjective variations of genetic algorithm and simulated annealing, have been implemented as well, however the DE algorithm showed superior performance.

Due to the problem complexity, the risks of the DE algorithm to stagnate in a suboptimal solution (premature convergence) and to lose population diversity are high. In order to cope with these issues, the auto-enhanced population diversity (AEPD) mechanism [97] is included. The proposed optimizer is fully described in Algorithm 2 and a brief explanation of its main steps is provided as follows.

Algorithm 2 multiobjective Differential Evolution with AEPD algorithm.

Inputs: NP, D, F, CR, $x_{\min}$, and $x_{\max}$
Output: $\mathcal{X}$
/* - - - - - - - - - Algorithm Initialization - - - - - - - - - */
$\mathcal{X} \leftarrow$ random_population(NP)
$\mathcal{U} \leftarrow \emptyset(NP)$
/* - - - - - - - - Population Evolutive Process - - - - - - - - */
while stopping criterion not met **do**
    /* - - - - - - - - - Mutation Process - - - - - - - - - - */
    for $i \leftarrow 1$ up to NP **do**
        Select randomly $r_1 \neq r_2 \neq r_3 \in [1, NP] \setminus i$
        Select randomly $\delta \in [1, D]$
        for $j \leftarrow 1$ up to D **do**
            if $\mathcal{V}_{[0,1]} \leq CR \vee j = \delta$ **then**
                $u_{i,j} \leftarrow x_{r_1,j} + F\left(x_{r_2,j} - x_{r_3,j}\right)$
            else
                $u_{i,j} \leftarrow x_{i,j}$
            end if
            if $u_{i,j} \notin \left[x_{\min,j}, x_{\max,j}\right]$ **then**
                $u_{i,j} = \text{map}(x_{r_1,j}, u_{i,j}, x_{\min,j}, x_{\max,j})$
            end if
        end for
        Evaluate u_i with Algorithm 1
        Evaluate u_i for objective functions and constraints
    end for
    /* - - - - - - - - - - Selection Process - - - - - - - - - */
    $\mathcal{X} \leftarrow \mathcal{X} \cup \mathcal{U}$
    Evaluate the $\mathcal{X}$ individuals feasibility
    $\mathcal{X} \leftarrow$ select$(\mathcal{X}, NP)$
    $\mathcal{X} \leftarrow$ AEPD$(\mathcal{X})$
end while
return $\mathcal{X}$

Initialization

The required algorithm parameters are the number of individuals (NP), the decision variables vector size (D), i.e. the size of vector $\mathbf{x}$, the scaling factor (F), the crossover probability (CR) [96], and the decision variables bounds ($x_{\min}$ and $x_{\max}$). The algorithm starts with a uniformly distributed random initialization of the population $\mathcal{X}$ (line 4). The mutant population is stored in the vector $\mathcal{U}$. Then, the population evolves until a stopping criterion is met.

Mutation

A mutation occurs with probability CR following a uniform random distribution ($\mathcal{V}_{[0,1]}$) or if the j^{th} dimension is forcefully selected (line 13). Otherwise, the i^{th} mutant is equal to the i^{th} individual of the current population (line 16). The mutation operator is the original DE/rand/1/bin [96] (line 14), being the i^{th} mutant equal to the scaled vector difference between three distinct individuals and not equal to the i^{th} individual of the current population. If a mutant individual component falls out of the bounds, the bounce back reinitilization proposed in [96] is employed (line 19), where the map function returns a feasible value for the j^{th} component given the base vector ($x_{r_1,j}$), the violating value ($u_{i,j}$), and the lower ($X_{\min,j}$) and upper ($X_{\max,j}$) bounds.

After mutation, all new individuals' consolidated winding design is obtained with Algorithm 1 (line 22) and the objective functions and constraints are calculated (line 23). Then, both populations are merged (line 26) and their objective function values are recalculated based on their constraint violation severity [98] (line 27).

Selection

The most fitted individuals are selected based on Pareto optimality, by considering their objective values. For this reason, NP individuals are selected from the unified populations using the NSGA-II [48] selection strategy (line 28).

After the selection of the survivors, the AEPD routine based on [97] is executed on the current population to promote diversity (line 29). The result of the optimization is stored in $\mathcal{X}$.

2.4 Case Studies

2.4.1 Experimental evaluation of an optimized winding design

In this case study, the original winding configuration of a 36-slot, 4-pole, three-phase commercial SCIM is optimized using the proposed methodology for odd-pitched winding configurations only. The geometry of the motor is depicted in Fig. 2.8. The reference winding has a symmetric, concentric, single-layer, ISW configuration and it is operated in delta connection mode at 400 V, 50 Hz.

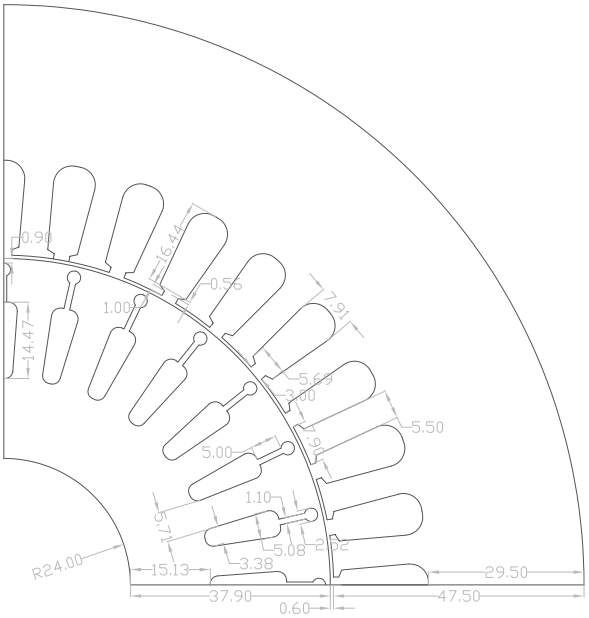

Figure 2.8 Stator and rotor core cross-sectional geometrical dimensions of a 2.7 kW, 4-pole, three-phase SCIM, with a 132S frame and a stack length of 130 mm.

Winding design optimization results

The optimization was performed to minimize both airgap MMF THD and winding resistance, while maintaining the airgap induction of the reference design. The algorithm initialization was the following: (i) the algorithm parameters were $N = 50$, $F = 0.7$, and $C_r = 0.95$; (ii) the general winding structure parameters were $Z = 36$, $p = 4$ and $m = 3$; (iii) the physical constraints parameters were, $B_{\text{ag}}^{\text{l}} = 0.61$, $B_{\text{ag}}^{\text{u}} = 0.62$, $k_{\text{sff}} = 0.43$. The airgap MMF spatial harmonics considered in (2.20) was 102. The maximum number of iterations was 4000, thus evaluating 200 thousand solutions.

The resulting set of nondominated solutions is illustrated in Fig. 2.9. In the selection of the preferred design the following qualities were considered: (i) identical airgap induction; (ii)

simple coil arrangement (low number of layers); (iii) low difference between the maximum and minimum values for the slot-fill factors; (iv) reduced number of coils per phase; and (v) reduced number of different coil-pitches. The reference and optimized winding diagrams are depicted in Fig. 2.10. In Table 2.1 the main characteristics of the reference and optimized winding configurations are provided. The optimized design has practically no fifth and seventh airgap MMF spatial harmonics, while having slightly lower fundamental airgap MMF.

Regarding manufacturing aspects, the reference design has equal slot-fill factor for all stator slots ($k_{\text{sff}} = 0.383$). In the optimized designed the slot-fill factor varies from 0.383, in slots with conductors of one layer with only one phase, and 0.405 in slots with two layers. Moreover, the additional layer in the optimized design requires additional insulation, thus increasing the manufacturing complexity and cost.

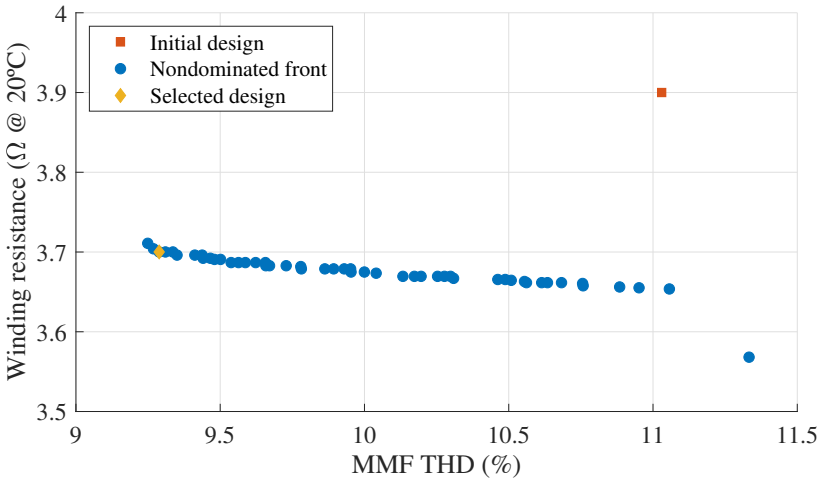

Figure 2.9 Nondominated frontier of the winding optimization.

Table 2.1 Main characteristics of the reference and optimized winding configurations.

Winding	k_{w1}	k_{w5}	k_{w7}	B_{ag} (T)	k_{sff} Min.	k_{sff} Max.
Reference	0.960	0.218	0.177	0.6191	0.383	
Optimized	0.925	0.052	0.014	0.6188	0.383	0.405

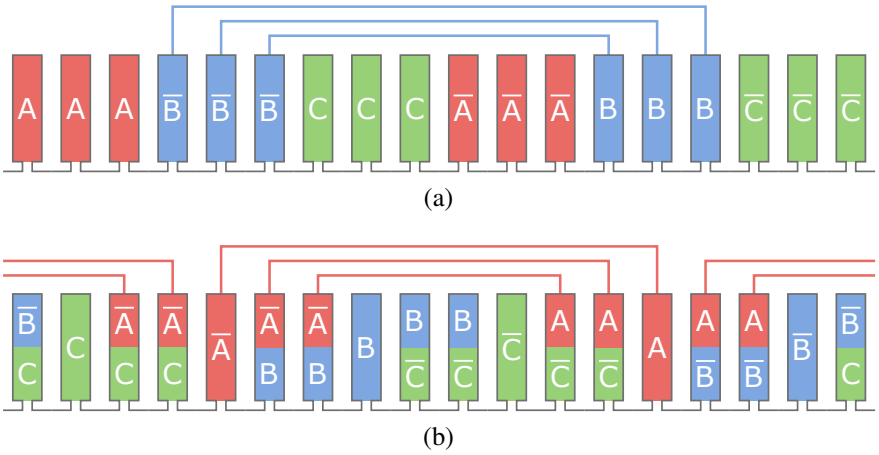

Figure 2.10 Winding configuration diagrams: (a) reference design, 52 turns per coil; (b) optimized design, coils with coil-pitches of 5, 7 and 9 slots and 16, 39 and 52 turns per coil, respectively. The overhang lines represent the end-winding connections, where the pattern is repeated throughout the remaining phases.

Experimental results

The performances of both winding configurations were assessed through experimental tests performed on two identical SCIMs. For coherent results, two motors with near sequential serial numbers were selected, thus ensuring similarity of the built-in materials and manufacturing.

During the rewinding procedure, maximum care was taken to avoid core and coil insulation damaging. Three Pt-100 displaced by 120 mechanical degrees were placed at distinct phases inside the end-windings of both stator windings. One search coil with 10 turns was also added to the stator of each motor for inspection of the magnetic flux. Both windings were assembled with no difficulty, and the assemblage time was similar for the two motors. Furthermore, the optimized design is, in principle, suitable for automated winding assembling machines, since the slot-fill factor was not considerably exceeded (Table 2.1). The measured copper weight of the initial and optimized windings amounts to 4.320 kg and 4.080 kg, respectively (copper reduction of 5.6%).

The same rotor, bearings, end-shields, fan, and fan cover were used in experimental tests, thus ensuring equal conditions for a comparative performance analysis (Fig. 2.11).

Efficiency tests at steady state temperature were performed in both motors for different load ratios, according to the IEC 60034-2-1 standard [99]. The experimental setup used is depicted in Fig. 2.12. The programmable power supply used ensures equal supply voltage with minimal harmonic distortion for both motors. The search coil voltage is monitored by an oscilloscope. The end-winding PT100 resistances are measured with an ohmmeter,

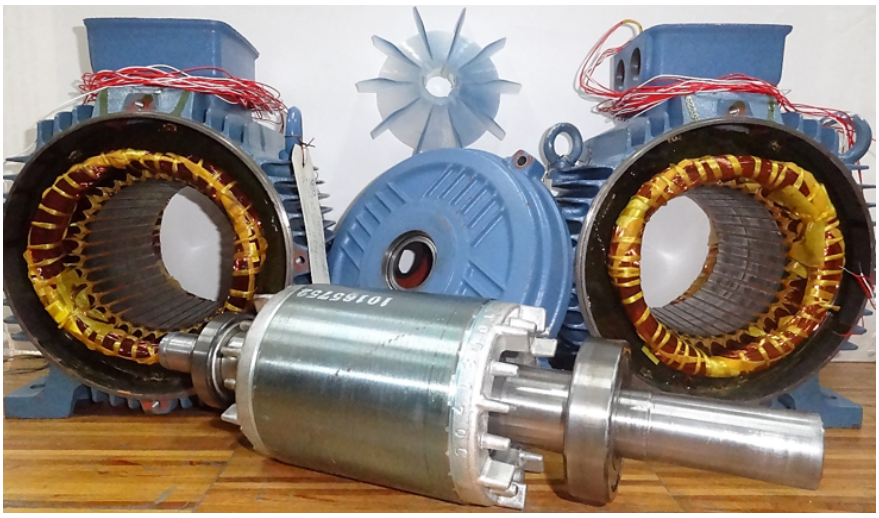

Figure 2.11 Motors used in the experimental tests (on the left the motor with the optimized winding, and, on the right, the motor with the reference winding).

which is used to determine the motor thermal steady-state point (1ºC or less of temperature variation in 30 minutes).

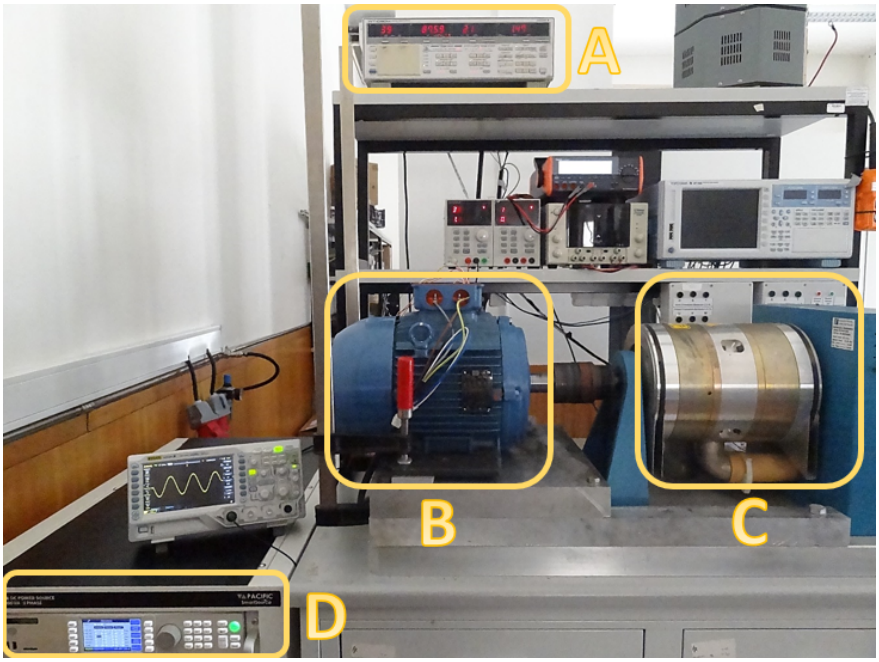

Figure 2.12 Experimental setup: (A) YOKOGAWA WT1030M power analyzer; (B) motor under test; (C) MAGTROL hysteresis dynamometer; (D) PACIFIC POWER 3300AFX programmable power supply.

Two output powers, 2.7 and 4.0 kW, were considered for performance assessments at normal and high-magnetic saturation regimes. A maximum current density of 6 A/mm^2 was

selected to determine the maximum saturation level applied to the motors. In Fig. 2.13 the experimental electric and mechanical quantities obtained for the reference and optimized winding configurations are provided. A significant motor efficiency improvement for the overall operation points was observed in the optimized winding for both nominal powers. The efficiency gains, measured for the 2.7 and 4.0 kW output powers, were 1.94 p.p. and 1.64 p.p., respectively. Regarding the maximum efficiency gain, measured for the 2.7 kW output power, an improvement of 2.66 p.p. at a load ratio of about 0.875 was observed. For the 4.0 kW nominal power, an improvement of 2.06 p.p. at a load ratio of about 0.75 was achieved by the optimized design. Both motors experienced similar induction levels, as it has been verified by the search coils fundamental induced voltages of 6.5 and 6.6 V that were measured at a motor supply voltage of 400 V, and 7.4 and 7.5 V measured at a motor supply voltage of 460 V, for the reference and optimized winding designs, respectively.

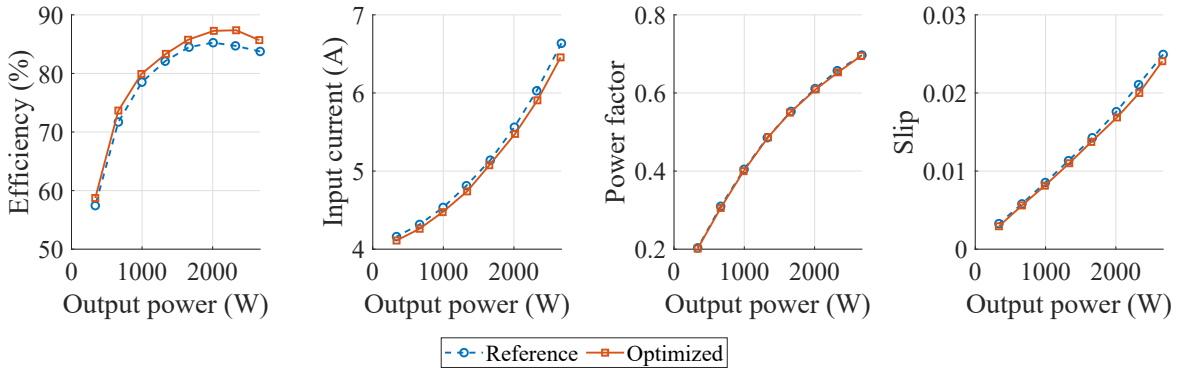

(a)

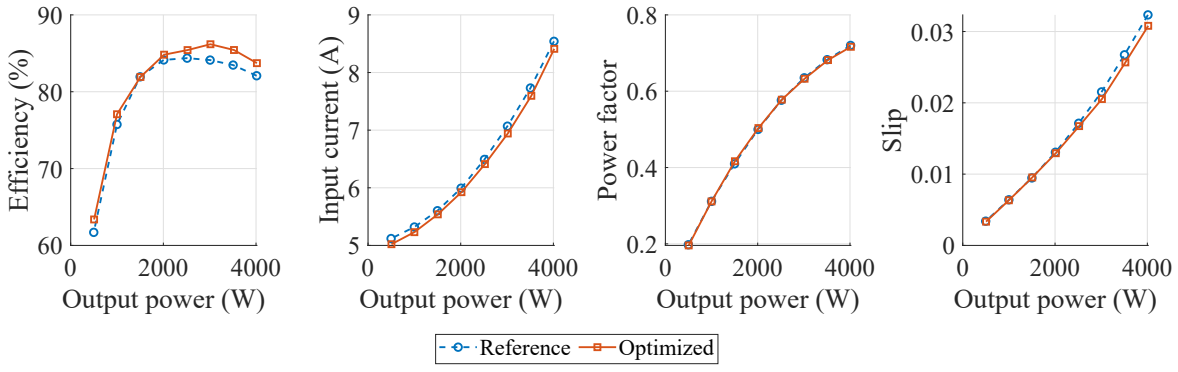

(b)

Figure 2.13 Experimental results of the reference and optimized windings for two different supply voltages: (a) 400 V; (b) 460 V.

A comparative analysis of the motor loss components for the two winding configuration, has been made following the IEC 60034-2-1 standard procedures [99]. In Fig. 2.14 and Table 2.2, the loss components of both designs are provided for a detailed performance comparison.

The stator winding Joule losses ($P_{w,s}$) are the largest loss share at nominal power. A reduction of 9.54% and 11.83% in those losses was observed in the optimized design for the 2.7 and 4.0 kW nominal powers, respectively, mainly due to the smaller line current and also the smaller winding resistance. In addition, the motor with the optimized winding is on average 3.5ºC cooler than the motor with the initial winding (with a standard deviation of 1.0ºC). Regarding the rotor conduction Joule losses ($P_{w,r}$), they are 5.3% and 5.7% smaller in the optimized design for the 2.7 and 4.0 kW nominal powers, respectively. This is mainly due to the smaller slip measured for the optimized design (Fig. 2.13). Therefore, the friction and windage losses (P_{mech}) are slightly higher for the optimized project. Concerning the iron losses (P_{fe}), a reduction of 26.0% and 17.3% has been determined for the optimized design for the 2.7 and 4.0 kW output powers, respectively. This is due to the quality improvement of the airgap MMF, since the two motors share the same parts. In fact, the stator core with the optimized winding experiences a more sinusoidal MMF, mainly due to the great attenuation of the 5^{th} and 7^{th} (Table 2.1) spatial harmonics [79, 29]. A reduction of 48.9% of the stray load losses (P_{sl}) was determined for optimized winding at 2.7 kW output power, although a smaller reduction happened at 4.0 kW output power, in part due to a higher magnetic saturation and the relevance of other loss components, such as the $P_{w,s}$ and P_{fe}. A cancellation of the low order parasitic torques was observed, namely the 5^{th} and 7^{th}, as expected in [77, 29, 100]. The impact of parasitic torques can be observed in the motor line currents (Fig. 2.13): as the slip increases the impact of low-order parasitic torques increases [29], aggravating their total braking torque, which leads to higher current absorption by the reference motor, since both configurations have practically equal power factors (Fig. 2.13).

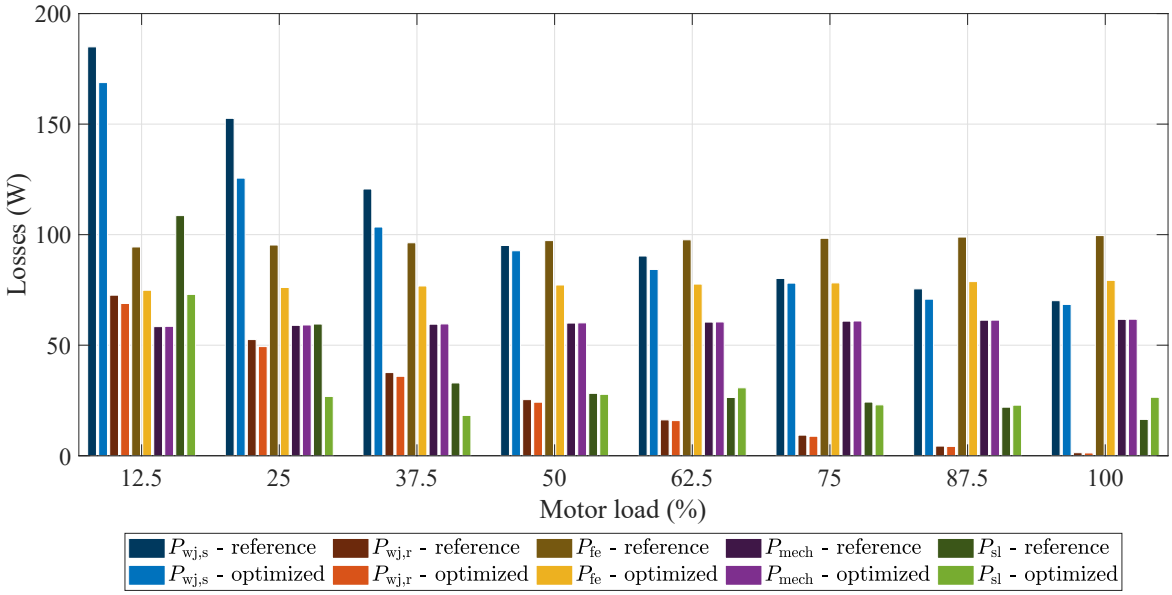

(a)

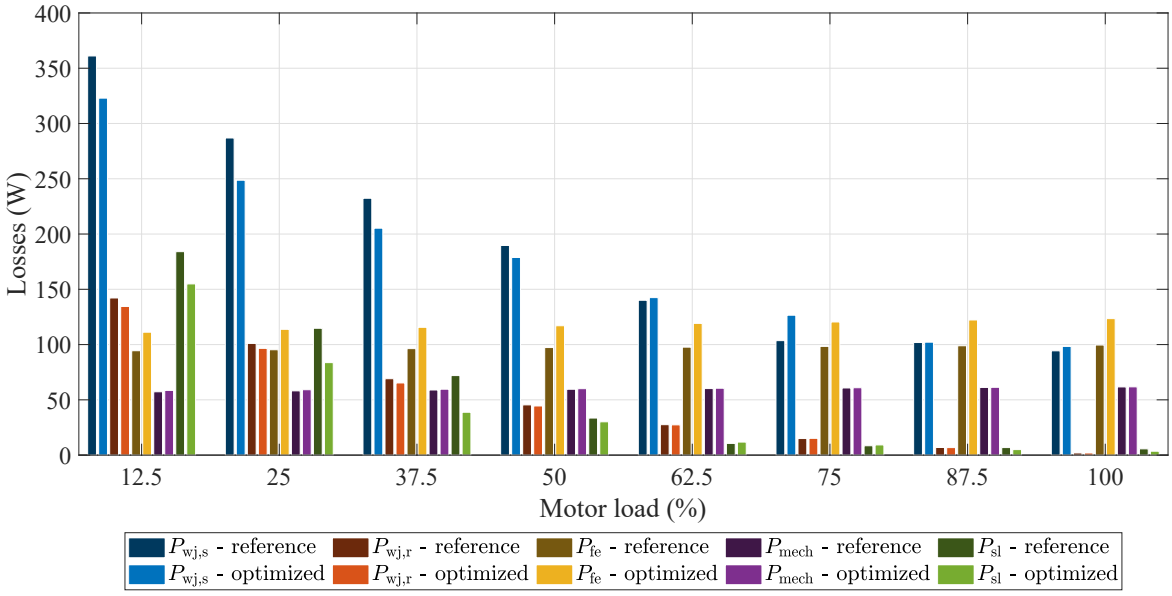

(b)

Figure 2.14 Loss components of the reference and optimized windings: (a) when supplied at 400 V and (b) when supplied at 460 V.

Table 2.2 Motor performance and loss segregation comparative data.

Quantity	Reference	Optimized	Unit	Variation (%)
2.7 kW at 400 V				
Input power	3192	3105	W	−2.80
Shaft power	2673	2661	W	−0.45
Shaft torque	17.452	17.358	N.m	−5.42
Shaft speed	1462.6	1463.9	r.p.m.	+0.09
Slip	2.49	2.4	%	−3.75
Efficiency	83.75	85.69	%	+2.26
P_{mech}	58.4	58.5	W	+0.17
P_{fe}	94.4	74.9	W	−26.03
$P_{\text{wj,s}}$	184.9	168.8	W	−9.54
$P_{\text{wj,r}}$	72.6	68.9	W	−5.37
P_{sl}	108.6	72.9	W	−48.97
Total losses	519	444	W	−16.89
4.0 kW at 460 V				
Input power	4888	4800	W	−1.83
Shaft power	4019	4013	W	−0.15
Shaft torque	26.401	26.398	N.m	−0.01
Shaft speed	1451.5	1453.8	r.p.m.	+0.16
Slip	3.23	3.08	%	−4.87
Efficiency	82.08	83.72	%	+1.95
P_{mech}	57.3	57.5	W	+0.34
P_{fe}	130.4	111.2	W	−17.26
$P_{\text{wj,s}}$	361.1	322.9	W	−11.83
$P_{\text{wj,r}}$	142.2	134.5	W	−5.72
P_{sl}	184.1	154.9	W	−18.85
Total losses	875	781	W	−12.04

2.4.2 Symmetrical and asymmetrical winding optimization

In this case study, the proposed methodology is fully applied to the optimization of two optimized winding configurations: one presented in the previous case study (section 2.4.1) and the other presented in the literature [72]. Hereafter, these windings are referred to as the reference designs. The universal applicability of the proposed methodology is demonstrated by the two distinct winding topologies of the reference designs. The design specifications of the windings are provided in Table 2.3.

Table 2.3 Design specifications of the SCIM and PMSM.

Stator design specifications			
SCIM		**PMSM**	
Slots	36	Slots	18
Outer diameter	220	External diameter	150
Inner diameter	125	Internal diameter	79
Tooth height	18	Tooth height	27.8
Tooth width	55	Tooth width	8.38
Slot opening	3	Slot opening	3
Slot area	110	Slot area	277
Yoke	29.5	Yoke	7.9
Core length	130	Core length	150
Rotor design specifications			
SCIM		**PMSM**	
Poles	4	Poles	8
Bars	28	PM height	4.2
Airgap	0.6	PM width	12
Bar area	69	PM pole arc	90º
Tooth height	22	Airgap	0.5
Shaft diameter	48	Shaft diameter	19.6
Yoke	15.1	Yoke	10

Note: All physical dimensions are in mm.

Winding design optimization results

The decision variable vectors of the SCIM and PMSM reference winding designs are described in Table 2.4. The optimization algorithm parameterization was defined with $NP = 40$, $CR = 0.8$, $F = 0.9$, and 4000 iterations as stopping criterion. For the SCIM constraints, the airgap induction allowed was the interval [0.60, 0.62] T and a slot fill factor of 0.41, whereas

for the PMSM a slot fill factor of 0.5 was set. For optimization results consistency validation purposes, 40 independent optimization runs were performed for both case studies, where each single run was completed on average in 156 and 42 seconds for the SCIM and PMSM cases, respectively. The resulting solutions are displayed in Fig. 2.15. The diagrams of the reference and optimized winding designs of both motors are shown in Fig. 2.16.

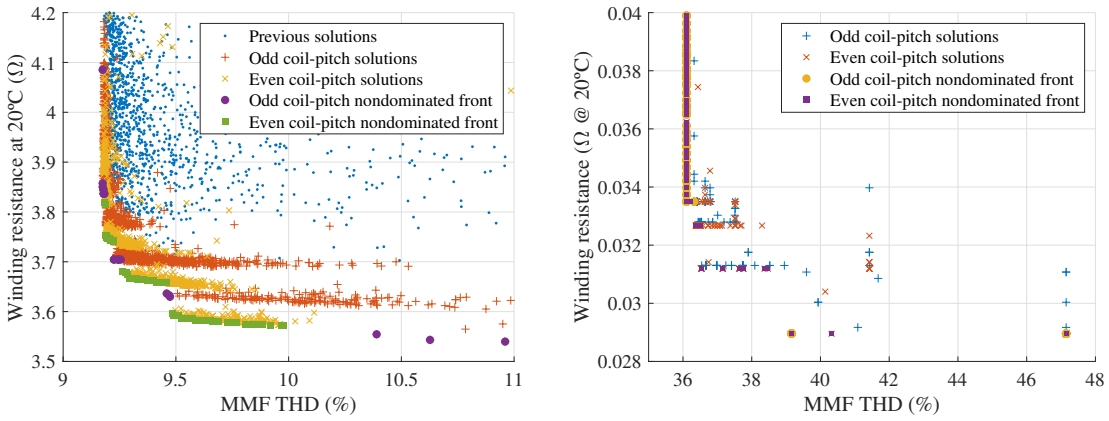

Figure 2.15 Optimization results of the (a) three-phase SCIM and (b) six-phase PMSM.

The optimization results for the SCIM winding configuration are provided in Fig. 2.15a. When compared to the solutions obtained in the case study of section 2.4.1, which are herein referred to as previous solutions, a wider range of Pareto efficient solutions is obtained with the full methodology, especially in the design of winding configurations featuring lower resistance. The improvements are mainly due to the enhanced variety of end-winding connections provided by the coil-sides arrangement algorithm and the even coil-pitch in-slot pattern.

On the other hand, the PMSM optimization results showed fast convergence to the final nondominated front displayed in Fig. 2.15b. This happened most likely due to the scarce number of winding configurations that satisfy the design requirements. In fact, this can be observed in the large discontinuities of the resulting nondominated front.

The optimal designs chosen for each machine were selected considering the compromises between MMF THD and winding resistance, giving more importance to the latter aspect, as the stator Joule losses have the largest impact in the motor total losses. The decision variable vectors of both SCIM and PMSM optimization cases are displayed in Table 2.4 and their characteristics provided in Table 2.5.

In the SCIM optimization case, the optimized design selected has 3% less copper and winding resistance and 2% higher MMF THD. In Fig. 2.17a, the winding factors of the

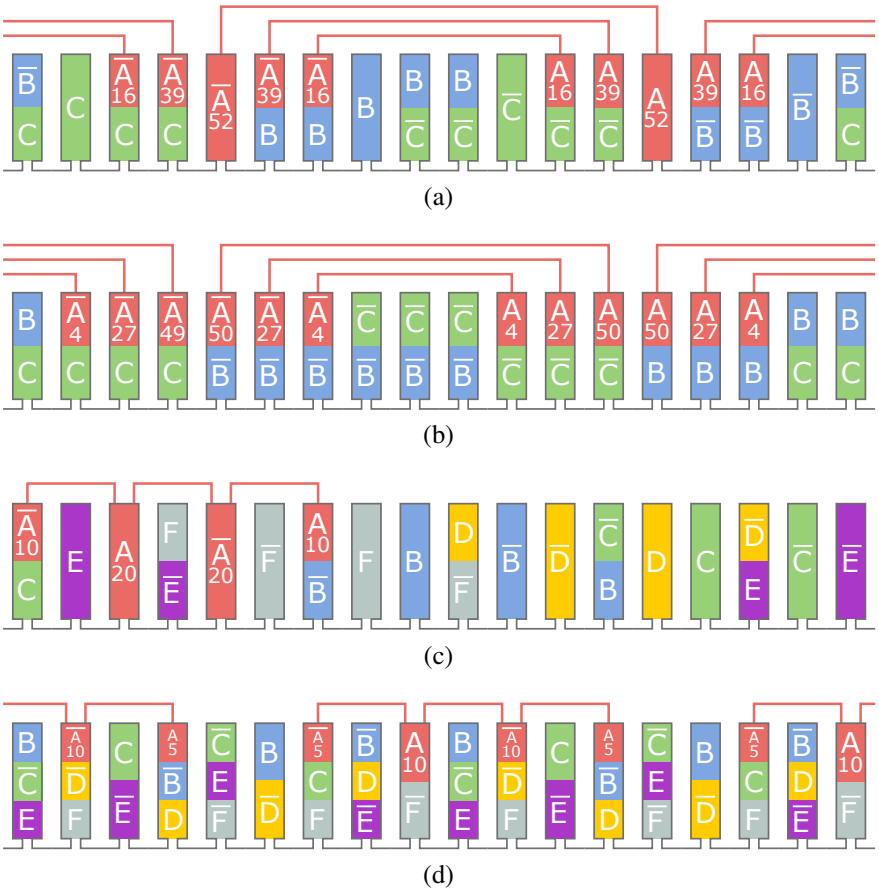

Figure 2.16 Winding configuration diagrams: (a) SCIM reference design, (b) SCIM optimized design, (c) PMSM reference design, (d) PMSM optimized design. The overhang lines represent the end-winding connections and the number of turns is provided, where the pattern is repeated throughout the remaining phases.

SCIM reference and optimized winding configurations are displayed. The degradation of the sinusoidal MMF quality is evident in the optimized design, nevertheless it still features a low MMF THD (Table 2.5). In the PMSM optimization case, the selected solution features equal winding resistance, but 15% lower MMF THD, when compared to the reference design. This MMF THD gain is due to the cancellation of some sub- and inter-harmonics (Fig 2.17b).

Simulation results

Time-step 2-D FEA simulations were performed to obtain the motor efficiency and loss components for different load factors, namely the motor input power (P_{in}), the stator winding Joule losses ($P_{\text{wj,s}}$), the rotor conduction or permanent-magnet Joule losses ($P_{\text{wj,r}}$ and $P_{\text{pm,r}}$, respectively), and the stator and rotor iron losses ($P_{\text{fe,s}}$ and $P_{\text{fe,r}}$, respectively). The stator end-winding leakage inductance ($L_{\text{ew,s}}$) was calculated for all winding designs as explained

Table 2.4 Decision variable vectors of the reference and optimized winding configurations.

Motor	Coil-sides	Phase shift
SCIM Ref.*	(Odd) 0, 0, -16, -39, -52, -39, -16, 0, 0, 0, 0, 16, 39, 52, 39, 16, 0, 0	0, 12, 24
SCIM Opt.*	(Even) 0, -4, -27, -49, -50, -27, -4, 0, 0, 0, 4, 27, 50, 50, 27, 4, 0, 0	0, 21, 6
PMSM Ref.**	(Even) 0, 0, 0, 0, 0, -10, 0, 20, 0	0, 6, 12, 13, 1, 7
PMSM Opt.**	(Even) -10, 0, 5, 0, -5, 0, 10, 0, 0	0, 6, 12, 13, 1, 7

Note: * distributed winding; ** concentrated winding.

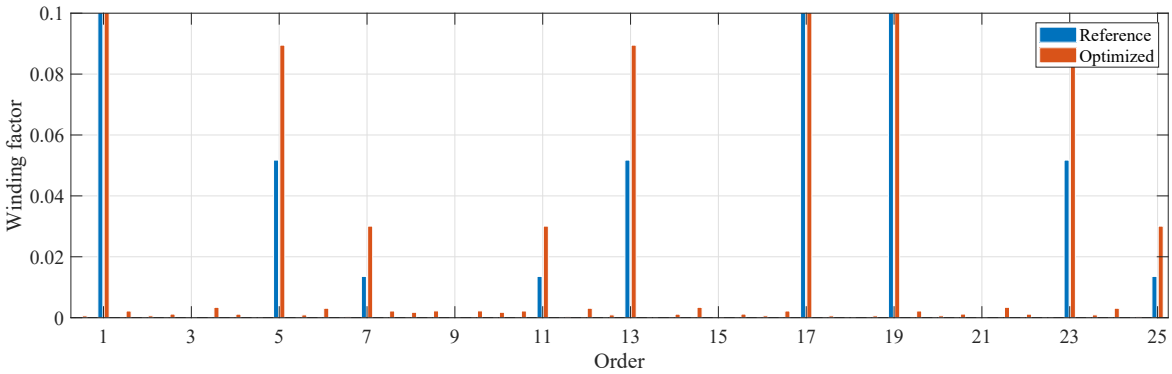

(a)

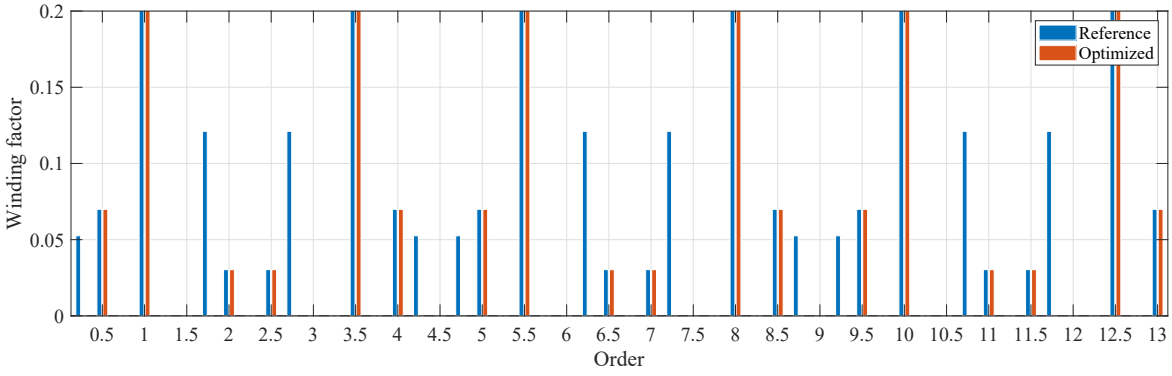

(b)

Figure 2.17 Winding factors of the reference and optimized winding configurations of the (a) SCIM and (b) PMSM. In (a), the fundamental winding factors (order 1) are 0.925 and 0.928 for the reference and optimized windings, respectively. In (b), the fundamental winding factors (order 1) are 0.945 for both winding designs. Winding factors due to the slot and pole combinations have identical values to their fundamentals.

in 2.2.6. The delta-connected SCIMs were supplied by a three-phase sinusoidal voltage

Table 2.5 Winding specifications and rated performance of the evaluated SCIMs and PMSMs.

Motor		SCIM		PMSM	
Specification	Unit	Reference	Optimized	Reference	Optimized
Winding specifications					
MMF THD	%	8.489	8.684	45.973	39.155
k_{w1}		0.925	0.928	0.945	0.945
$R_{ph,s}$	Ω	3.70	3.59	0.02895	0.02895
$L_{ew,s}$	mH	3.54	3.49	1.12E-2	9.36E-3
S_{wire}	mm^2	0.75	0.75	6.73	6.73
Copper weight	kg	3.33	3.23	4.20	4.20
Layers		2	2	2	3
Coils/phase		10	12	3	6
Rated machine performance					
Torque	N.m	16.52	16.52	63.26	63.37
Torque ripple	N.m	2.17	2.48	2.56	3.24
Speed	rpm	1467.7	1467.6	2800	2800
P_{in}	W	2793	2790	19499	19510
$P_{wj,s}$	W	142	138	702	702
$P_{wj,r}$, $P_{pm,r}$	W	44.40	45.30	25.52	23.83
$P_{fe,s}$	W	52.52	52.51	199.44	186.71
$P_{fe,r}$	W	13.16	13.21	25.72	24.19
Efficiency	%	90.96	91.07	95.12	95.24
Voltage	V	400	400	104.03	104.75
Current	V	6.21	6.20	63.64	63.64
THD	%	2.25*	2.52*	20.10**	18.76**

Note: * input current THD; ** input voltage THD.

source, while the star-connected PMSMs were supplied by a six-phase sinusoidal current source. Detailed rated characteristics of the motors are provided in Table 2.5.

In the SCIM simulation scenario, an M800-65A electrical steel is used for both stator and rotor cores, and cage conductors are made of aluminum. In the PMSM simulation scenario, an M270-35A electrical steel is used for the stator and the rotor cores, and permanent magnets have a remanent flux density of 1.1 T, a relative recoil permeability of 1.04, and an electrical resistivity of 1.45 $\mu\Omega$.m. Copper is employed as the conductor's material of the stator windings. The rated performance results of the motors are provided in Table 2.5 and the loss distribution as a function of the output power is displayed in Fig. 2.18a.

In the SCIM optimization case, the reduction of the winding resistance allowed for a residual attenuation of the stator winding Joule losses. However, due to the slight increase of the MMF spatial harmonic components, the motor experienced slightly increased iron losses, in both stator and rotor cores, as well as increased rotor conduction losses. Despite the final balance of all these loss components, there is an efficiency improvement with the optimized winding for all the operating points. Moreover, the lower airgap MMF THD in the reference design positively affects the motor torque production quality, due to the reduced torque ripple, as well as the attenuated stator current THD.

In the PMSM optimization case, the stator winding Joule losses are equal and constant for both winding designs, due to equal winding resistance and supply current. In this case, all residual efficiency improvements achieved are likely to be a result of the cancellation of several MMF spatial harmonic components. As expected, the stator and rotor cores iron losses and the permanent-magnet Joule losses were slightly attenuated with the optimized winding, which is an expected result for windings featuring lower MMF harmonic content as noted in [79]. Moreover, the back-EMF of the PMSM with optimized winding design benefits from lower THD. However, contrarily to the predictions, the torque production quality of the reference design showed advantage over the optimized design, as it generated less torque ripple. A justification may rely on the interaction between the stator MMF and the invariant and almost square function of the rotor MMF, as a more square function of the stator MMF is achieved with the reference design.

Regarding the manufacturing aspects, both optimized winding designs increase the complexity of the winding insertion process. In the SCIM solution, the winding has two additional coils per phase and equal number of layers, while in the PMSM solution it is even more challenging, since it has the double of coils per phase and an additional layer, thus requiring additional insulation. Nevertheless, considering that the reference designs were already notably optimized, positive outcomes were achieved regarding the residual overall efficiency improvement verified in both motors, and the reduced winding weight in the SCIM optimized solution.

2.5 Conclusions

In this chapter, a review of the major contributions in literature was carried out for a comprehensive recognition of modern trends in winding design optimization. The aim of this study was to analyze the main winding configurations proposed and evaluate the possibilities available for further innovation in this field. The production of more sinusoidal MMF waveforms and more compact winding configurations (reduced weight and electrical resistance) are two

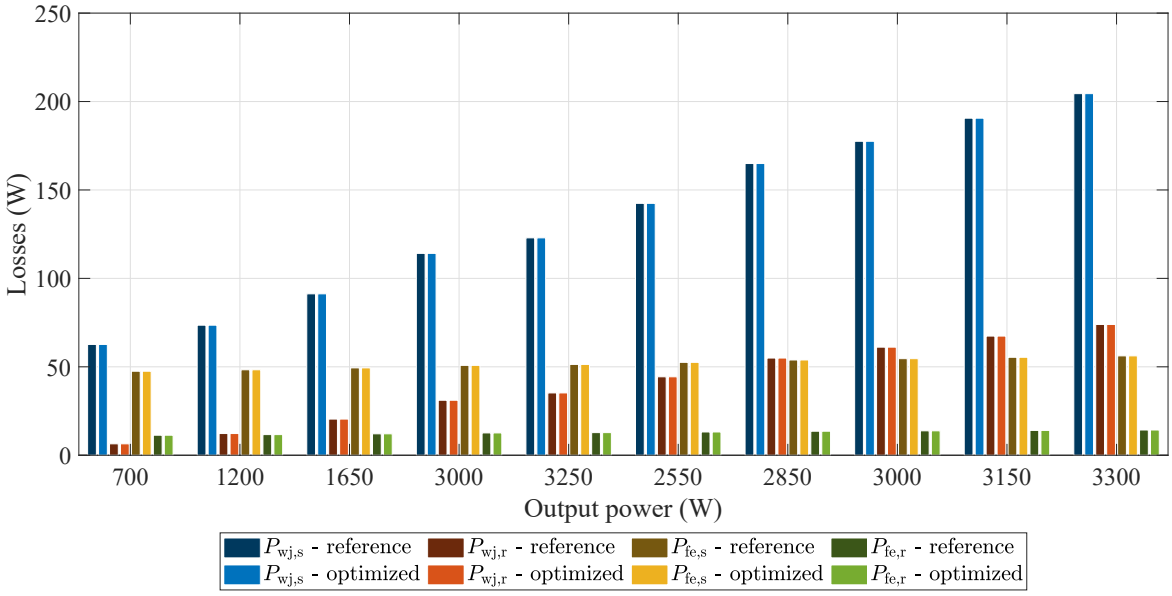

(a)

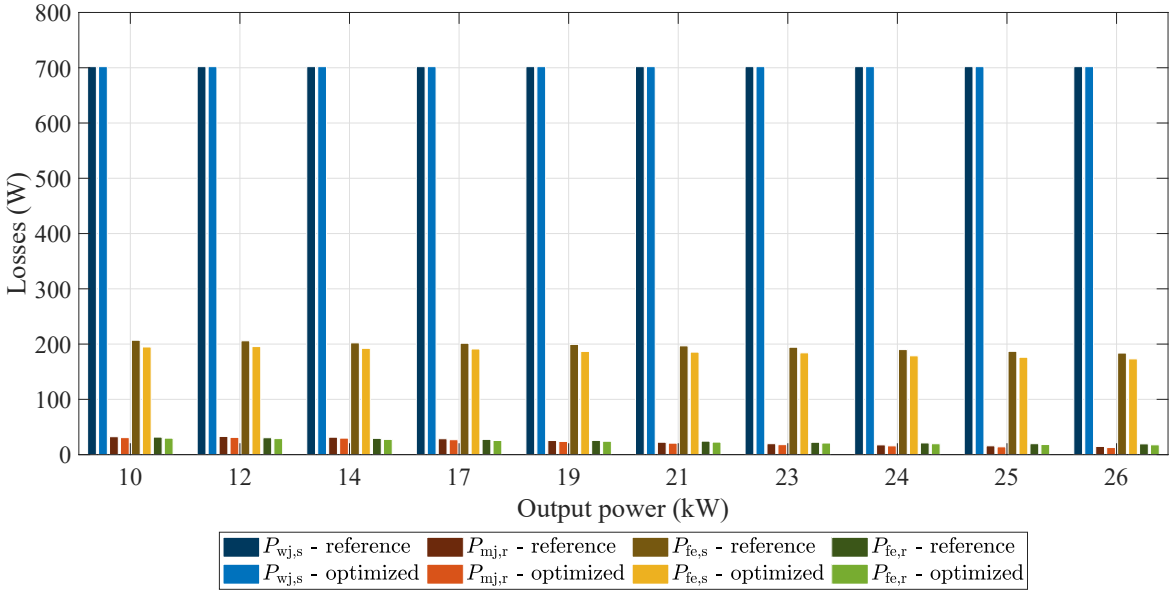

(b)

Figure 2.18 Loss components of the reference and optimized windings of the (a) SCIM (b) PMSM.

consensual objectives aiming at improved machine performance. Generally, methodologies are developed for specific winding types (slot, pole and phase ratios) without ever mentioning eventual improvements that could be achieved by extrapolating their strategies to other types of winding configurations.

From this perspective, the proposed methodology aimed to generalize and unify multifarious winding design optimization approaches into a single framework, thus allowing certain design features that were only applied in specific contexts to be investigated in an universal optimization application, such as, employing tooth-concentrated coils in an integer distributed winding configurations. The case studies provided aim to validate the applicability of the proposed methodology and the following conclusions can be drawn:

- The proposed methodology allows for the design of novel winding configurations envisioned to improve performance and reduce the amount of active conductor materials of the machine.
- The main features contributing to such universal winding design optimization strategy include: (i) the vast decision variables, comprising the global in-slot multilayer and phase-shift concepts for enhanced symmetrical and asymmetrical multiphase winding configurations; (ii) the wider range of coil-pitch combinations; (iii) the novel end-winding connection iterative algorithm in literature that promotes reduced phase resistance and weight.
- It is almost certain that this methodology is the most general developed so far. The basis for the construction of a universal approach has been described in section 2.2.2, yet its implementation is dependent on the development of more efficient optimization algorithms.
- Given the proposed objectives and constraints, few data is required to set up the optimization algorithm, which makes this framework suitable and very relevant for motor repairing/rewinding commercial businesses.
- In general, the Pareto optimal solution set results in winding configurations that are technically more exigent to manufacture, due to additional number of layers and coils.
- A minimal MMF THD is a coherent indicator for enhanced machine performance, yet the interaction of both stator and rotor fluxes must be investigated in more detail for an improved assessment of the machine performance, especially for the torque ripple analysis.
- Bounds for the optimization proposed objectives can be known in advance: by calculating the THD considering only the harmonics due to slot-effect, the MMF THD minimum value that can ideally be achieved is known; and by considering only the total in-slot length of the conductors, the minimal winding electrical resistance that

can ideally be achieved is known. This can be relevant information for the definition of optimization scenario for decision support.

- Finally, the proposed methodology allows for different objective functions and constraints to be considered, thus ensuring both comprehensiveness and flexibility in carrying out multiple studies.

Chapter 3

A Non-parametric Magnetic Equivalent Circuit for the Analysis of Electric Machines

3.1 Introduction

The performance analysis of an electric machine through numerical methods has always been fundamental to obtain a feasible design. Over the past decades, equivalent electric circuits (EEC) featuring lumped parameter models, usually based on empirical equations or on bold physical simplifications, have been used to obtain potential design candidates [31, 101, 102]. Design optimization techniques relying on EEC models feature very fast computational time, allowing for the assessment of thousands of candidates, but at the cost of low accuracy of some critical electromagnetic quantities. Thus, this approach may misguide the optimization convergence and compromise the feasibility of the results obtained [103]. Conversely, finite element analysis (FEA) is the most accurate numerical method available for these purposes, but it requires large computational resources. From this perspective, the low accuracy of EEC models and the massive computational effort required by FEA hardly allow for enhanced design optimization methodologies, in particular, recent non-parametric design optimization methodologies [104, 105], which require exceptional analysis tools featuring a good compromise between accuracy and fast computational response.

The reluctance network (RN) or MEC method is a popular and powerful magnetic field analysis tool that has been applied in design optimization and real-time analysis applications, offering fair accuracy and relatively fast processing time [40, 106–117]. In this method, an electromagnetic device is modeled by means of a circuit of reluctances and MMF sources,

which is solved by the Kirchhoff circuit laws. The method accuracy is dependent on the device geometrical discretization by fundamental reluctance elements. In literature, the rectangular and trapezoidal elementary geometries are commonly applied [40, 41, 109, 107]. However, finer approximations can be obtained with semi-circular [40], sector shaped [41], and even diamond mesh cells [118–120]. Traditionally, a single magnetic flux-path is allowed within an element, resulting in coarser reluctance meshes [103]. Alternatively, additional flux-paths can be added to a reluctance element to promote accuracy and mesh generalization [121, 118–120, 103, 122, 116].

The integration of MEC into CAD and analysis software tools is nowadays available on reputed commercial applications [123–126]. The purpose is to assist the electric machinery pre-design, where parameterized templates are available for swift generation and performance comparison of a set of design options. Nevertheless, these tools have limited geometries available and most of them do not allow for the use of systematic optimization tools. Alternatively, an open-source software framework, as the Magnetic Equivalent Circuit Toolbox [127], enables complex designs to be generated, due to fully customizable configuration of the mesh. In addition, an optimizer can be integrated into such toolbox to enable design strategies. However, owing to the simplicity of this framework and the lack of mesh handling algorithms, its integration into complex design optimization strategies is impracticable.

When dealing with rotating radial-flux machines, the airgap reluctance network plays a crucial role in the MEC overall accuracy. The simplest approaches employ a dense mesh of permeances, connecting both stator and rotor teeth, whose values follow a square or trapezoidal shaped function that depends on the misalignment and overlapping angles of a pair of teeth [40, 128, 129]. In [109, 130], the airgap permeance function takes into account the skewing effect given the overlapping area of a pair of teeth, instead of the angular misalignment. In [40, 131, 113, 132, 133], the magnetic fringing flux is modeled by a smooth sigmoidal function that considers the nearby slot openings. In [134, 135, 114], FEA is employed to determine the airgap permeance function for a specific machine design. Alternatively, in [41, 136, 120, 137, 138], the meshing is built of a single or multiple layers of reluctance elements throughout the airgap region.

Owing to the possibility to concentrate large portions of a device into a single reluctance element, MEC based methods are developed for specific and parameterized designs. Then, to compensate for the consequent accuracy reduction caused by the low mesh density, some refinements are made concerning geometrical parameters, especially in the airgap reluctance network modeling, where dimensions of nearby slot openings and teeth are considered in the airgap permeance functions. Therefore, a more general reluctance network, but still

computationally efficient, needs to be investigated to solve more demanding electric machine design optimization approaches, such as non-parametric methodologies [105].

For these reasons, in this chapter, an improved reluctance network is proposed, combining state-of-the-art contributions into a more general, accurate and fast framework for the analysis of radial-flux machines. In particular, the major proposed contributions concern: (i) a new reluctance element shape and improved airgap permeance function to support non-parametric meshing; (ii) an improved rotor squirrel-cage electric circuit to account for a more accurate modeling of the in bar skin-effect and magnetic shielding effect. Additionally, an extensive electromagnetic analysis of the three main industrial motor technologies (squirrel-cage induction machine, synchronous reluctance machine, and permanent magnet synchronous machine) is provided for a better understanding of the benefits and drawbacks associated with the method for design and real-time simulation applications, when compared to FEA.

3.2 Non-parametric reluctance network

3.2.1 Fundamental reluctance element

The non-parametric representation of radial-flux electric rotating machines can be achieved by the mesh displayed in Fig. 3.1a. A trapezoidal shaped sector element (Fig. 3.1b) is proposed to consider not just the inherent curvatures of an even tangential and radial non-parametric discretization of a radial-flux machine, but also to provide more flexibility when a hybrid mesh is employed. In this case, the proposed element top and bottom arcs naturally adapt the coarser resolution better than a regular rectangular or trapezoidal shape. The fundamental reluctance element is a two flux-path reluctance element, given in a cylindrical coordinate system, as displayed in Fig. 3.1c. Two reluctances define the flux-path along the tangential direction ($R_{\mathrm{m}\theta}$) and another two define the flux-path along the radial direction (R_{mr}). A magnetic scalar potential (V_{m}) is identified at the element central node. When the element is part of a coil-side or a permanent magnet region, then two magnetomotive force (MMF) sources (F_{m}) are included along the tangential or radial directions.

The bidirectional reluctances are calculated as in [40]. Therefore, considering the trapezoidal shaped sector displayed in Fig. 3.1b, its arc length given at a certain radius r, within its top radius (r_{t}) and bottom radius (r_{b}), in meters, is obtained by

$$w(r) = \left[\frac{\alpha_{\mathrm{t}} - \alpha_{\mathrm{b}}}{r_{\mathrm{t}} - r_{\mathrm{b}}}\left(r - r_{\mathrm{b}}\right) + \alpha_{\mathrm{b}}\right] r, \tag{3.1}$$

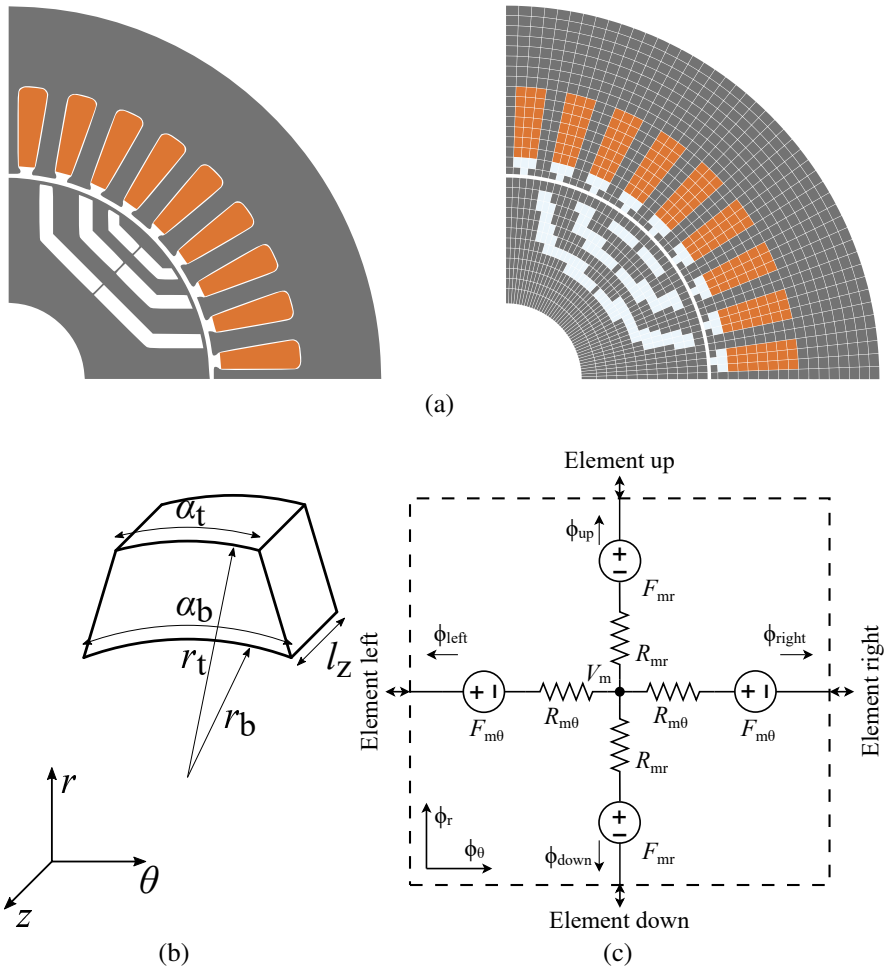

Figure 3.1 Non-parametric reluctance network: (a) mesh example of a synchronous reluctance machine; (b) geometrical characteristics of the mesh fundamental element; and (c) elementary magnetic circuit.

where, α_t and α_b are the top and bottom arcs of the sector in radians. The infinitesimal tangential permeance of the element is obtained by

$$\mathrm{d}g_{m\theta} = \mu \cdot l \frac{\mathrm{d}r}{w(r)} = \frac{\mu \cdot l}{\frac{\alpha_t - \alpha_b}{r_t - r_b} r^2 + \left(\alpha_b - r_b \frac{\alpha_t - \alpha_b}{r_t - r_b}\right) r} \mathrm{d}r, \tag{3.2}$$

where μ is the element magnetic permeability, and l is the element axial length. Similarly, the infinitesimal radial reluctance of the element is given by

$$\mathrm{d}r_{mr} = \frac{1}{\mu l} \frac{1}{w(r)} \mathrm{d}r = \frac{1}{\mu l} \frac{1}{\frac{\alpha_t - \alpha_b}{r_t - r_b} r^2 + \left(\alpha_b - r_b \frac{\alpha_t - \alpha_b}{r_t - r_b}\right) r} \mathrm{d}r. \tag{3.3}$$

Once both infinitesimal reluctance entities are defined, the total tangential and radial reluctance components of the element, as depicted in Fig. 3.1c, can be calculated by integrating the infinitesimal entities along the radial axis. Therefore, the total tangential permeance is given by

$$G_{\mathrm{m}\theta} = \int_{r_\mathrm{b}}^{r_\mathrm{t}} \mathrm{d}g_{\mathrm{m}\theta} = \mu l \frac{1}{\alpha_\mathrm{b} - r_\mathrm{b}\frac{\alpha_\mathrm{t}-\alpha_\mathrm{b}}{r_\mathrm{t}-r_\mathrm{b}}} \ln\left(\frac{r_\mathrm{t}\alpha_\mathrm{b}}{r_\mathrm{b}\alpha_\mathrm{t}}\right), \tag{3.4}$$

hence the tangential reluctance is calculated by

$$R_{\mathrm{m}\theta} = \frac{1}{2G_{\mathrm{m},\theta}} = \frac{1}{2\mu l}\left(\alpha_\mathrm{b} - \frac{\alpha_\mathrm{t}-\alpha_\mathrm{b}}{r_\mathrm{t}-r_\mathrm{b}} r_\mathrm{b}\right) / \ln\left(\frac{r_\mathrm{t}\alpha_\mathrm{b}}{r_\mathrm{b}\alpha_\mathrm{t}}\right). \tag{3.5}$$

Likewise, the radial reluctance is calculated by

$$R_{\mathrm{mr}} = \frac{1}{2}\int_{r_\mathrm{b}}^{r_\mathrm{t}} \mathrm{d}r_{\mathrm{mr}} = \frac{1}{2\mu l} \ln\left(\frac{r_\mathrm{t}\alpha_\mathrm{b}}{r_\mathrm{b}\alpha_\mathrm{t}}\right) / \left(\alpha_\mathrm{b} - \frac{\alpha_\mathrm{t}-\alpha_\mathrm{b}}{r_\mathrm{t}-r_\mathrm{b}} r_\mathrm{b}\right). \tag{3.6}$$

Additionally, the trapezoidal sector area is given by

$$S_\mathrm{m} = \int_{r_\mathrm{b}}^{r_\mathrm{t}} w(r)\mathrm{d}r = \frac{\alpha_\mathrm{t}-\alpha_\mathrm{b}}{r_\mathrm{t}-r_\mathrm{b}}\left(\frac{r_\mathrm{t}^3 - r_\mathrm{b}^3}{3} - r_\mathrm{b}\frac{r_\mathrm{t}^2 - r_\mathrm{b}^2}{2}\right) + \alpha_\mathrm{b}\frac{r_\mathrm{t}^2 - r_\mathrm{b}^2}{2}. \tag{3.7}$$

When compared to simpler regular rectangular and trapezoidal elements [41], the expressions (3.5 - 3.7) are more complex and require additional effort to compute the reluctance geometrical constants of the elements. However, in a complete simulation these constants are only computed once; thus, when considering the total computation time required to simulate a machine, this additional computation effort is negligible.

Hereafter, all electric and magnetic quantities are referred to in the time domain, except when expressed otherwise.

3.2.2 Magnetic flux equations

The fundamental reluctance element tangential and radial magnetic flux components are obtained by

$$\Phi_\theta = \frac{\Phi_{\mathrm{right}} - \Phi_{\mathrm{left}}}{2}, \tag{3.8}$$

and

$$\Phi_\mathrm{r} = \frac{\Phi_{\mathrm{up}} - \Phi_{\mathrm{down}}}{2}, \tag{3.9}$$

respectively. The directional magnetic fluxes are determined by

$$\begin{cases} \Phi_{\text{left}} = \Lambda_{\text{left}} \left[V_{\text{m}} - V_{\text{m,left}} + \left(F_{\text{m}\theta} + F_{\text{m}\theta,\text{left}} \right) \right] \\ \Phi_{\text{right}} = \Lambda_{\text{right}} \left[V_{\text{m}} - V_{\text{m,right}} - \left(F_{\text{m}\theta} + F_{\text{m}\theta,\text{right}} \right) \right] \\ \Phi_{\text{up}} = \Lambda_{\text{up}} \left[V_{\text{m}} - V_{\text{m,up}} + \left(F_{\text{mr}} + F_{\text{mr,up}} \right) \right] \\ \Phi_{\text{down}} = \Lambda_{\text{down}} \left[V_{\text{m}} - V_{\text{m,down}} - \left(F_{\text{mr}} + F_{\text{mr,down}} \right) \right] \end{cases} . \tag{3.10}$$

where the permeances are defined as

$$\begin{cases} \Lambda_{\text{left}} = \left(R_{\text{m}\theta} + R_{\text{m}\theta,\text{left}} \right)^{-1} \\ \Lambda_{\text{right}} = \left(R_{\text{m}\theta} + R_{\text{m}\theta,\text{right}} \right)^{-1} \\ \Lambda_{\text{up}} = \left(R_{\text{mr}} + R_{\text{mr,up}} \right)^{-1} \\ \Lambda_{\text{down}} = \left(R_{\text{mr}} + R_{\text{mr,down}} \right)^{-1} \end{cases} . \tag{3.11}$$

Note that unconnected branches have null values of permeances. The element magnetic flux density is given by

$$B_{\text{m}} = \sqrt{\frac{\Phi_{\text{left}}^2 + \Phi_{\text{right}}^2}{2S_{\text{m}\theta}^2} + \frac{\Phi_{\text{up}}^2 + \Phi_{\text{down}}^2}{2S_{\text{mr}}^2}}, \tag{3.12}$$

where $S_{\text{m}\theta}$ and S_{mr} are the element tangential and radial cross-sectional areas, respectively.

3.2.3 Magnetomotive force equation

In the magnetic domain, a coil-side is defined by the chain of elements that comprises the active conduction elements, which allow electric current to flow along the z-axis, and the coil-side passive or back-iron elements. Accordingly, the MMF function is obtained by the integration of the individual MMFs produced throughout the chain of elements of the coil-side, where only its active conduction elements account for MMF increments. As illustrated in Fig. 3.2, the integration is made from the first active conduction element (Es1) to the last back-iron element (Ey2). Hence, the MMF source value for the coil-side e-element is given by

$$F_{\text{m},e} = \frac{N_{\text{coil}} I_{\text{coil}}}{2S_{\text{coil}}} \left(\frac{\delta_e S_{\text{m},e}}{2} + \sum_{i=1}^{e-1} \delta_i S_{\text{m},i} \right), \tag{3.13}$$

where N_{coil} is the coil-side number of turns, I_{coil} is the coil-side total current, S_{coil} is the total area of the coil-side active conduction region, and

$$\delta_e = \begin{cases} 1 & , e \in \Omega_{\text{cond}} \\ 0 & , \text{otherwise} \end{cases} , \tag{3.14}$$

where Ω_{cond} is set of the coil-side active conduction elements. In case an element comprises MMF sources due to coil-sides, then only one orientation is allowed. Thus, if tangential orientation is assigned then $F_{\text{m}\theta,e} = F_{\text{m},e}$ and $F_{\text{mr},e} = 0$; similarly, if radial orientation is assigned then $F_{\text{mr},e} = F_{\text{m},e}$ and $F_{\text{m}\theta,e} = 0$. An element can accept contributions from varied MMF sources, being a necessary condition for multiple-layer winding configurations and for the proposed squirrel-cage modeling. In case the element belongs to a permanent magnet region, its tangential and radial MMF sources assume the value given by

$$F_{\text{m}\theta,e} = \frac{1}{2} B_{\text{r}} \cdot \cos(\gamma) \cdot S_{\text{m},\theta} \cdot R_{\text{m},\theta} \tag{3.15}$$

and

$$F_{\text{mr},e} = \frac{1}{2} B_{\text{r}} \cdot \sin(\gamma) \cdot S_{\text{m,r}} \cdot R_{\text{m,r}}, \tag{3.16}$$

where B_{r} is the remanent magnetization and γ is the magnet polarization angle referred to the element coordinate system.

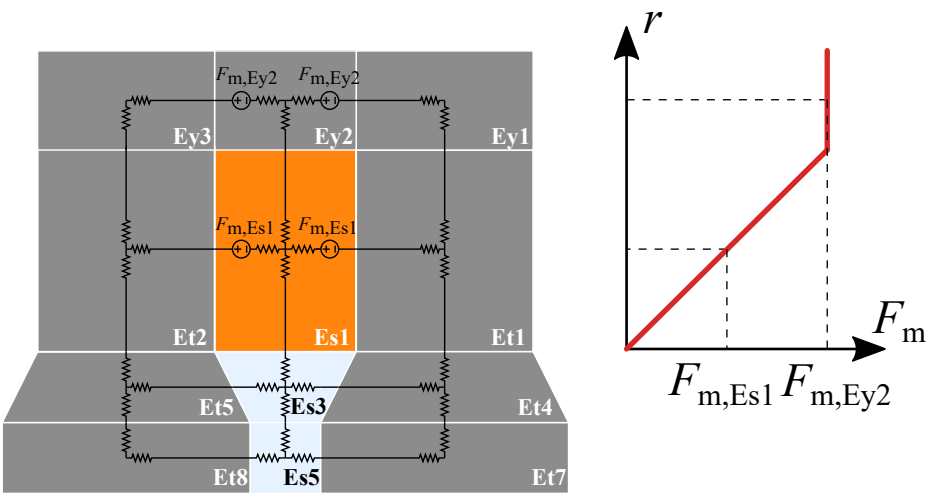

Figure 3.2 MMF produced by a coil-side inside a slot. The element Es1 is the coil-side active conduction element (increases the MMF integration value) and the element Ey2 is the coil-side passive element.

3.2.4 Electromotive force equation

The total electromotive force (EMF) of a coil-side is the summation of all the magnetic fluxes variations with respect to time that are comprised within its total coil-side region. Hence, an

active conduction element EMF is given by

$$E_{\mathrm{m,e}} = -\frac{S_{\mathrm{m,e}}}{S_{\mathrm{coil}}} N_{\mathrm{coil}} \left(\frac{1}{2} \frac{\mathrm{d}\Phi_{\mathrm{m,e}}}{\mathrm{d}t} + \sum_{i=1}^{e-1} \frac{\mathrm{d}\Phi_{\mathrm{m},i}}{\mathrm{d}t} \right), \tag{3.17}$$

where the flux linkage integration is made from the last back-iron element (Ey2) to the conduction active e-element (Es1).

3.2.5 Magnetic torque computation

In the proposed MEC, the torque calculation is done in two manners. In the case of motion, the torque is calculated given the computed machine output power and rotor speed. In the case the rotor is at a standstill position, the Maxwell stress tensor (MST) is here applied for the torque calculation. Hence, considering magnetism only, the torque produced in a cylindrical region is computed by taking into account the tangential forces integrated along an external surrounding surface [38, 139]. In this case, the integration path (Ω_{path}) is an external thin cylindrical layer of reluctance elements surrounding the rotor. Therefore, the instant torque produced by the rotor is obtained by

$$T_{\mathrm{em}} = l r_{\mathrm{path}}^2 \sum_{e \in \Omega_{\mathrm{path}}} \alpha_e \sigma_{\theta,\mathrm{e}}, \tag{3.18}$$

where r_{path} is the average radius of the cylindrical integration path, α_e is the reluctance element average arc, and the MST tangential component is given by

$$\sigma_{\theta,\mathrm{e}} = \frac{B_{\mathrm{r},e} B_{\theta,e}}{\mu_0}. \tag{3.19}$$

In the case of steady state time-harmonic analysis (THA), the MST tangential component is evaluated for a magnetic time cycle, such that

$$\sigma_{\theta,\mathrm{e}} = \frac{1}{T} \int_0^T \frac{B_{\mathrm{r},e} B_{\theta,e}}{\mu_0} dt = \frac{\left| \widehat{B}_{\mathrm{r},e} \widehat{B}_{\theta,e} \right| \cos\left(\varphi_{\mathrm{Br},e} - \varphi_{B\theta,e} \right)}{\mu_0}, \tag{3.20}$$

where T is the magnetic period, $\widehat{B}_{\mathrm{r},e}$ and $\widehat{B}_{\theta,e}$ are the peak radial and tangential magnetic flux density components, respectively, and $\varphi_{\mathrm{Br},e}$ and $\varphi_{B\theta,e}$ are the phases of the radial and tangential magnetic flux density components, respectively.

3.2.6 Iron losses computation

The total iron losses can be separated into the hysteresis, eddy current, and excess loss components [41]. Hence, the total iron losses of a given element can be computed by

$$P_{\mathrm{fe}} = S_{\mathrm{m}} l \left[k_{\mathrm{h}} \widehat{B}_{\mathrm{m}}^{2} f + k_{\mathrm{c}} \left(\frac{\mathrm{d}B_{\mathrm{m}}}{\mathrm{d}t} \right)^{2} + k_{\mathrm{e}} \left(\frac{\mathrm{d}B_{\mathrm{m}}}{\mathrm{d}t} \right)^{1.5} \right], \tag{3.21}$$

where $\widehat{B}_{\mathrm{m}}$ is the element peak magnetic flux density, f is the element magnetic flux density fundamental frequency, and k_{h}, k_{c} and k_{e} are the hysteresis, eddy current and excess Steinmetz iron loss coefficients per unit of volume ($\mathrm{W} \cdot \mathrm{m}^{-3}$).

The discrete hysteresis iron loss component of an element at time step k is calculated as in [41], such that

$$P_{\mathrm{fe,h}}^{(k)} = S_{\mathrm{m}} l \cdot k_{\mathrm{h}} \frac{f}{4} \left(\left| B_{\mathrm{m}}^{(k)} \right| + \left| B_{\mathrm{m}}^{(k-1)} \right| \right) \left| B_{\mathrm{m}}^{(k)} - B_{\mathrm{m}}^{(k-1)} \right|, \tag{3.22}$$

and the discrete eddy current iron loss component of an element at time step k is calculated also as in [41], such that

$$P_{\mathrm{fe,c}}^{(k)} = S_{\mathrm{m}} l \cdot k_{\mathrm{c}} \left(\frac{B_{\mathrm{m}}^{(k)} - B_{\mathrm{m}}^{(k-1)}}{\Delta t} \right)^{2}. \tag{3.23}$$

Similarly, the discrete excess iron loss component of an element at time step k is calculated by

$$P_{\mathrm{fe,e}}^{(k)} = S_{\mathrm{m}} l \cdot k_{\mathrm{e}} \left(\frac{B_{\mathrm{m}}^{(k)} - B_{\mathrm{m}}^{(k-1)}}{\Delta t} \right)^{1.5}. \tag{3.24}$$

In case of steady-state time THA, the total iron losses of an element are computed by

$$P_{\mathrm{fe}} = S_{\mathrm{m}} l \left[k_{\mathrm{h}} \widehat{B}_{\mathrm{m}}^{2} f + k_{\mathrm{c}} \left(\widehat{B}_{\mathrm{m}} f \right)^{2} + k_{\mathrm{e}} \left(\widehat{B}_{\mathrm{m}} f \right)^{1.5} \right]. \tag{3.25}$$

3.2.7 Permanent magnet Joule losses computation

The permanent magnet element discrete Joule losses due to eddy currents at time step k is calculated as in [140, 141], such that

$$P_{\mathrm{pm}}^{(k)} = S_{\mathrm{m}} l \frac{\pi^{2} d^{2}}{6 \rho D} \left(\frac{B_{\mathrm{m}}^{(k)} - B_{\mathrm{m}}^{(k-1)}}{\Delta t} \right)^{2}, \tag{3.26}$$

where d is the depth of element seen by the magnetic flux which is crossing it, D is the mass density of permanent magnet material, and ρ is the magnet electrical resistivity.

3.2.8 Airgap permeance function

The definition of the airgap reluctance network is a very challenging problem, as the airgap permeances cannot be accurately modeled uniquely based on a rather limited number of flux tubes. Mainly owing to the magnetic discontinuities caused by sudden changes in permeability (fringing effect). In a non-parametric model, the airgap permeance function must only be a function of a very limited set of geometrical parameters of the machine, due to the generalization required in dedicated optimization strategies [105].

The proposed airgap permeance function resulted from a comparative study of several proposals in the literature. For this assessment, a model was employed to observe the permeance created by two airgap peripheral elements as a function of misalignment. This model consists of an almost infinite permeable unsaturated closed magnetic circuit with two central teeth with 4- and 8-mm width, separated by a 0.5-mm airgap (Fig. 3.3a), where the overlapping ratio of both tooth tips is one and zero for a misalignment smaller than 2 mm (out of 6 mm, i.e., 33%) and greater than 6 mm (out of 6 mm, i.e., 100%), respectively. In Fig. 3.3b, the curves of the total and tooth-tip FEA permeances refer to the tooth flux and airgap flux integration lines, respectively. Analyzing the total and tooth-tip FEA airgap permeances created by this tooth-to-tooth configuration, two characteristics of the airgap permeance variation with misalignment were observed: when complete overlapping exists, the airgap permeance is constant, while in the cases of partial and null overlapping, the permeance reduction follows an exponential curve. In the proposed airgap function, a constant permeance region is defined for the complete overlapping region of two peripheral airgap elements, as proposed in [40], and for partial and null overlapping cases, the airgap function is defined by an exponential function, as proposed in [142]. For the proposed MEC meshing, the parameters controlling the exponential function decay slope consider the normalized misalignment between the two elements considered and the maximum arcs for complete and null overlapping spans, which is a similar measure used in the airgap permeance attenuation region in [40]. Hence, the proposed airgap permeance function of two any airgap peripheral elements is given by

$$\Lambda_{\mathrm{ag},ij} = \begin{cases} \Lambda_{\mathrm{max},ij} & , \sigma_{ij} \leqslant \alpha_{\mathrm{m}} \\ \Lambda_{\mathrm{max},ij} \cdot \exp\left(- \left[\frac{\sigma_{ij} - \alpha_{\mathrm{m}}}{\alpha_{\mathrm{z}} - \alpha_{\mathrm{m}}} \right]^2 \right) & , \sigma_{ij} > \alpha_{\mathrm{m}} \end{cases} , \tag{3.27}$$

where α_{ij} is the misalignment between the i-element at one side of the airgap periphery and the j-element at the opposite side. The maximum overlapping region between two elements is limited by the arc $\alpha_{\mathrm{m}} = \left|\alpha_i - \alpha_j\right|/2$ and the maximum misalignment before null overlapping is given by the arc $\alpha_{\mathrm{z}} = \left|\alpha_i + \alpha_j\right|/2$, where α_i and α_j are the relative top and bottom arcs of the elements. Additionally, $\Lambda_{\mathrm{max},ij}$ is the permeance connecting the top i- and the bottom j-elements at perfect alignment, whose value, for the case of radial machines, is calculated by (3.6). Rotor eccentricity can be considered by making $\Lambda_{\mathrm{max},ij}$ a function of the rotor position and time.

In Fig. 3.4, the proposed complete airgap meshing applied in radial flux machines is depicted. All airgap peripheral elements contribute to flux conduction between stator and rotor regions. Optionally, an additional layer of air elements can be added for torque computation purposes, namely by the Maxwell stress tensor method. However, this additional layer of elements does not contribute for accuracy improvement.

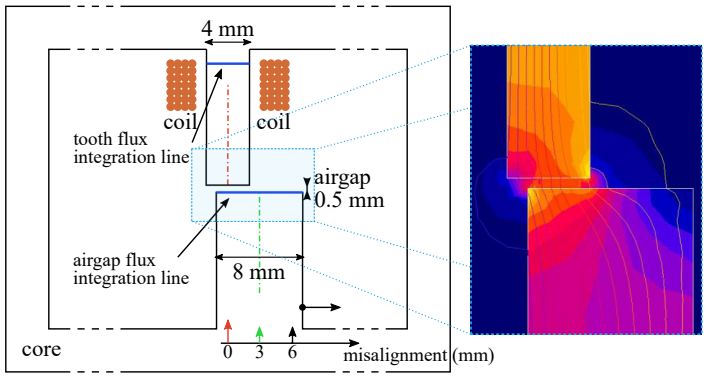

(a)

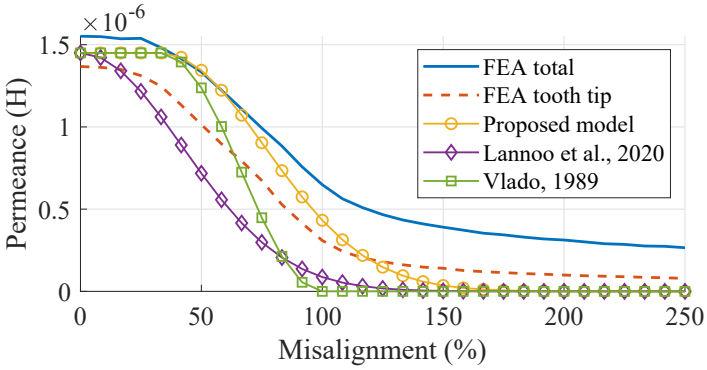

(b)

Figure 3.3 Airgap tooth-to-tooth permeance as a function of tooth misalignment: (a) diagram of the unsaturated closed magnetic circuit considered to assess the permeance variation and the resulting magnetic flux computed by FEA for a tooth misalignment of 3 mm (out of 6 mm, i.e., 50%); (b) airgap permeance curves obtained with FEA and MEC models.

3.3 Solutions of the reluctance network

3.3.1 Magnetic circuit domain system of equations

The system of equations describing the magnetic circuit of a non-parametric reluctance network can be obtained by an equivalent Kirchhoff nodal-voltage or mesh-current circuitry laws. The nodal-voltage or, in this case, the nodal-magnetic-scalar-potential method, is preferable due to implementation simplicity, as each reluctance element accounts for a single equation. Therefore, the flux balance equation is applied according to the Gauss magnetism law, which states that

$$\Phi_{\text{left}} + \Phi_{\text{right}} + \Phi_{\text{up}} + \Phi_{\text{down}} = 0, \tag{3.28}$$

where the resulting unknowns are the magnetic scalar potentials of the reluctance network elements.

When considering airgap periphery elements, the summation of all additional airgap flux-paths connecting the reluctance element is accounted for in (3.28). In this way, the proposed airgap reluctance network does not increase the size of the global system of equations.

3.3.2 Electric circuit domain system of equations

Equations of the electric circuits are obtained by the Kirchhoff mesh-current method, where the unknowns are the currents of the circuit meshes, thus allowing for a simpler formulation of the flux balance equations.

In the case of radial-flux electric rotating machines, the definition of the stator winding electric circuit is straightforward, because the current is uniformly distributed along a coil-side region. Hence, the fundamental circuit of a coil is its equivalent electrical resistance and end-winding leakage inductance connected in series to a voltage source representing its back-EMF. Conversely, the shielding and skin effects in the rotor cage bars, which intensifies with the increase in rotor current frequency (directly dependent on the slip), forces the current to flow in the superior regions of the bars, making the current density distribution nonuniform. Contrarily to most MEC-based models, where the entire bar is modeled by a single current-path (one current unknown per bar), the proposed method accounts for this effect by including multiple current-paths per rotor bar that are connected in parallel, as displayed in Fig. 3.5. Each current-path of the bar model has a EMF source that integrates the magnetic flux of the corresponding element of the bar. For example, considering the bar model with 4 radially stacked elements of Fig. 3.4, the EMF source due to the Es8 element integrates the tangential magnetic fluxes on elements Es8, Es11, Es14, Es17, and Ey8; the EMF source due to the Es11 element integrates the tangential magnetic fluxes on elements

Es11, Es14, Es17, and Ey8; and so on. Therefore, the proposed MEC can model multiple cage rotor configurations.

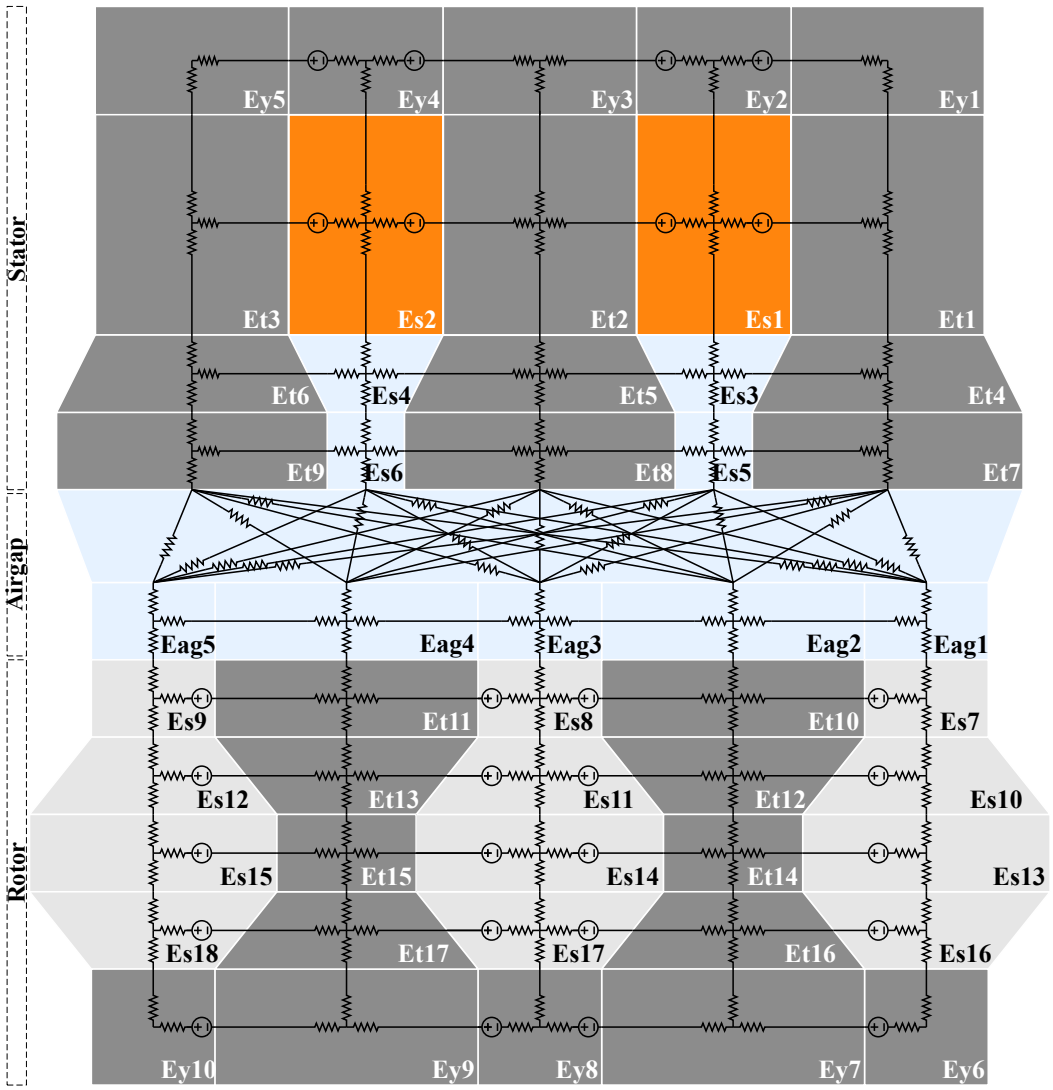

Figure 3.4 SCIM modeling example. Elements enumerated by subscripts *y* denote back-iron regions, *t* tooth regions, *s* slot regions, and *ag* airgap region for the MST integration path (optional). Dark gray elements represent non-conducting magnetic regions, light gray solid-conductor regions, light-blue air regions, and orange stranded-coil regions.

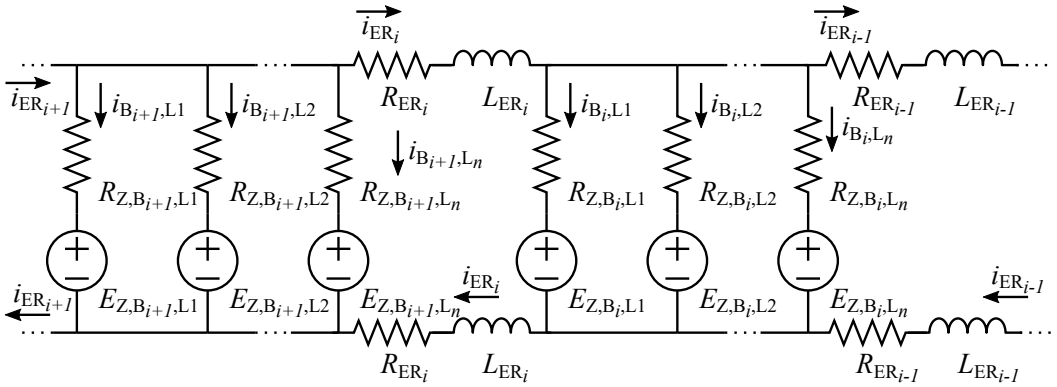

Figure 3.5 Partial electric circuit for the proposed rotor squirrel-cage rotor model, with at least n-radially stacked layers of reluctance elements. The subscript B identifies the bar number, L the layer number, and ER the end-ring number.

3.3.3 Global system of equations

The universal global system of linear equations of a radial-flux device is given by:

$$\begin{bmatrix} \mathbf{A} & \mathbf{F} \\ \mathbf{E} & \mathbf{Z} \end{bmatrix} \begin{bmatrix} v_{\mathrm{m}} \\ i \end{bmatrix} = \begin{bmatrix} k_{\mathrm{pm}} \\ u_{\mathrm{s}} \end{bmatrix}, \tag{3.29}$$

where $\mathbf{A}$ is the matrix comprising the reluctance network permeances, $\mathbf{F}$ is the matrix of the MMF sources, $\mathbf{E}$ is the matrix of the back-EMF sources, and $\mathbf{Z}$ is the matrix of the electric circuits passive components and the current dependent terms of the back-EMF sources equations. The unknowns vector comprises the magnetic scalar potential vector v_{m} and the electric current vector i. The constant terms in (3.29), which result from the permanent magnets remanent magnetizations, are included in the constants vector k_{pm}. The power supply voltage sources are included in the constant vector u_{s}. In the nodal-mesh model proposed, a reference node must be forced in order to avoid matrix singularity, for example by setting the first element scalar potential to zero.

This system of equations is solved for the nodal magnetic scalar potentials of the magnetic circuit domain and the mesh-currents of the electric circuit domain. Moreover, this linear system of equations can be solved efficiently by taking into account its sparsity. Hence, in the proposed framework, the open source general purpose library SuperLU [143, 144] is used to solve (3.29).

In case of THA applications, all time derivative operations are replaced by the complex term $j\omega$, where ω is the domain angular frequency. In time-step applications, (3.29) is modified according to the forward Euler method.

3.3.4 Nonlinear solving

In literature, the B-H nonlinear characteristics of a material are typically handled with the iterative Newton–Raphson method. However, in this case, the bidirectional reluctance element makes impracticable the determination of the Jacobian matrix required by the method, because of the derivative of (3.12) with respect to V_{m}. Instead, the following iterative method is utilized:

1. Initiate all nonlinear element reluctivities (ν) with a saturated reluctivity value (ν_{sat});
2. Solve the system of linear equations and determine the new values of magnetic flux density of all nonlinear elements;
3. Update the nonlinear elements reluctivities with

$$\nu^{(k+1)} = \nu^{(k)} + k_{\mathrm{r}} \left(\nu(B) - \nu^{(k)} \right), \tag{3.30}$$

   where k is the iteration number, k_{r} is a relaxation factor, and an element reluctivity is obtained with the nonlinear material $\nu(B)$ function (e.g. cubic splines);
4. Calculate the elements magnetic flux density variation with

$$\varepsilon = \frac{\left| B^{(k+1)} - B^{(k)} \right|}{B^{(k)}}; \tag{3.31}$$

5. Repeat from step 2 if the maximum magnetic flux density variation of the current iteration is greater than a desired value.

3.3.5 Magnetic periodicity and axial skewing

Magnetic periodicity is herein considered to reduce computational time. Therefore, if magnetic symmetry is verified, the electric machine is reduced to the portion comprising one magnetic pole pair only. The motion of the rotor is solely solved by the airgap permeance function, which refers an element tangential position to a value inside the arc of a pole pair. Thus, there is no need to remesh the stator and rotor regions.

Axial skewing can be regarded as in the FEA method, where slices of the device (axial-wise) are evaluated independently. In this scenario, only the magnetic domain of (3.29) increases in size in the same proportion of the number of slices considered.

3.4 Performance assessment

In this section, the proposed reluctance network is thoroughly compared with the FEA commercial software FLUX by Altair for the three main industrial motoring technologies. Simulations were conducted on a four-core 4.5-GHz computer with 32 GB of RAM.

3.4.1 Case studies

The SCIM, PMSM, and SynRM motor technologies are simulated under motoring and generating operation with FEA and the proposed methodology for a complete computational performance assessment.

In the first case study, the analysis of the 4-pole double-cage SCIM depicted in Fig. 3.6a was carried out using THA. This machine was experimentally tested in [145]. The outer and inner rotor cages present an especially tough analysis challenge, as several complex electromagnetic phenomena take place, thus making this a comprehensive case study. This machine has 36 and 28 stator and rotor slots, respectively, a stack length of 130 mm, it employs a single-layer full-pitched winding of 52 turns per coil, and the core material is a M250-50A grade electrical steel. This core material is used in the following case studies as well. Its iron losses coefficients [41] are $k_{\mathrm{h}} = 74.62$ for the hysteresis losses component, $k_{\mathrm{c}} = 1.046$ for the eddy current losses component, and $k_{\mathrm{e}} = 4.974$ for the excess losses component. The partial reluctance network meshing is displayed in Fig. 3.6b, where 736 reluctance elements were used, resulting in a system of 935 linear equations, against a FEA system of 103295 linear equations. In this case, no periodicity was used. In the simulations, a variable slip ranging from 0.005 to 1 and a 400-V, 50-Hz, three-phase, sinusoidal voltage supply, were considered.

In the second case study, the time-step analysis of the 8-pole PMSM with interior permanent magnets depicted in Fig. 3.7a was conducted. This machine has 48 stator slots, a stack length of 75 mm, a single-layer full-pitched winding of 13 turns per coil and a phase resistance of 88 mΩ. The full reluctance network meshing is displayed in Fig. 3.7b, where 796 reluctance elements were employed in a magnetic pole pair, resulting in a system of 796 linear equations, against a FEA system of 16143 linear equations. In this case, a non-parametric mesh was used in the rotor permanent magnet region. The machine power supply is a three-phase sinusoidal current supply of 200 A (peak). In the simulations, a variable load angle of the current sources was considered, ranging from 0 to 360 degrees, at a constant rotor speed of 1200 rpm, thus allowing for a full four-quadrant analysis of the machine. For each operation point, 90 steps (out of 92) of 0.139 ms each were considered,

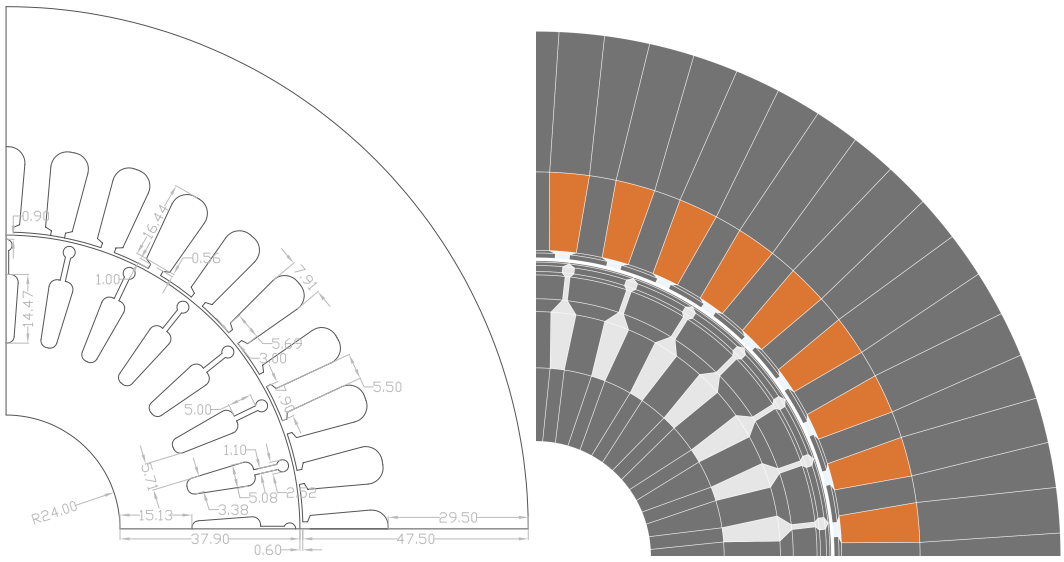

(a) (b)

Figure 3.6 Quarter representation of the double-cage induction machine: (a) geometric dimensions; (b) quarter representation of the parametric mesh employed in the MEC model.

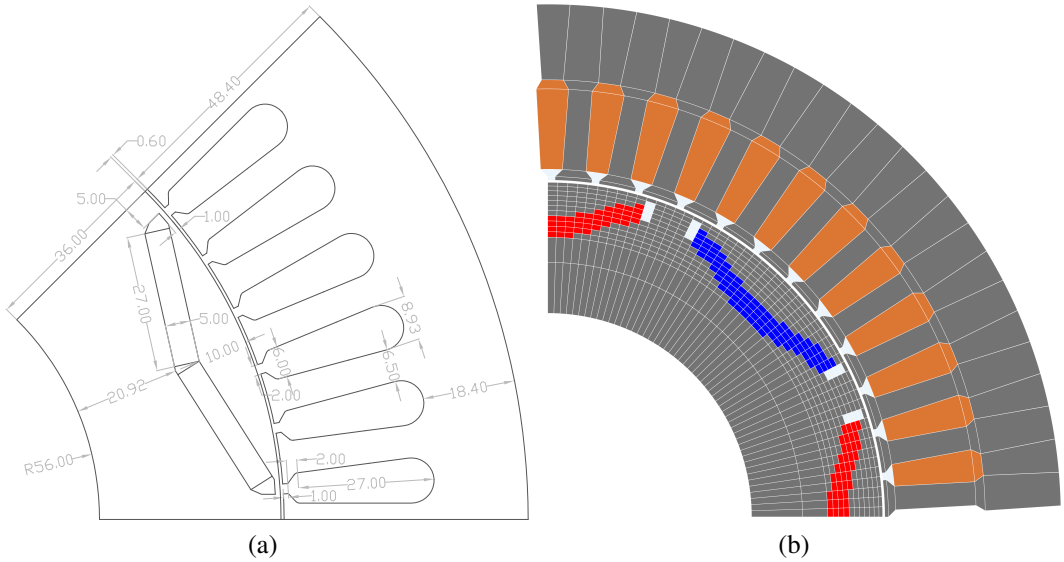

(a) (b)

Figure 3.7 Quarter representation of the synchronous interior permanent magnet machine: (a) geometric dimensions; (b) full representation of the hybrid mesh employed in the MEC model (non-parametric rotor and parametric stator meshes).

where the first two points where discarded for the sake of derivative stability. The permanent magnet resistivity is 1.4E-6 Ω.m.

The last case study was the time-step analysis of the 4-pole synchronous reluctance machine represented in Fig. 3.8a. This machine has 24 stator slots, a stack length of 100 mm,

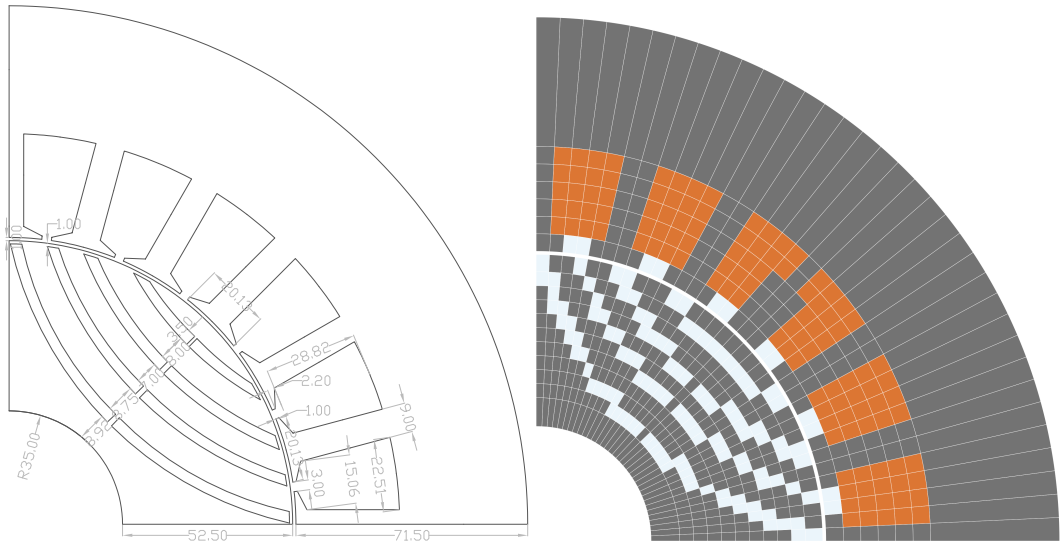

(a) (b)

Figure 3.8 Quarter representation of the synchronous reluctance machine: (a) geometric dimensions; (b) half representation of the full non-parametric mesh employed in the MEC model.

and a single-layer full-pitched winding of 26 turns per coil and a phase resistance of 100 mΩ. In this case, a full non-parametric mesh was selected. The partial reluctance network meshing is displayed in Fig. 3.8b, where 1260 reluctance elements were employed in a magnetic pole pair, resulting in a system of 1260 linear equations, against a FEA system of 21101 linear equations. Similarly to the PMSM, the machine was supplied by a 50-A(peak), 50-Hz, three-phase sinusoidal current supply. In the simulations, a variable load angle of the current sources, ranging from 0 to 180 degrees, at a constant rotor speed of 1500 rpm, was considered, allowing for a full four-quadrant analysis of the machine. Likewise, for each operation point, 90 steps (out of 92) of 0.222 ms each were considered, where the first two points were discarded for the sake of derivative stability.

The main simulation results of the SCIM, PMSM, and SynRM machines are provided in Figs. 3.9, 3.10, and 3.11, respectively.

3.4.2 Results and discussion

When comparing the results of both FEA and the proposed MEC methods, an overall good agreement between the simulated quantities is observed. In the SCIM case studies, additionally to the FEA simulation results, it was possible to compare the MEC method with the experimental tests performed in [145]. In this case, a better approximation was surprisingly achieved by the MEC, possibly bearing to the differences of the real B-H curve

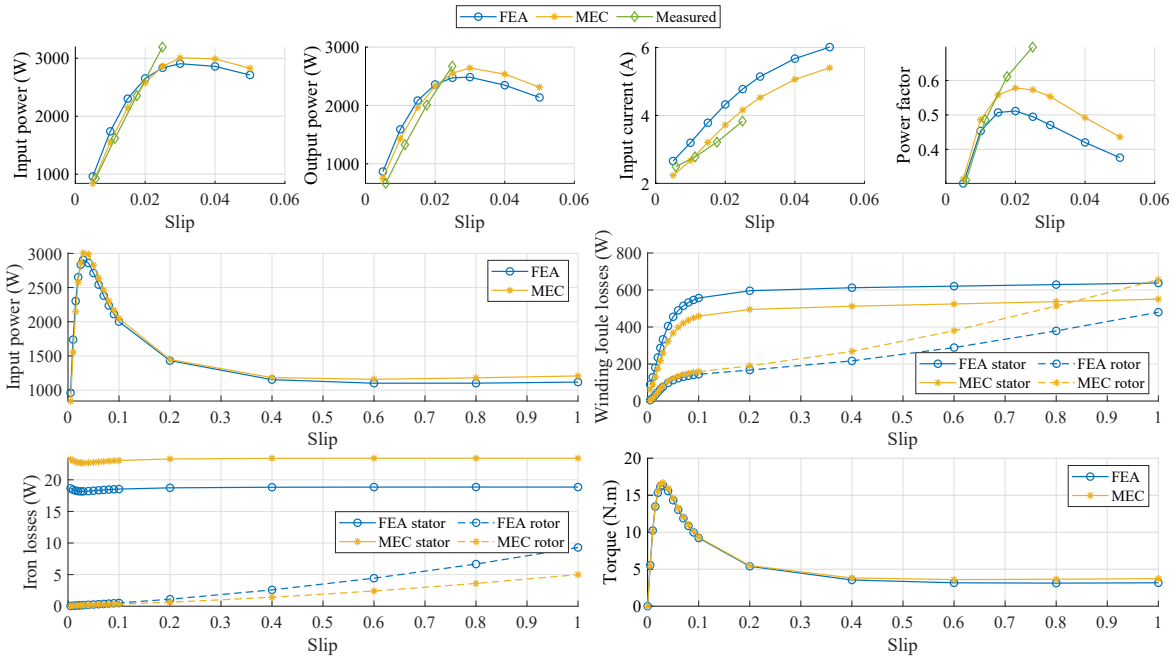

Figure 3.9 Simulation and experimental results of the SCIM case study.

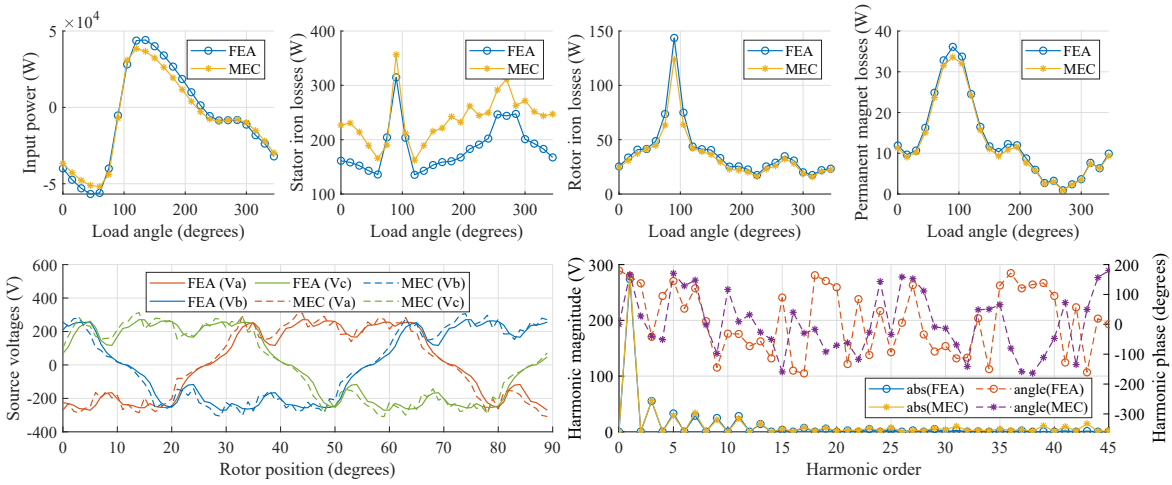

Figure 3.10 Simulation results of the PMSM case study. The stator phase voltage waveforms were sampled at maximum power at motor operation.

of the SCIM. Nevertheless, both FEA and MEC methods showed good agreement with the experimental results obtained.

Regarding the numerical simulations, some results exhibit consistent patterns for the different machines assessed. The most evident one is the stator iron losses, where the MEC method outputs higher values. This relates to the slightly higher magnetic saturation of back-iron regions in the MEC method, caused by the MMF sources in those regions and the coarser

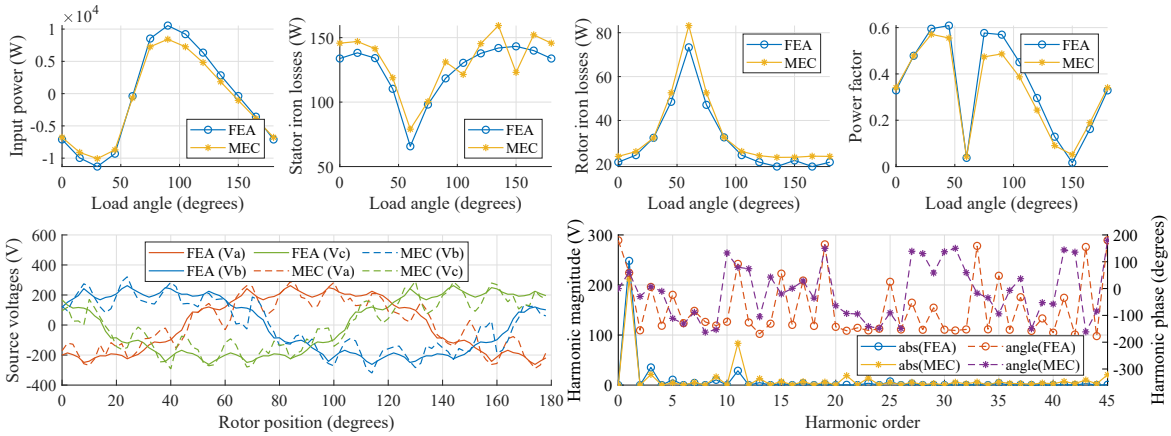

Figure 3.11 Results of the SynRM case study. The stator phase voltage waveforms were sampled at maximum power at motor operation.

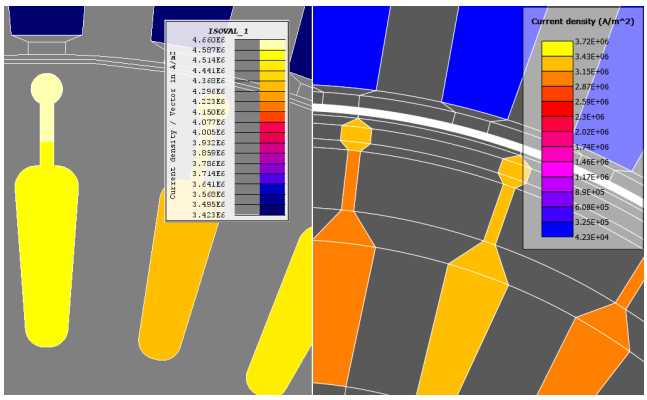

(a)

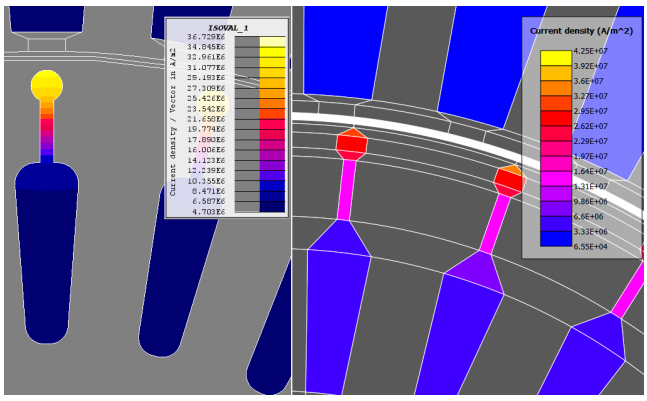

(b)

Figure 3.12 Current density isovalue maps of the SCIM case study: (a, left) slip of 3%, obtained by FEA; (a, right) slip of 3%, obtained by MEC; (b, left) slip of 100%, obtained by FEA; (b, right) slip of 100%, obtained by MEC.

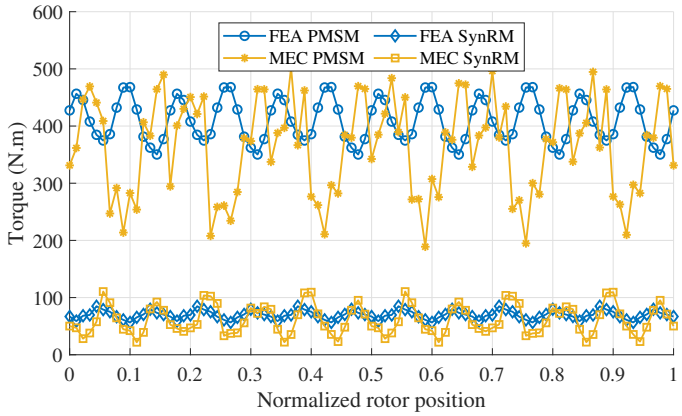

Figure 3.13 Torque curves obtained by FEA and MEC models of the PMSM and SynRM operated at a load angle of 45º and 30º, respectively.

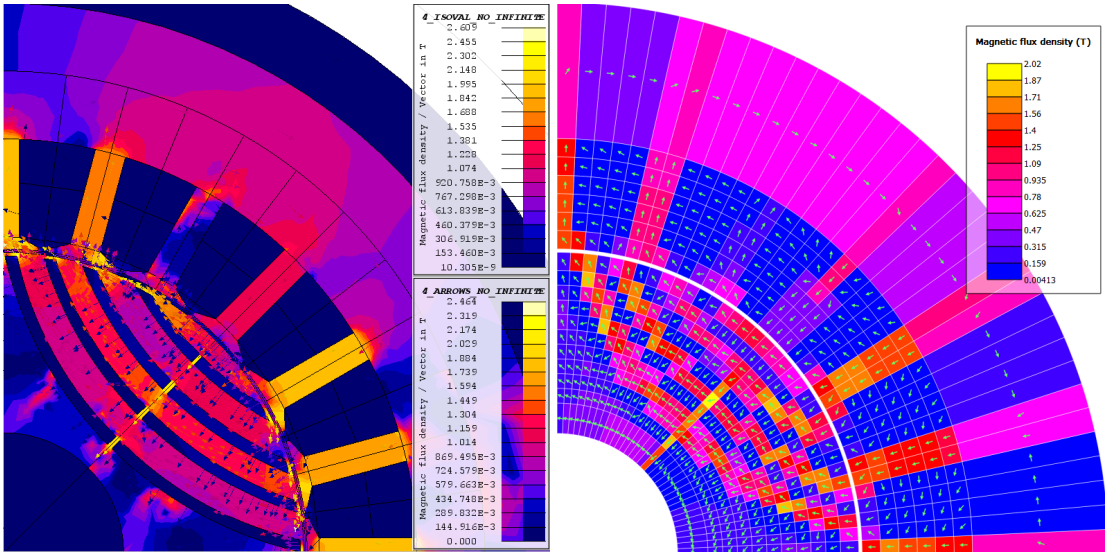

(a) (b)

Figure 3.14 Magnetic flux density isovalue and orientation maps of the SynRM case study (30º load angle and 0º rotor position) obtained by: (a) FEA and (b) MEC.

meshing. This is why the stator iron losses of SynRM case study have better accordance with the FEA results, despite the severe oscillations for load angles greater than 90º, which may be caused by the asymmetric tooth region and the shorter or longer periods that the region gets saturated. Regarding the voltage waveforms measured at the current sources of the PMSM and SynRM case studies, irregular oscillations are observed when compared to the FEA much smoother curves, clearly related to the mesh refinement, especially dense in the airgap region. The squirrel-cage circuit model herein proposed displays satisfactory

performance in the prediction of the current displacement within the rotor bar as shown in Fig. 3.12 for distinct slip values. However, the model accuracy diminishes for increased slip values, as observed in the rotor bar Joule losses and iron losses (Fig. 3.9). This is due to the impossibility of directly embedding the eddy current effect in the global system of equations of the MEC model. Therefore, unless there is a complex circuit model enabling the circulation of eddy currents, an error would always exist in MEC models and it is aggravated for higher frequencies.

By inspecting the torque developed in an electrical cycle by the PMSM and SynRM (Fig. 3.13), it is noticeable the benefits of the SynRM stator teeth finer mesh for the torque ripple analysis, where a better approximation to FEA was achieved when compared to the torque curve accuracy obtained for the PMSM. In fact, when displaying the magnetic flux density isovalue map of the SynRM (Fig. 3.14), it is clear in the FEA the non-uniform distribution of magnetic flux within the stator teeth, especially in the fourth element of the second tooth tip (counterclockwise), whereas in the MEC with a single element per tooth tip, this magnetic flux distribution is not possible.

Further justifications for the FEA and MEC discrepancies are difficult to ascertain, as many physical phenomena are boldly approximated or even neglected due to the coarser meshing and limited physical modeling of MEC (e.g. impossibility of modeling of eddy currents in solid conductors). Nevertheless, it is clear that the higher number of elements employed in the FEA meshing plays a crucial role on the accuracy.

In Table 3.1 the time required by both FEA and MEC methods to solve the machines of the case studies are compared. With the proposed MEC, it was possible to achieve a maximum 50-fold reduction in computational time in the SCIM case study, due to the large difference between the sizes of the MEC and FEA linear system of equations. Moreover, considering that the FEA employs CPU parallel processing, this computational speedup achieved by MEC would have been at least 150 times superior if the same CPU parallel processing were used. When compared to FEA, other MEC models show a shortening of the computational processing time of less than 10 times [107, 119, 137], less than 20 times [110, 113, 120, 121, 133], 55 times [130], and even 1017 times [114]. However, in this latter case, a dedicated FPGA digital circuit was specially tailored to solve the system of linear equations.

Table 3.1 Time required for solving the case studies.

Case study	FEA time (s)	MEC time (s)	Speedup
SCIM	216	4.3	50x
PMSM	7507	641	12x
SynRM	4321	457	9x

3.5 Conclusions

In this chapter, a review of the major contributions presented in literature regarding reluctance network models for electric rotating machines was conducted. This study aimed at investigating state-of-the-art modeling methodologies such that the development and implementation of a dedicated model suiting the high degree of generality required for the goals of this study would have cutting-edge accuracy and computational speed. As it has been concluded from the review, most MEC models were not practical to be implement due to the knowledge of a machine design electromagnetic characteristics required in advance to tune some of their model parameters. Additionally, other models tested were not accurate enough for the degree of generalization required.

The MEC model herein presented resulted from a comprehensive try and error development approach, where different model characteristics of the many literature contributions evaluated were slightly adapted to fulfill the goals for a general MEC model. Therefore, the proposed MEC model was thoroughly validated through an extensive and detailed test-bench, which comprised the analysis of the three main industrial motor technologies. The simulated electromagnetic quantities assessed in this test-bench included the computation of design optimization relevant quantities, such as input power, winding losses, core losses, power factor, permanent magnet Joule losses, torque, and harmonic content, in order to guarantee a trustful goal-oriented validation of the proposed MEC model. From the results obtained, the following main conclusions can be drawn:

- The proposed method proved to be robust and offers a satisfactory compromise between accuracy and computational effort when compared to the FEA method and other MEC models proposed in literature.
- Therefore, the novel non-parametric mesh is suitable for pre-designing and fast analysis of the newest trends in electric machines for industry and electric vehicle [105]. Thus, it is also a good tool to integrate machine design/dimension optimization algorithms, enabling the evaluation of a significantly higher number of dimensional/geometric variations/combinations per unit of time than would be possible with FEA.
- Better accuracy can be achieved by implementing denser meshes or in a more efficient manner by improving the tangential discretization of ferromagnetic regions, thus the elements aspect ratio is lower.
- The method flexibility to interchange between parametric and non-parametric mesh topology enlarges its range of applicability.

- The proposed MEC model could be adapted to a thermal model of lumped parameters for thermal integrity analysis of a machine design. For this purpose, the same mesh adopted in the electromagnetic analysis is sufficiently accurate to model steady-state thermal analysis. In this case, the thermal mathematical problem is a system of linear equations, thus the same circuitry is employed as in the proposed MEC; however, the reluctances are replaced by equivalent resistances with the thermal-conductivity characteristics of the element and the MMF sources are replaced by outward-oriented sources supplying the equivalent losses of the element. In the case of time-step simulations, a capacitance placed at the central node of each element can be included. Each element thermal equivalent capacitance can be calculated given the element's volume, mass, and specific heat. When the element is part of a conductor, the respective losses can be calculated taking into account its current density and resistivity. If the element is part of a ferromagnetic core or a permanent magnet, the iron losses or eddy current losses, respectively, can be easily computed. The unknowns of the global system of linear equations would be the temperature of the central nodes of each element, except those of the shaft and housing border elements, which could have a constant temperature predefined.

- A 3-D MEC model can be expanded from the proposed 2-D MEC. This can be achieved by adding to the z-axis a branch including two additional reluctances and two MMF sources. In this case, at the central node of each 3-D element, six magnetic flux paths have to be considered (additional positive z and negative z directions).

- Accelerated convergence could be achieved by a mesh-based variation to support the Newton-Raphson method for the solution of the nonlinear B-H characteristics of ferromagnetic materials.

- Also, improved computational performance could be achieved by exploiting to the fullest the periodicity of the device, in such way that only one magnetic pole portion is analyzed, as in [42] for a mesh-based MEC.

- Given the critical role that the airgap permeance network plays in the overall accuracy of the method, further research could be undertaken to tackle a more accurate and yet general formulation of the airgap permeance function. Nevertheless, immediate accuracy improvements can be achieved by implementing a finer meshing, especially by increasing the number of tangential elements modeling tooth regions, as it has been observed in the SynRM case study.

Chapter 4

Methodologies for Topological Optimization of Electric Rotating Machines

4.1 Introduction

Quite often, coming up with an initial design for an electric rotating machine requires strenuous efforts. From the vast number of geometrical parameters associated with the machine design for the definition of the stator/rotor circuit and winding configuration, the number of decision variables escalates extremely fast. Previously to the computers advent, engineers relied on empirical formulas, tables, and regular design patterns to achieve a feasible design by adapting a rather limited number of design variables. This suits fine most general motoring applications, where efficiency, power density, and operation cycles are well defined and for those applications where further relevant performance improvements are unlikely. Nowadays, owing to the increasing conscience of climate change and to the necessity to move towards more sustainable societies, the internal combustion engine based drive technologies require an urgent shift to less polluting solutions. For this purpose, electric rotating machines are definitely the best energy conversion solution, due to their unmatched energy efficiency and easy control. For all the applications driven by these obsolete technologies that need to be phased out, there is the need to design suitable electric machines with specific application performance requirements. Therefore, traditional electric machine designs may not fulfill these new specific performance characteristics, thus improved methodologies need to be investigated and implemented to assist the design of such challenging electric machines.

Currently, three main technologies dominate the electric motor-driven applications, namely the SCIM, SynRM, and PMSM. The radial-flux topology is the most commonly employed, where the SCIM is still the dominating motor technology in the industrial sector, particularly in fixed-speed applications. All these machines can be manufactured in many other variations, such as outer rotor [146–149]; axial-flux [150–152]; claw pole [153–156]; single and multiple stator and rotor configurations [157, 158]; and even realized in a *magnetic tunnel* topology, where practically no leakage flux exists and enabling cutting-edge torque density levels [159]. For all these reasons, many topological optimization methodologies have been proposed in literature to either promote general machine performance improvement or just to achieve a specialized set of performance requirements.

The simplest technique to improve machine efficiency and rated power is to increase the machine axial length [160, 161]. However, this strategy is limited due to the standardized frame sizes and in high-efficiency motors it has already been exploited to the fullest. In the following review, the focus will be given to methodologies developed for the topological optimization of radial-flux machines, due to their importance in the industrial and electric mobility applications.

Considering the SCIM applications, many contributions have been dedicated to the shape optimization of the stator slots [162, 163], rotor bars [164–172], or both [173, 174]. In [162], the optimal shape of the stator slots is achieved by the conjugate gradient method for efficiency and maximum torque ratio, where the design variables are four geometric parameters that control the height and the width of the slots. For each candidate, FEA is used to perform harmonic equivalent circuit analysis for a fixed slip and to calculate the motor performance. The winding conductors gauge is adjusted to a specified slot fill factor, and the stator winding losses change with the slot cross-sectional area. In [163], sensitivity analysis of flux density at stator tooth and back iron is carried out by FEA using three different slot profiles for maximum efficiency and maximum power factor. It has been concluded that higher efficiency is achieved by compromising the power factor and vice-versa. In [164], the rotor bar shape defined by geometrical parameters is optimized by a Gaussian multiobjective PSO algorithm. The candidates are firstly evaluated by equivalent circuit analysis (100 thousand solutions evaluated). Then, the height and width of the selected optimal bar shape is refined with FEA. The objectives are the maximization of maximum torque and the minimization of the slip at maximum torque, for the design of a class-D motor. In [165], the starting torque is increased by 12% through the lumped parameter sensitivity analysis of a general layered rotor bar, the resulting design was verified by FEA with no degradation of the efficiency of the new design. In [166], the computational performance and the output solutions obtained by a large range of optimization algorithms for the parametric design

optimization of a SCIM are compared for benchmark purposes. A GA outperformed the other approaches in terms of the number of nondominated solutions obtained, but it was the most time consuming algorithm with more than 27 hours for 7600 solutions evaluated through FEA. In [167, 170, 171], the parametric shape optimization of closed and open, single and double, rotor bars is conducted using the NSGA-II for the maximization of efficiency at a specified slip and starting torque. The performance of each design was assessed by the computation of the equivalent electric circuit, whose parameters were obtained by AC magnetostatics FEA. The best performance was achieved by the open-double-cage design with a nondominated front featuring a maximum efficiency of 94.2% and a starting torque of 305 N.m. In [169], a non-parametric design of the rotor bars optimization methodology is proposed for the achievement of desired torque-slip characteristics. The optimization was carried out with the augmented Lagrangian method for an AC magnetostatics FEA physical formulation. In [173], a bio-inspired multiobjective metaheuristic is used to optimize the design of both stator and rotor slot geometries in terms of the maximization of the machine efficiency and the minimization the SCIM active parts material costs. An analytical model is used to compute the performance of the designs. The authors considered their model sufficiently precise, as it embodies magnetic saturation and skin effect. The optimizer proposed by the authors was compared with other metaheuristics (NSGA-II and PSO), showing a lower computation time, although a poorer performance according to the number of nondominated solutions generated. In [174], a multiobjective genetic algorithm was used to solve the parametric design optimization of a SCIM stator and rotor slot geometries for maximized efficiency and power factor. Results showed higher efficiency and power factor with wider and shorter stator slots. Conversely, narrower and deeper rotor slots improved the machine efficiency, while wider and shallower rotor slots improved the machine power factor.

Topological optimization of radial-flux synchronous machines, with special relevance to the SynRMs and PMSMs, is addressed using methodologies in a similar manner as to those used for SCIMs. Major contributions presented in the literature generally attain the design requirements by solely manipulating the geometries of the rotor configurations [175–201], where common objectives are related to the efficiency and torque ripple improvements, as well as to the material costs reduction of the active parts, namely the neodymium magnets, which are usually made from very expensive rare-earths.

In [202, 78], the optimal unequal distribution of stator slots is investigated for reduced torque-ripple. In [186], the maximization of torque and minimization of the magnets volume are achieved by inspecting variations in the rectangular shape and depth of the magnets in the rotor. It has been concluded that torque improvement was achieved with longer rather than thicker magnets positioned closer to the rotor surface, which also contributed

to smaller magnet volume. Similarly, in [185], the Taguchi and response surface methods were used to determine the magnet rectangular shape, position and rotor size for optimal PMSM efficiency and power factor. The magnet position showed larger impact on the frequency and power factor than magnet dimensions. In [187], to reduce the torque ripple and permanent magnet losses, while increasing the rated torque, the dimensions of the permanent magnets, the stator slot size, the airgap length, and the rotor structure of a PMSM were optimized with the Kriging model (Gaussian regression based interpolation model). Two current densities of 6 and 18 A/mm^2 were investigated for maximum torque capability. In [188], the height, the angular width and the inner rotor radius of a surface-mounted PMSM were optimized for improved torque capability by the NSGA-II algorithm. In [189], a general magnetization pattern defined by a binary tree is proposed for the torque, efficiency, volume, and torque ripple improvement of a surface-mounted PMSM by a Tabu search algorithm. In [181–183], the shape of permanent magnets and flux barriers are optimized for efficiency, demagnetization tolerance, mechanical stress, cogging torque, and permanent magnet mass improvements. In [201], a step-skew design approach is proposed, where both the length and the skew-angle of different portions of the rotor are investigated for minimal cogging-torque. Focusing on possible methods for the performance evaluation of the candidates, in [176, 186, 177, 190, 191, 184] analytical models are preferred due to low computational effort. In [178], the MEC methodology is employed to solve the optimal shape of flux barriers in the stator back-iron region. In [180], the stator slots and the magnet shapes are investigated and some selected cases are analyzed with FEA to build up a surrogate model. In [192, 179, 193–200], FEA is employed for precision evaluation of detailed design refinement processes.

The conventional rotor design of SynRM as known today, which consists in multiple flux barriers perpendicularly positioned along the quadrature-axis, was proposed by Kostko in 1920. This design is the basis of many new rotor configurations proposed in the literature. In [203], the saliency ratio (flux barriers width / iron slits width) was investigated for the maximization of the machine power factor. An optimal result was achieved by a saliency ratio of 0.5. In [204], a multiobjective GA was employed for the optimization of the flux barriers shape aiming at improving torque ripple and torque density at a specified speed. Similarly, in [205], three stochastic algorithms (DE, SA, and GA) are compared for the optimization of the flux barrier shape to maximize the torque per Joule loss ratio and minimize the torque ripple. Better performance was achieved by the DE algorithm. In [206], a ribless rotor design with optimized flux barriers was proposed to further increase the power factor. In [207], the refinement process of an optimized rotor design for high speed applications was explained. A novel rib structure is proposed for increased torque capability when

compared to conventional designs. Additionally, it is shown that ribless designs promote better machine performance; however, for high speed applications such configurations are unfeasible due to high mechanical stress. Yet, when replacing the air-barriers with a rigid and low permeable material is possible, such as epoxy resin, the advantages of a ribless design can be maintained [208]. Other similar methodologies for optimizing the rotor flux barrier shapes are proposed in [209–212]. Mainly, FEA is employed to obtain the performance of the optimization candidates, but also analytical [207] and MEC methods [212] can be adopted for less time consuming applications. In [212], the genetic algorithm required the evaluation of 2000 candidates for a total of 4 and half days. Novel non-parametric topological optimization methods have been proposed in [104, 213–217] for improved performance and design opportunities of SynRMs, in particular, the on/off method based on the normalized Gaussian network [104]. However, when dealing with such general methods, the objective function has a rather broad distribution of optimal sub-regions in the search space, thus impairing the convergence of the optimizer. Moreover, the resolution of the mesh plays a crucial role on the performance of the solutions obtained and the computational time required, as FEA is preferably used. Generally, these methods generate solutions with thicker flux-paths, as they are more robust against finer distribution of flux-paths that may be represented by peak regions in the search space. To overcome this convergence issue, in [217], the Gabor filter is employed to promote designs with finer flux-paths for increased average torque production with smaller torque ripple. The time required for the complete optimization was approximately six days.

Other relevant topological optimization regarding hybrid technologies have been proposed. In [218], the geometry of the flux barriers and the size of magnets of a five-phase permanent magnet assisted SynRM were optimized with a multiobjective DE algorithm to improve the machine efficiency, the material costs, and the torque ripple. Analogous strategies were developed in [219–221]. In [222], the rotor design optimization of a line-start PM-assisted SynRM was solved to increase the average torque and reduce the torque ripple. The objective function evaluation was carried out by FEA, and the optimization was solved by a multiobjective DE algorithm with a Pareto dominance selection strategy. The design variables were the flux barriers angular position, rotor slots number, angular position of the first rotor slot, depth of the rotor slots, and the rotor tooth width.

With respect to this review on topological optimization of electric rotating machines, the following major observations can be made:

1. Analytical models may be highly imprecise for the operation points relatively far from the reference point of calculations, especially when magnetic saturation is relevant.

2. Methods relying on FEA usually evaluate a rather small number of candidates, thus compromising the search for optimal solutions.

3. Most topological methods are based on parameterized geometrical frameworks, thus diminishing the diversification of solutions.

4. In non-parametric methods the optimization is made for very specific electromagnetic characteristics of the design, such as iron losses and torque ripple, which generally do not reflect the overall machine performance.

5. In SynRM and PMSM optimization applications, a fixed relative position of the rotor against the stator magnetic flux orientation (load angle or phase advance) is usually considered. Therefore, it is possible for some candidates that their fitness values do not meet their real potential, thus negatively affecting the optimization convergence.

Therefore, to overcome these limitations, in this chapter novel topological optimization methodologies are proposed for a more general and systematic design of the SCIM, SynRM, and PMSM radial-flux motor technologies.

4.2 Hyper-decision-variable topological optimization

Aiming at more general topological optimization strategies that can provide significant assistance in the pre-design of radial-flux SCIM, PMSM and SynRM, the methodologies summarized in Fig. 4.1 are proposed.

4.2.1 Topological optimization of the stator

The stator is regarded equivalently throughout the optimization strategies of the three machines proposed (Fig. 4.1). The stator design is dealt with parameterized geometrical entities, since no relevant designs besides the simple straight and regular thoothed stator configuration are expected for improved machine performance. Therefore, the geometrical parts listed in Table 4.1 are proposed for the vast set of decision variables. Fixed parameters are the stator outer radius, stack length, and the tooth tip height, which is equal to 10% to the total tooth height ($h_{\mathrm{t,s}}$).

4.2.2 General topological optimization of the rotor

Throughout the proposed optimization methodologies, a non-parametric design region and a back-iron region is assigned to the rotor. Table 4.2 lists the geometrical entities of the rotor

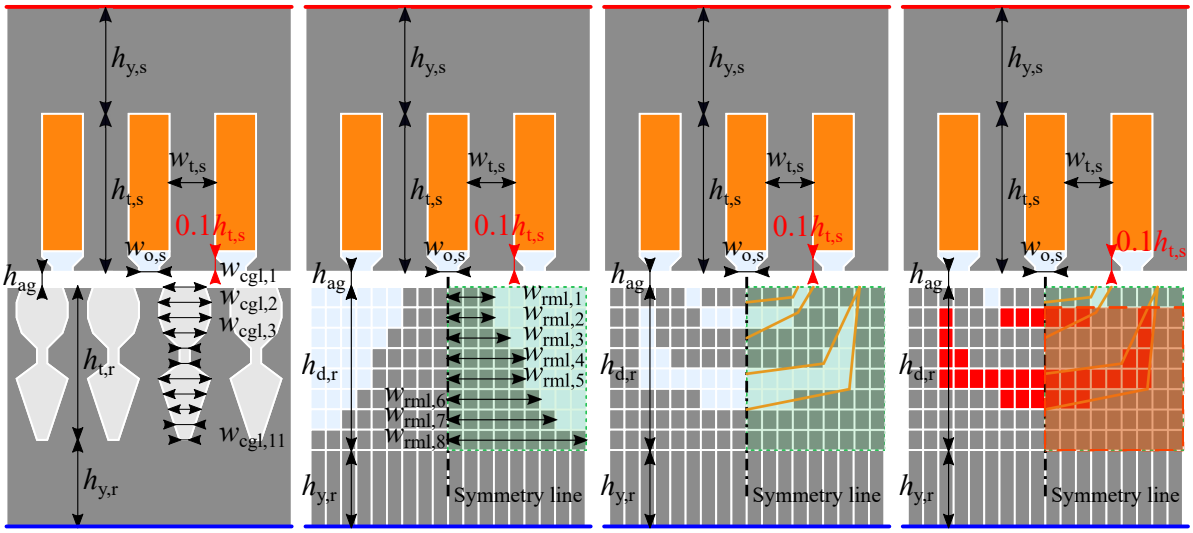

Figure 4.1 Topological design strategies: (a) definition of the decision variables for the SCIM; (b) definition of the decision variables for the SynRM with salient-pole rotor; (c) definition of the decision variables for the SynRM with air-barriers; (d) definition of the decision variables for the PMSM.

Table 4.1 Decision variables set of the stator topological optimization.

Geometrical part	**Symbol**	**Major impacts**
Back-iron height	$h_{y,s}$	weight, delivered power, magnetic saturation, iron losses
Tooth height	$h_{t,s}$	weight, winding Joule losses
Tooth width	$w_{t,s}$	winding Joule losses, delivered power, magnetic saturation, iron losses
Slot opening width	$w_{o,s}$	delivered power

general configuration. The shaft radius is not regarded by the complete set of the decision variables; however, a desired minimum limit can be set to all related height geometrical entities ($h_{y,s}$, $h_{t,s}$, h_{ag}, $h_{t,r}$ or $h_{d,r}$, and $h_{y,r}$).

Table 4.2 Decision variables set of the general rotor topological optimization.

Geometrical part	**Symbol**	**Major impacts**
Airgap	h_{ag}	delivered power, power factor, leakage magnetic flux
Design region height	$h_{t,r}$ or $h_{d,r}$	weight
Back-iron height	$h_{y,r}$	weight

4.2.3 Topological optimization of squirrel-cage rotors

The strategy for a non-parametric design of the squirrel-cage is displayed in Fig. 4.1a. In the design domain any straight toothed geometry can be replicated by a finite set of layers with variable widths and uniform height, thus the larger the number of layers the higher the resolution. The minimum width of the layer defining the bars geometry ideally should be zero, to allow for the design of multiple cages. However, the maintenance of the mesh coherence is fundamental, thus a very small value for the minimum layer width, such as 1E-9 m, is set instead. Likewise, the bar maximum layer widths should be defined in such a manner that the tooth and bar elements never overlap each other. Therefore, $w_{\mathrm{cgl},j} = k_{\mathrm{alw}} r_{\mathrm{cgl},j} \times 2\pi/Z_{\mathrm{r}}$, where $r_{\mathrm{cgl},j}$ is the top radius of the j^{th} layer, Z_{r} is the rotor number of slices or bars, and k_{alw} is a factor that guarantees a minimal tooth width (e.g. $k_{\mathrm{alw}} = 0.95$).

4.2.4 Topological optimization of reluctance rotors

The On/Off methodology is the most general technique that can be applied in the topological optimization of rotor, since any design can be replicated by the appropriate selection of the elements of a discretized mesh. For this reason, the implementation of this methodology is highly desirable, thus a Differential Evolution based optimization strategy for the maximization of efficiency and power density was developed. However, the optimization results showed poor convergence. In fact, only by adding a feasible design to the initial population, the algorithm is able to converge to normal standards of performance, but design diversification is still poor.

This convergence issue was mitigated by the following quasi-non-parametric design strategies proposed: one strategy is dedicated to the design of salient-pole rotor configurations, generally adopted in switched reluctance machines; and the other strategy is dedicated to the design of rotor configurations featuring air-barriers. In both proposed design strategies, an active design region, corresponding to one half of a pole and a back-iron region, is used to define the rotor topology.

With respect to the design of the pure salient-pole rotor configuration, the design is made by the manipulation of stacked layers with variable widths, as depicted in Fig. 4.1b. For symmetry reasons, the area corresponding to half of a pole is assigned to the active design region (green region in Fig. 4.1b). The order of dealing with the layer widths is made from the top to the bottom layers, where the minimal width of a layer corresponds to the width of its predecessor layer. The maximum width allowed corresponds to half of a pole arc, such that $w_{\mathrm{rml},j} = r_{\mathrm{rml},j} \times \pi/p$, where $r_{\mathrm{rml},j}$ is the middle radius of the j^{th} layer.

Regarding the design of air-barrier reluctance rotor configurations, geometry variations result from the subtraction of regions defined by auxiliary poly-lines, as illustrated in Fig. 4.1c. The strategy for the definition of an air-barrier regions and the decision variables controlling them is depicted in Fig. 4.2. Each air-barrier is defined by a pair of auxiliary poly-lines, each comprising two linear segments. These segments consist of a set of five decision variables. The first segment is defined by an initial end-point placed on the pole radial symmetry line, a slope and a length. Then, the second segment is defined by the second end-point of the first segment and by an additional slope and length. Finally, an air-barrier region is assigned if two conditions are simultaneously verified for a given tangential position: (i) the space between the first and the second auxiliary poly-lines is larger than one fundamental sector; (ii) the second auxiliary poly-line stays under the first. Depending on the initial number of air-barriers selected, the resulting design may not reflect that total of air-barriers. Moreover, this strategy can also generate salient-pole rotor configurations as represented in the previous design strategy.

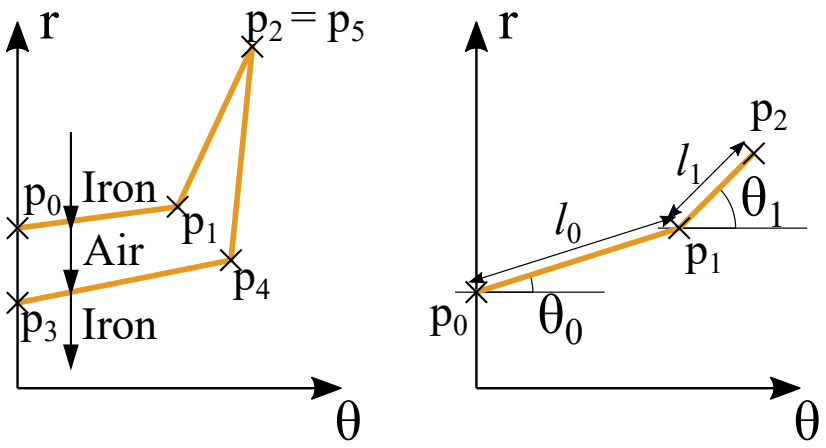

Figure 4.2 Definition of air-barriers by design auxiliary poly-lines. The rotor design domain is initialized with only core elements. An air-barrier region is assigned if two conditions are simultaneously verified for a given tangential position: (i) the space between the first (p_0, p_1 and p_2) and the second (p_3, p_4 and p_5) auxiliary poly-lines is larger than one fundamental sector; (ii) the second auxiliary poly-line stays under the first. An auxiliary poly-line is defined by two linear segments: a point placed on the pole symmetry line (p_0), a slope (θ_0) and a length (l_0) define the first segment; then, the second segment is define by the second end-point of the first segment, and another slope (θ_1) and length (l_1).

4.2.5 Topological optimization of permanent magnet assisted reluctance rotors

The strategy used in the definition of air-barriers is employed in the topological optimization of permanent magnet assisted reluctance rotors. However, in this case, an additional permanent magnet region (red region in Fig. 4.1d) redefines air elements as a permanent magnet with a desired orientation and remanent magnetization.

4.2.6 Multiobjective topological design optimization approach

A general optimization scenario is adopted for the design optimization of the electric rotating machines previously mentioned. Therefore, the maximization of the efficiency and power density are set as the two objectives of the optimization. For the sake of feasibility of the thermal characteristics of the optimized machine, the current density of the winding conductors is restrained for a maximum of 10 A/mm^2, and the whole machine is regarded at a temperature of 100 °C.

The optimization is carried out by the same Differential Evolution algorithm proposed in chapter 2 for the design optimization of the stator winding. The flowchart describing the SCIM optimization strategy is depicted in Fig. 4.3 and the flowchart describing the SynRM and PMSM optimization strategies is depicted in Fig. 4.4. Despite the different vectors of decision variables, controlling the design of each machine technology, the optimization strategy is identical and it is summarized in the following steps:

1. **Initialization:** set the machine design parameters and the design variables vector. Initialize the algorithm controlling parameters, for all the optimization scenarios a population of 12 individuals, a crossover probability of 0.95, a scaling factor of 0.75, and a maximum number of 200 iterations was set. Randomly generate of initial population.

2. **Mutation and Crossover:** mutate the parent population with a suitable mutation operator, the DE/Rand/1/Bin mutation operator resulted satisfactory for the different optimization scenarios.

3. **Fitness assessment:** the fitness of each machine candidate of the parent and offspring populations are assessed based on their efficiency and power density values, which are maximized at an unknown operation point. On one hand, for the SCIM optimization scenario, this operation point is determined by the maximum efficiency operation point that can be found in a range of slip values. The slip interval assessed ranged from 0.5%

to 7.5% with a step of 0.5%. Therefore, the fitness assessment of each SCIM candidate requires 15 time-harmonic simulations. On the other hand, for the PMSM and SynRM optimization scenarios, this operation point is determined by the maximum motor torque which the machine is able to produce. The torque maximizing phase advance or load angle is obtained by searching, for a suitable range of phase advance values, the most negative torque evaluated by a magnetostatics analysis of the candidate. In the following case studies, the search range consists in steps of 5 electrical degrees. Therefore, the fitness assessment of each PMSM and SynRM candidates requires the evaluation of 72 and 36 magnetostatics analysis, respectively, and a time-step analysis of 60 steps, corresponding to a full electrical cycle. To improve the computational time, a pool of parallel cores is created to solve different candidates simultaneously. The maximum number of candidates that can be solved simultaneously corresponds to the number of the CPU cores.

4. **Selection of the best solutions:** normalize the fitness value of the candidates with respect to constraints violation as in [98], and select the most fitted individuals according to the NSGA-II algorithm [48].

5. **Population stagnation avoidance:** in case of population stagnation perform a regeneration of the population as in [97].

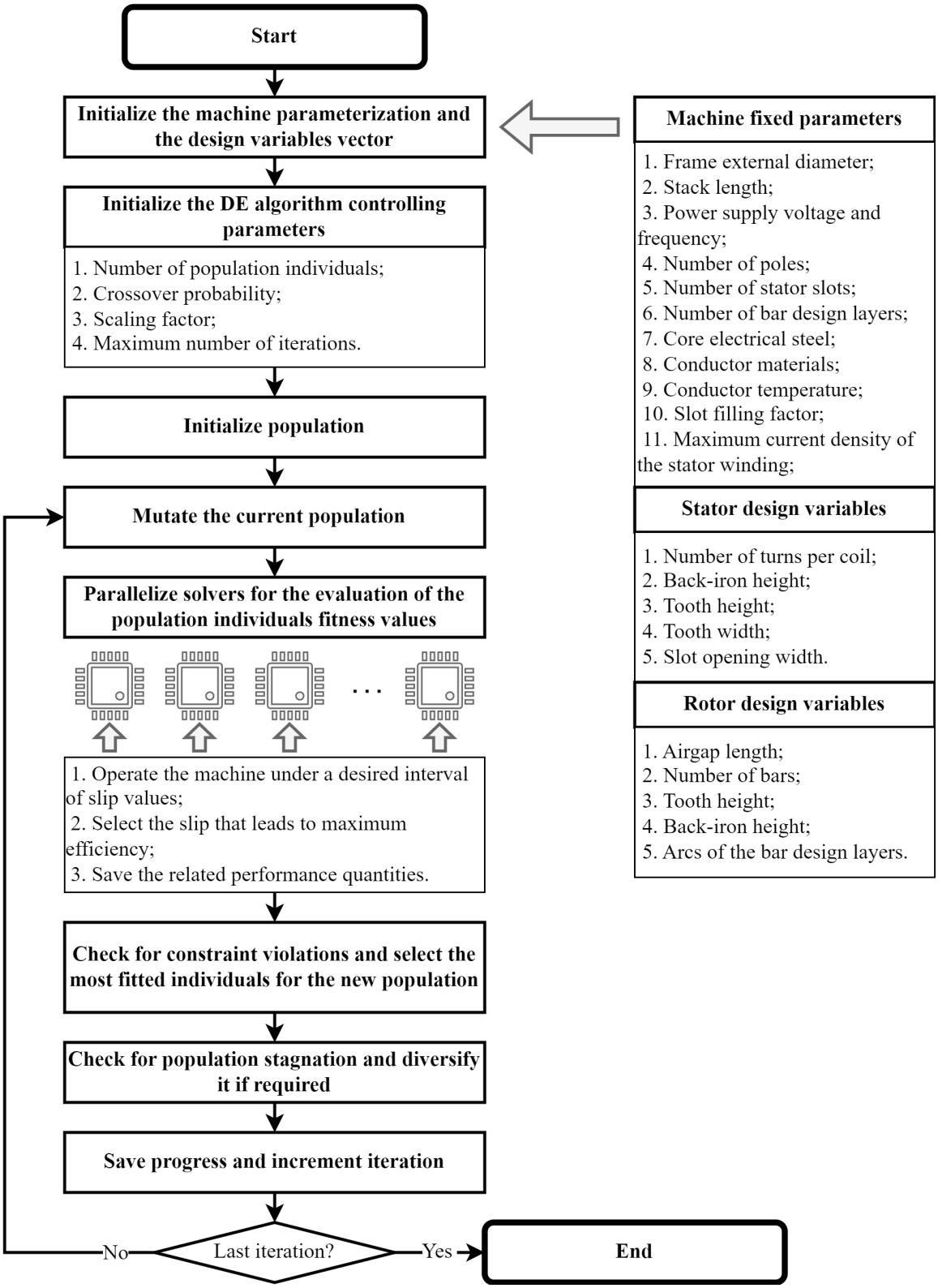

Figure 4.3 SCIM optimization strategy flowchart.

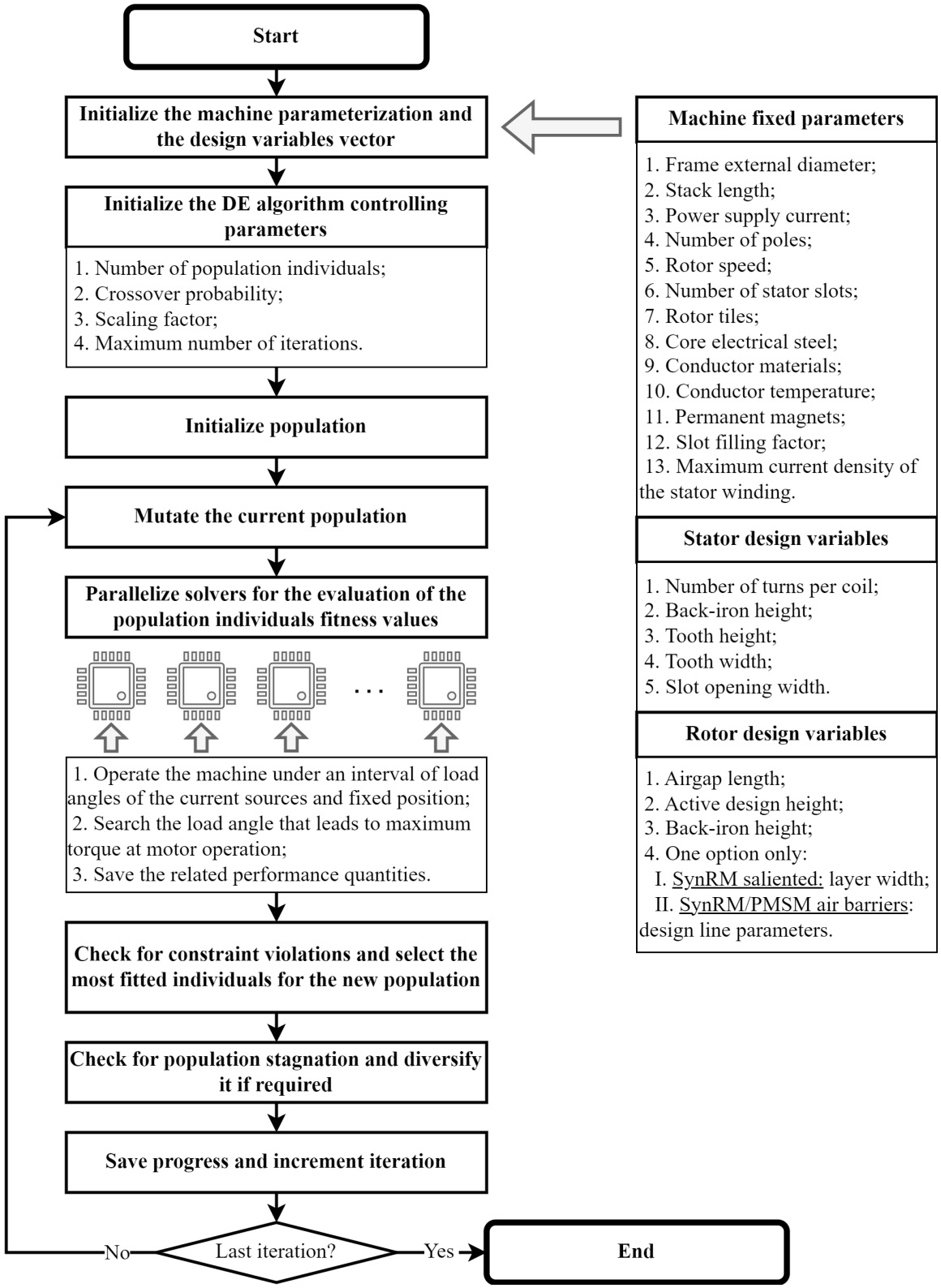

Figure 4.4 SynRM and PMSM optimization strategy flowchart.

4.3 Case studies

In the following case studies, the topological optimization strategies here proposed are applied to different machine technologies. The optimization is conducted to maximize the machine efficiency and power density. Additionally, the maximum current density applied to the stator winding conductors is restrained to 10 A/mm^2.

In each optimization, the individuals generated throughout the iterations are saved in an archive for a comprehensive analysis of the algorithm performance. The electromagnetic performance of two candidates of the archive that realize the ends of the resulting nondominated front is compared with FEA for the comprehension of the full methodology limitations in terms of robustness and accuracy. The algorithm setup for all the optimization scenarios are: population of 12 individuals, scaling factor of 0.75 (mutation operator DE/Rand/1/Bin), crossover probability of 0.95, and stopping criterion of 200 iterations. A computer with 4 CPU cores running at 3.8 GHz and 16 GB of RAM is used.

4.3.1 Topological optimization of a 2.7-kW squirrel-cage induction machine

In this study, the performance improvement of the SCIM tested in Chapters 2 and 3 which can be achieved with the proposed methodology is evaluated and quantified. The optimization fixed setup of this case study is provided in Table 4.3 and the design decision variables parameterization is provided in Table 4.4.

The optimization was completed in 2 hours and 16 minutes. The evolution of the optimization and the resulting nondominated front are displayed in Fig. 4.5. The initial and selected designs decision variables are provided in Table 4.5. A comparison of the geometries of the initial design and the optimal selected solution is displayed in Fig. 4.6. The performance analyses of the initial and optimal designs are provided in Fig. 4.7.

A diversified set of improved solutions was obtained by the proposed optimization methodology, as it can be observed in Fig. 4.5. In fact, efficiency can be improved by more than 2 p.p., while power density can almost quadruple with respect to the initial design. The optimizer finds more effectively the efficient solutions than the power-dense solutions, as a denser region of solutions near the more efficient end of the nondominated front emerge from Fig. 4.5. This can be justified by the pressure the selection mechanism puts by selecting the most efficient operating point, instead of the most power-dense operating point within the allowed slip range.

The selected solution has increased efficiency by 1 p.p. and almost doubled power density. This was mainly achieved by the reduction of the winding number of the turns. However,

other relevant geometrical modifications were achieved by the optimizer. A much larger slot area stands out in the optimized design, as the optimizer clearly recognized the relevance of the stator winding Joule losses and found a good compromise between this loss component and the iron loss component. In fact, the iron losses of the optimized design more than double, while the stator winding and rotor bar Joule losses are maintained, even though the input power and current nearly doubled, with respect to the initial design (Fig. 4.7). Further, the unusual shape of the optimized rotor bars evidences the difficulty or the insensibility of the methodology to generate smoother shapes. The resulting shallower pear shape of the optimized design rotor bars features larger top and finer bottom widths, thus promoting increased torque production for low slip values. Both designs reach maximum efficiency at the slip of 1.25%, but the low-slip linear operating region of the optimized design has a higher slope and the starting torque was largely attenuated, since the bar resistance was reduced.

Table 4.3 Optimization fixed setup of the 2.7-kW SCIM case study.

Property	**Value**	**Unit**
Outer radius	110	mm
Strack length	130	mm
Poles	4	
Stator slots	36	
Bar design layers	20	
Power supply voltage	400	V
Power supply frequency	50	Hz
Slot fill factor	0.5	
Electrical steel	M250-50A	
Winding material	copper	
Bar conductor	aluminium	
Maximum current density	10	A/mm^2

Table 4.4 Design decision variables setup of the 2.7-kW SCIM case study.

Property	Min. Value	Max. Value	Unit
Turns	40	70	
Stator backiron height	10	33	mm
Stator tooth height	10	30	mm
Stator tooth width	1	5	mm
Stator slot opening width	1	5	mm
Airgap length	0.4	1.5	mm
Rotor bars	20	48	
Rotor design height	10	25	mm
Rotor back-iron height	10	20	mm
Bar layer width	20	99.999	%

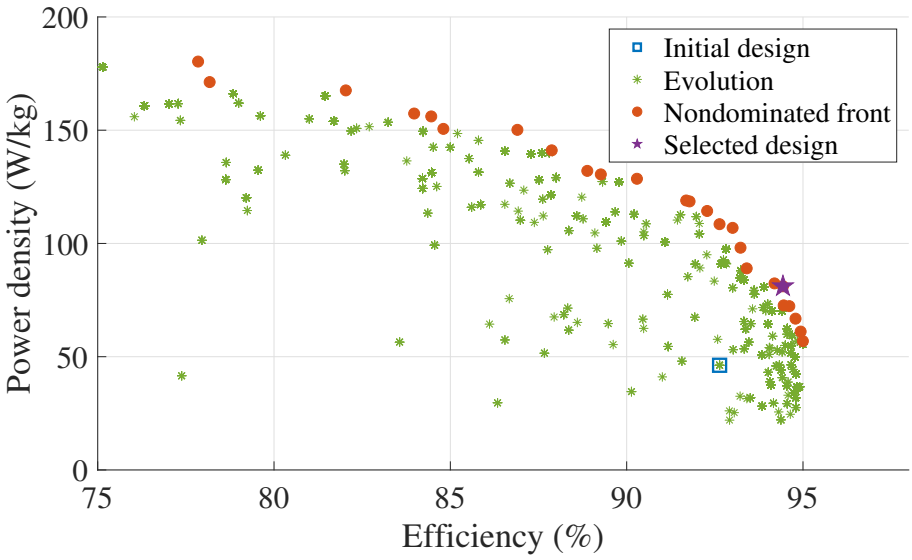

Figure 4.5 Optimization evolution and resulting nondominated front of the SCIM previously analyzed in Chapters 2 and 3.

Table 4.5 Design decision variables of the initial and selected optimal design of the 2.7-kW SCIM case study.

Property	Initial design	Optimized design	Unit
Turns	52	43	
Stator backiron height	29.50	16.86	mm
Stator tooth height	18.00	25.58	mm
Stator tooth width	4.80	4.62	mm
Stator slot opening width	3	2.46	mm
Airgap length	0.6	0.52	mm
Rotor bars	28	28	
Rotor design height	22.5	14.92	mm
Rotor back-iron height	15.4	15.63	mm

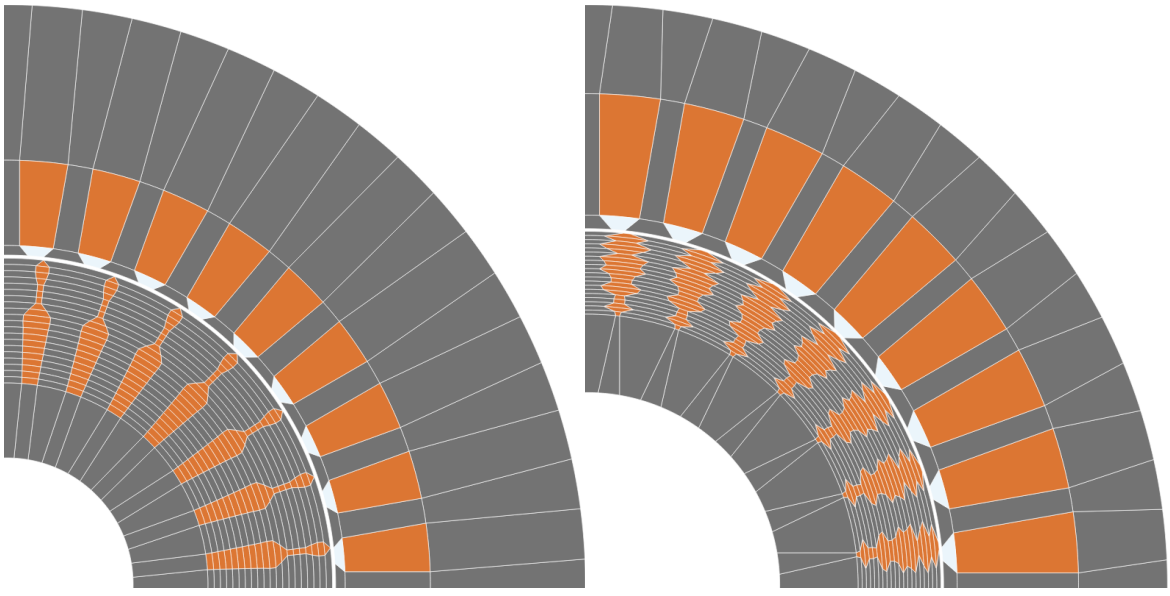

(a) (b)

Figure 4.6 MEC meshing of the solutions of the SCIM optimization displayed in Fig. 4.5: (a) initial design; (b) selected nondominated solution.

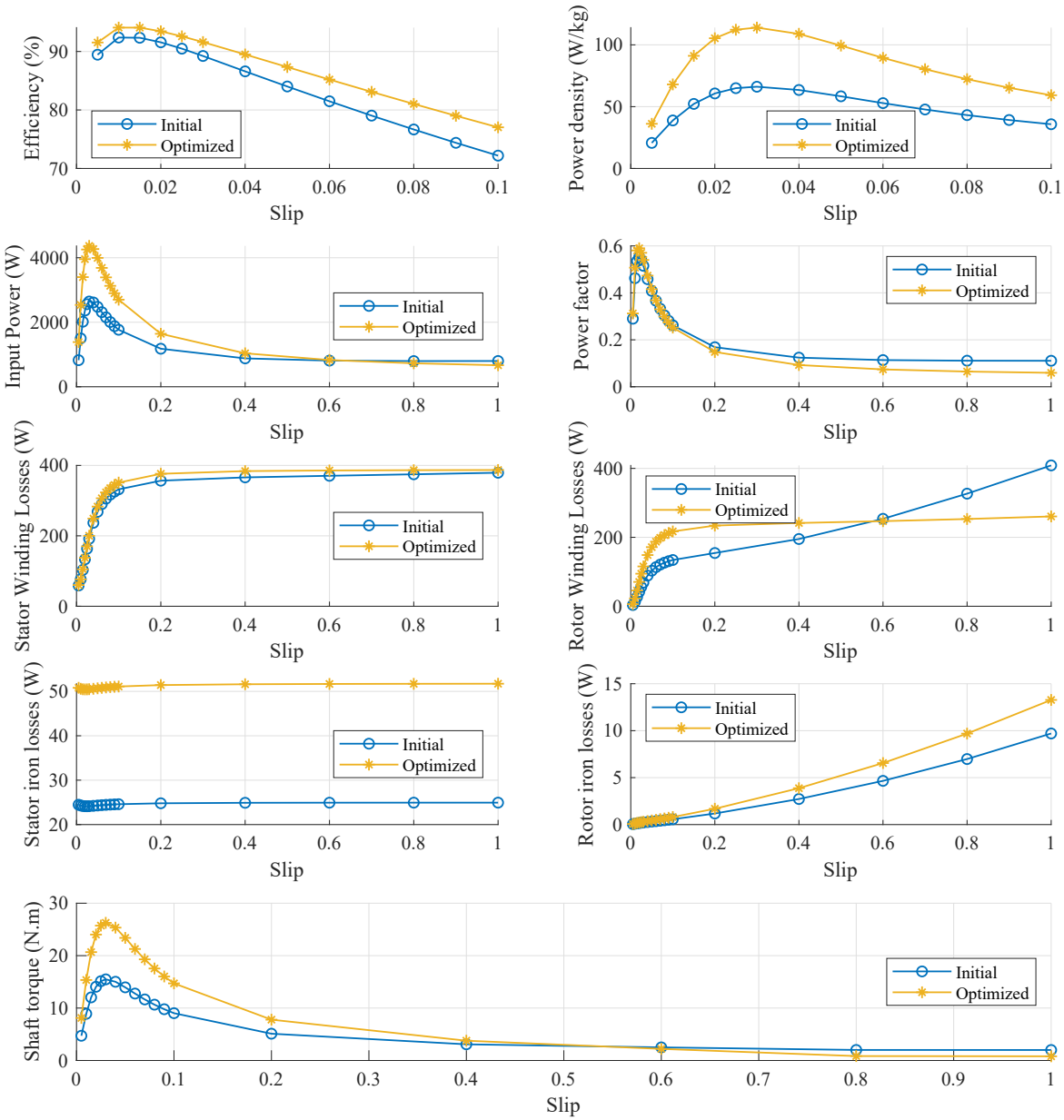

Figure 4.7 Performance curves of (a) the initial design and (b) the optimized SCIM design displayed in Fig. 4.5.

4.3.2 Comparison of topological optimization of different machine technologies

The following case studies demonstrate the applicability of the different topological optimization techniques proposed in this chapter, namely SCIM, SynRM with salient-poles, SynRM with air-barriers, and PMSM with air-barriers. These different machine technologies are optimized for the maximization of efficiency and power density. The housing volume is fixed for the different machine technologies to fairly assess their potential. The main characteristics of the machines used in the following case studies are provided in Table 4.6.

Table 4.6 Optimization fixed setup of the topological optimization case studies for the different machine technologies evaluated.

Property	**Value**	**Unit**
Outer radius	160	mm
Strack length	100	mm
Poles	4	
Stator slots	36	
Bar design layers	20	
Rotor tangential tiles	40	
Rotor radial tiles	10	
Power supply voltage	400	V
Power supply frequency	50	Hz
Slot fill factor	0.5	
Electrical steel	M250-50A	
Winding material	copper	
Bar conductor	aluminium	
Maximum current density	10	A/mm^2

Squirrel-cage induction machine topological optimization

In the SCIM topological optimization case, the design decision variables parameterization is defined as described in Table 4.7.

The optimization was completed within 2 hours and 24 minutes. The evolution of the optimization and the resulting nondominated front are displayed in Fig. 4.8. The design decision variables of the most efficient and the most power-dense nondominated solutions are provided in Table 4.8. A comparison of the geometries of the initial design and the selected solution is displayed in Fig. 4.9. The MEC and FEA performance analyses of the

most efficient and the most power-dense designs are compared in Fig. 4.10 and Fig. 4.11, respectively.

A diversified set of solutions was obtained by the proposed optimization methodology. Once again, the optimizer finds more effectively efficient solutions than power-dense solutions, which stands out by the denser region of solutions that appear near the right end of the nondominated front. The solutions clustering each end of the nondominated front have the following features:

1. High efficiency solutions have narrower and taller stator teeth, so the slot cross section area is increased to allow for the reduction of stator winding Joule losses.

2. The back-iron height is larger in the cluster of the high efficiency solutions.

3. The higher number of turns and narrower airgap is also a characteristic of the high efficiency solutions.

4. High power density solutions have smaller and wider rotor bars, thus having increased rotor resistance.

5. High power density solutions are more compact and lighter, since the resulting space reserved for the shaft is larger.

In the solutions depicted in Fig 4.9 and in the remaining nondominated solutions, a clear definition of multi-cage rotor configurations was not achieved. In fact, the severe unaligned widths of the rotor bar layers may evidence the difficulty of the methodology to find more conventional designs. More likely, the optimizer is only dealing with the bar cross sectional area to reach the best rotor resistance value. Conceivably, if considering the optimization of additional operating points then a smoother shape or at least a more controlled variation of the layers widths would be perceived by the optimizer, especially in high slip operating conditions where the induced eddy currents have great impact. The machine performance accuracy of the MEC method was poor when compared to the FEA results, especially for the higher power density solutions. This can be explained by the coarse mesh of the MEC method: the narrow bottom and top arcs of the elements 5 and 6, respectively, of Fig. 4.11, creates low reluctance path which is not accounted for by the average widths of both those elements. Converesely, the finer meshing in FEA (Fig. 4.11) accounts much better for the magnetic shielding occurring between those elements. Therefore, this increases the MEC and FEA discrepancies, especially in high slip operating conditions.

Table 4.7 Design decision variables setup of the SCIM case study.

Property	Min. Value	Max. Value	Unit
Turns	10	100	
Stator backiron height	10	43	mm
Stator tooth height	20	45	mm
Stator tooth width	3	10	mm
Stator slot opening width	1	7	mm
Airgap length	0.4	1.5	mm
Rotor bars	20	48	
Rotor design height	15	35	mm
Rotor back-iron height	10	35	mm
Bar layer width	20	99.999	%

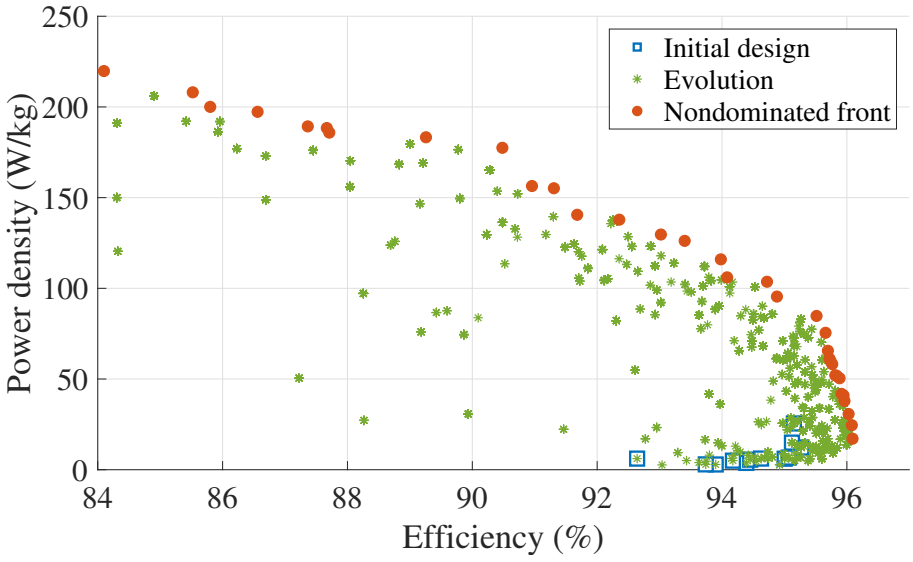

Figure 4.8 Optimization evolution and resulting nondominated front of a SCIM technology packed in a cylinder with 160 mm of radius and 100 mm of length.

Table 4.8 Design decision variables of the most efficient and power-dense designs of the SCIM case study.

Property	Most efficient design	Most power-dense design	Unit
Turns	39	13	
Stator backiron height	39.16	32.24	mm
Stator tooth height	34.28	26.30	mm
Stator tooth width	6.11	9.35	mm
Stator slot opening width	2.29	3.75	mm
Airgap length	0.50	0.89	mm
Rotor bars	32	32	
Rotor design height	34.82	20.28	mm
Rotor back-iron height	34.74	32.25	mm

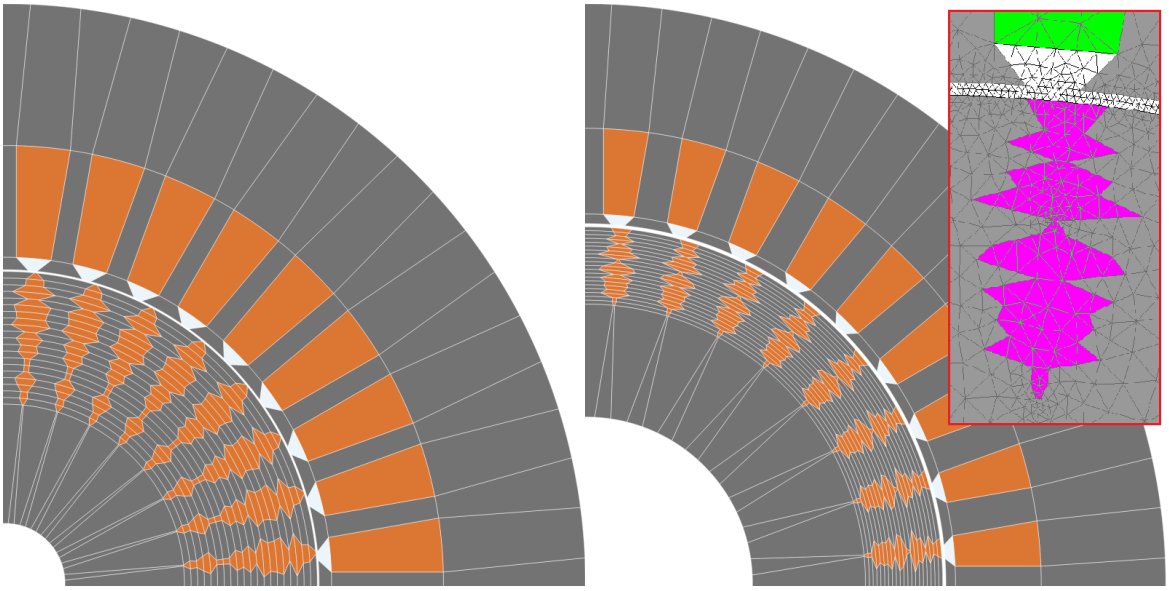

(a) (b)

Figure 4.9 MEC meshing of the solutions of the SCIM optimization displayed in Fig. 4.8: (a) nondominated solution with maximum efficiency; (b) nondominated solution with maximum power density (the meshing of the FEA model is displayed to evidence the low resolution of the MEC mesh, when the average magnetic flux path created by elements with such uneven top and bottom arcs is not sufficient to model high flux leakages in the nearby regions).

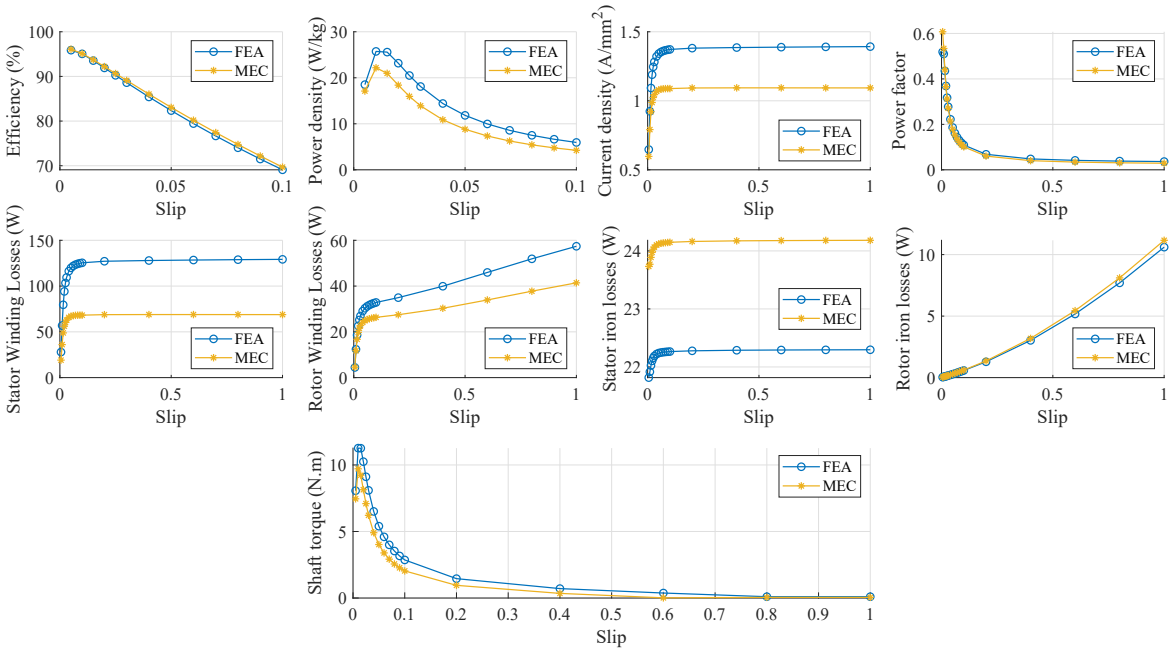

Figure 4.10 Verification of the SCIM performance curves of the nondominated solution with maximum efficiency of Fig. 4.8.

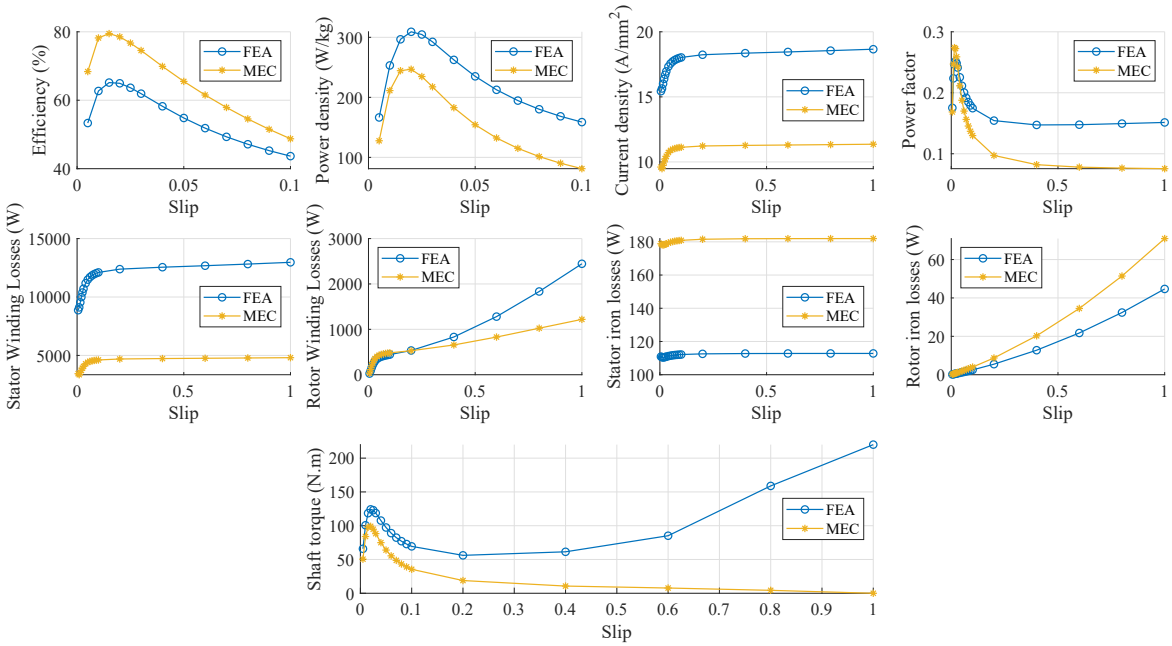

Figure 4.11 Verification of the SCIM performance curves of the nondominated solution with maximum power density of Fig. 4.8.

Salient pole synchronous reluctance machine topological optimization

The design decision variables parameterization of the SynRM with salient-pole topological optimization is defined as described in Table 4.9.

The optimization was completed within 8 hours and 42 minutes. The evolution of the optimization and the resulting nondominated front are displayed in Fig. 4.12. The design decision variables of the most efficient and the most power-dense nondominated solutions are provided in Table 4.9. A comparison of the geometries of the high efficiency and high power density selected solutions is displayed in Fig. 4.13. The MEC and FEA performance analyses of the high efficiency and high power density selected solutions are compared in Fig. 4.14 and Fig. 4.15, respectively.

A diversified set of solutions was obtained by the proposed optimization methodology. In opposition to the previous SCIM optimization cases, a more uniform distribution of the candidates along the nondominated front is observe. In this case, the fitness of each candidate is calculated for the phase advance which maximizes torque. The solutions clustering each end of the nondominated front have the following features:

1. High efficiency solutions have narrower and taller stator teeth, so the slot cross section area is increased to allow for the reduction of stator winding Joule losses.

2. Generally, the back-iron height is larger in the cluster of the high power density solutions.

3. The lower number of turns and the narrower airgap is also a characteristic of the high efficiency solutions.

4. Both clusters of solutions have similar pole saliency (rotor pole surface spans practically the same number of stator teeth), and the depth of the saliency. However, in high power density designs, generally the variation of the pole saliency depth takes place in the elements rather close to the pole surface.

5. Generally, high power density solutions are the lightest machine designs.

In this case, the MEC performance simulation resulted satisfactorily accurate when compared to the FEA results, as depicted in Figs. 4.14 and 4.15.

Table 4.9 Design decision variables setup of the salient-pole SynRM case study.

Property	Min. Value	Max. Value	Unit
Current	20	50	A
Turns	10	40	
Stator backiron height	10	43	mm
Stator tooth height	20	43	mm
Stator tooth width	3	11	mm
Stator slot opening width	1	7	mm
Airgap length	0.4	2	mm
Rotor design height	25	50	mm
Rotor back-iron height	5	20	mm
Pole layer incremental width	0	100	%

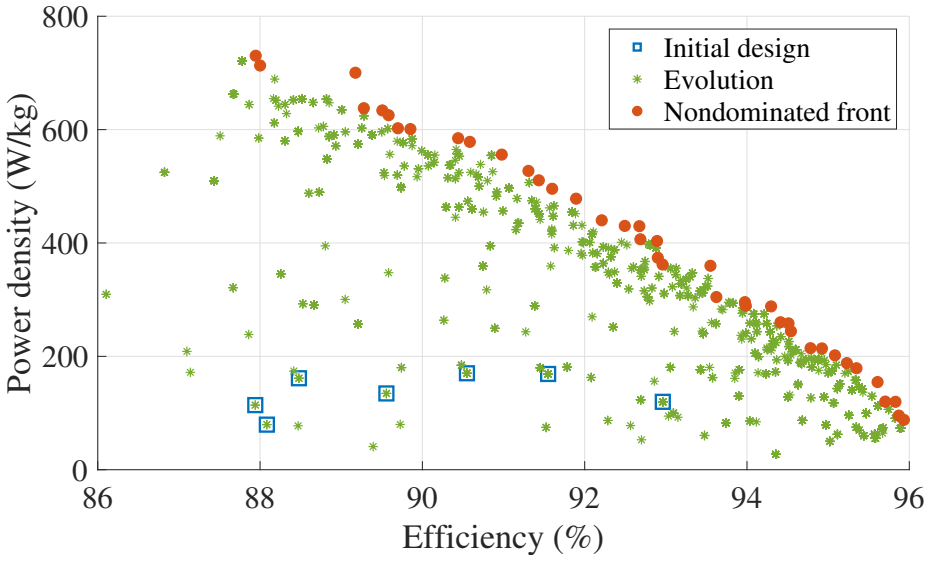

Figure 4.12 Optimization evolution and resulting nondominated front of a SynRM with salient-pole rotor packed in a cylinder with 160 mm of radius and 100 mm of length.

Table 4.10 Design decision variables of the most efficient and power-dense designs of the salient-pole SynRM case study.

Property	Most efficient design	Most power-dense design	Unit
Current	22.35	49.11	A
Turns	17	40	
Stator backiron height	31.90	32.72	mm
Stator tooth height	42.70	40.53	mm
Stator tooth width	7.47	10.97	mm
Stator slot opening width	1.95	4.98	mm
Airgap length	0.41	1.32	mm
Rotor design height	40.08	49.20	mm
Rotor back-iron height	19.74	19.40	mm

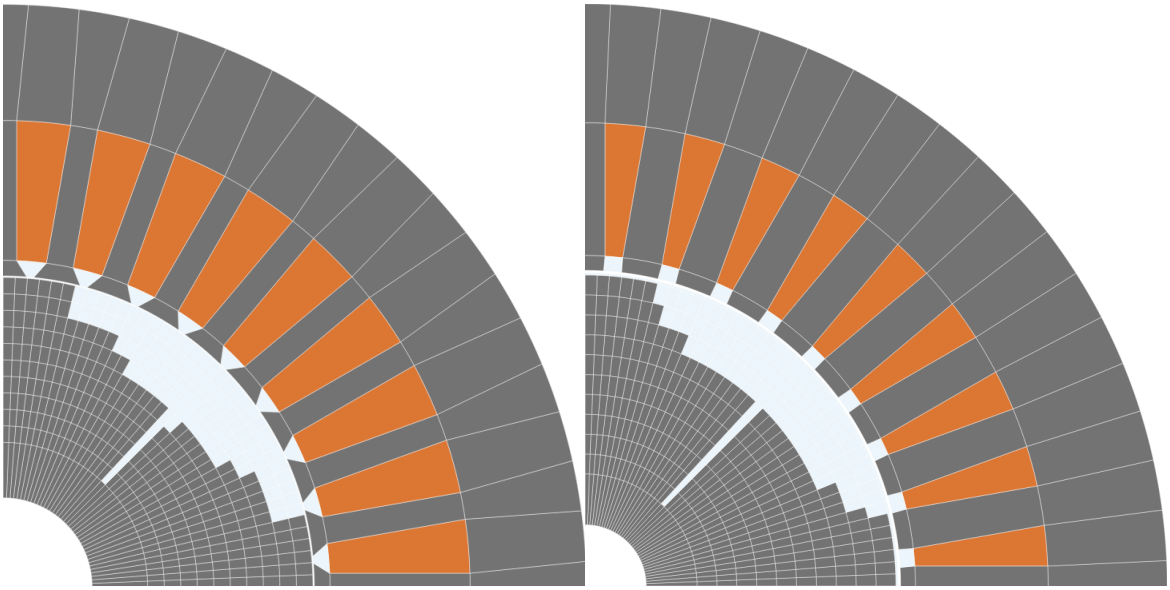

(a) (b)

Figure 4.13 MEC meshing of the solutions of the SynRM optimization displayed in Fig. 4.12: (a) nondominated solution with maximum efficiency; (b) nondominated solution with maximum power density.

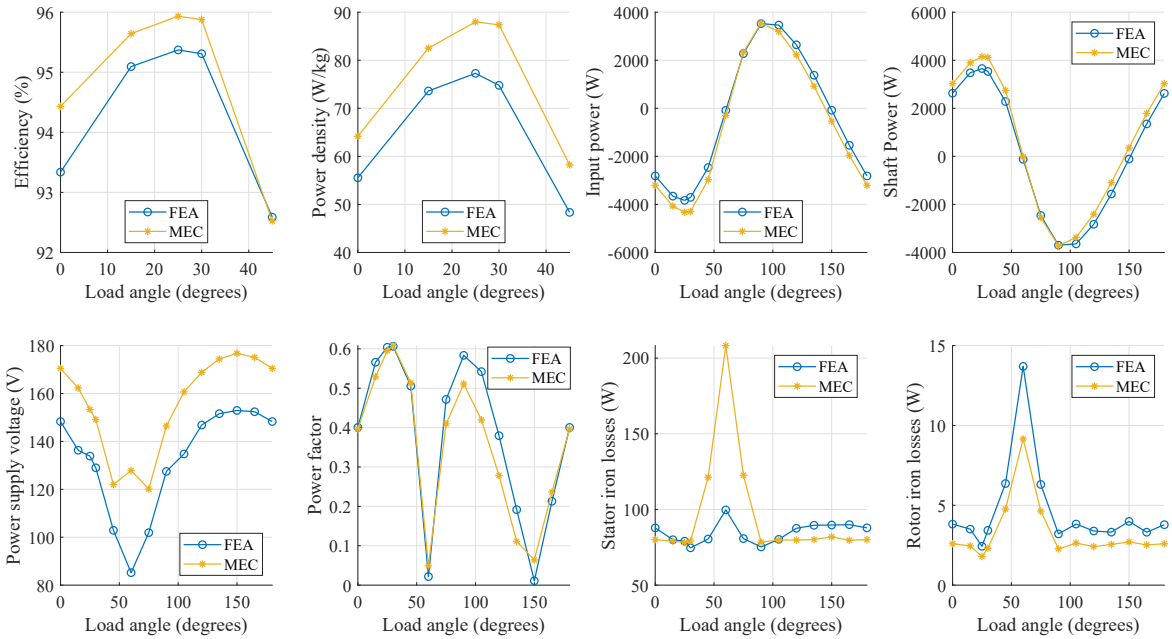

Figure 4.14 Verification of the SynRM performance curves of the nondominated solution with maximum efficiency of Fig. 4.12.

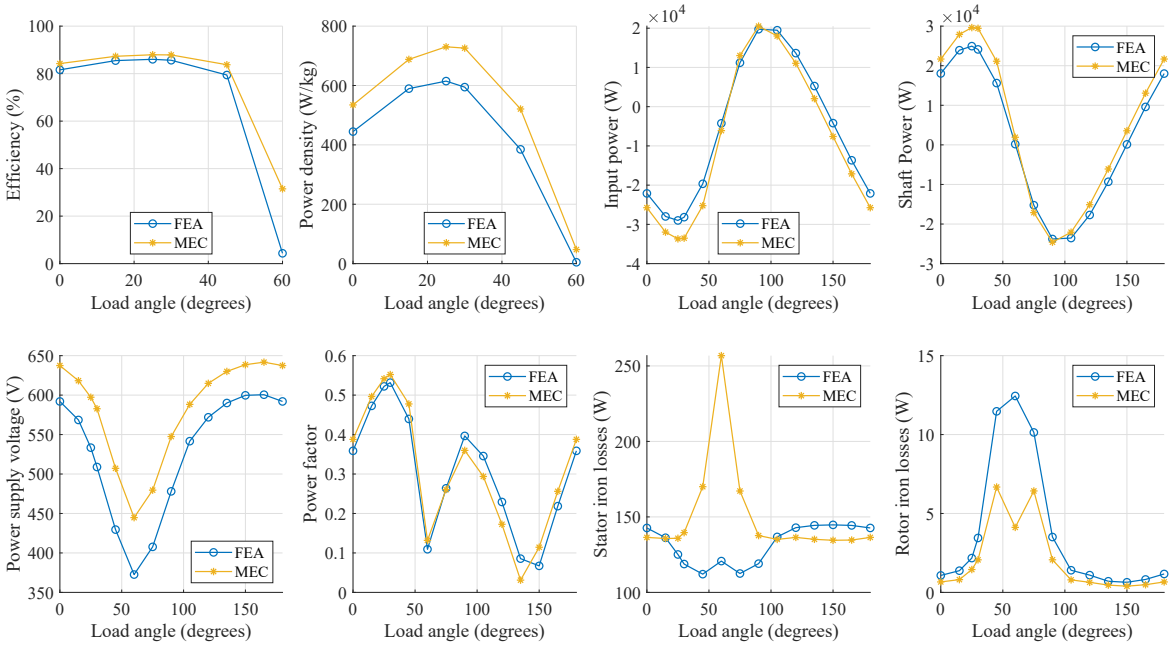

Figure 4.15 Verification of the SynRM performance curves of the nondominated solution with maximum power density of Fig. 4.12.

Air-barrier synchronous reluctance machine topological optimization

The parameterization of the design decision variables for the topological optimization of the SynRM with air-barriers was defined as described in Table 4.9. The optimization strategy adopted in this case study is the same as illustrated in Fig. 4.1c.

The optimization was completed within 8 hours and 37 minutes. The evolution of the optimization and the resulting nondominated front are displayed in Fig. 4.16. The design decision variables of the most efficient and the most power-dense nondominated solutions are provided in Table 4.11. A comparison of the geometries of the high efficiency and high power density selected solutions is displayed in Fig. 4.17. The MEC and FEA performance analyses of the high efficiency and high power density selected solutions are compared in Fig. 4.18 and Fig. 4.19, respectively.

A diversified set of solutions was obtained by the proposed optimization methodology. However, in this case, a much less dense and more sparse region of candidates is populating the nearby space of the resulting nondominated front. This can be result of the low resolution of the mesh employed, meaning that for small changes of the decision variables the resulting geometry is maintained, thus negatively affecting the convergence characteristics of the optimizer. The solutions clustering each end of the nondominated front have the following features:

1. High efficiency solutions have narrower and taller stator teeth, so the slot cross section area is increased to allow for the reduction of stator winding Joule losses or to compensate solutions with higher ampere.turn value.

2. Generally, the back-iron height is larger in the cluster of the high power density solutions.

3. The lower number of turns and the narrower airgap is also a characteristic of the high efficiency solutions.

4. Generally, higher power density solutions have thicker and smoother air-barriers. Conversely, high efficiency solutions have thinner and thuggish air-barriers;

5. Generally, high power density solutions are the lightest machine designs.

Also in this case, the MEC performance simulation resulted satisfactorily accurate when compared to the FEA results, as depicted in Figs. 4.18 and 4.19.

Table 4.11 Design decision variables setup of the air-barrier SynRM case study.

Property	Min. Value	Max. Value	Unit
Current	20	50	A
Turns	10	40	
Stator backiron height	10	43	mm
Stator tooth height	20	43	mm
Stator tooth width	3	11	mm
Stator slot opening width	1	7	mm
Airgap length	0.4	2	mm
Rotor design height	25	55	mm
Rotor back-iron height	3	15	mm
Design line start position	0	100	%
Design line length	0	100	%
Design line slope	0	80	degrees

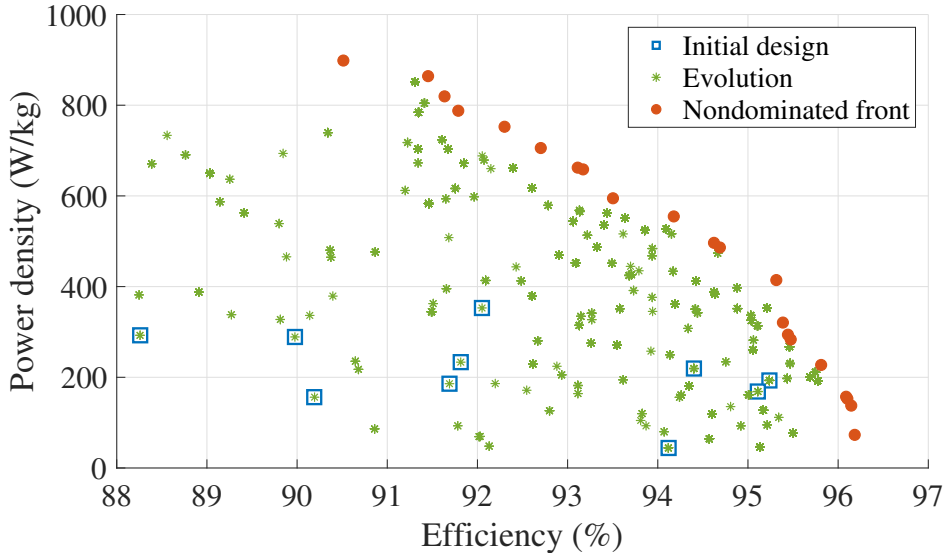

Figure 4.16 Optimization evolution and resulting nondominated front of a SynRM with air-barrier rotor packed in a cylinder with 160 mm of radius and 100 mm of length.

Table 4.12 Design decision variables of the most efficient and power-dense designs of the air-barrier SynRM case study.

Property	Most efficient design	Most power-dense design	Unit
Current	21.88	45.92	A
Turns	22	37	
Stator backiron height	34.13	36.63	mm
Stator tooth height	35.64	32.45	mm
Stator tooth width	6.84	10.28	mm
Stator slot opening width	3.28	2.82	mm
Airgap length	0.61	0.93	mm
Rotor design height	52.30	47.78	mm
Rotor back-iron height	13.87	10.57	mm

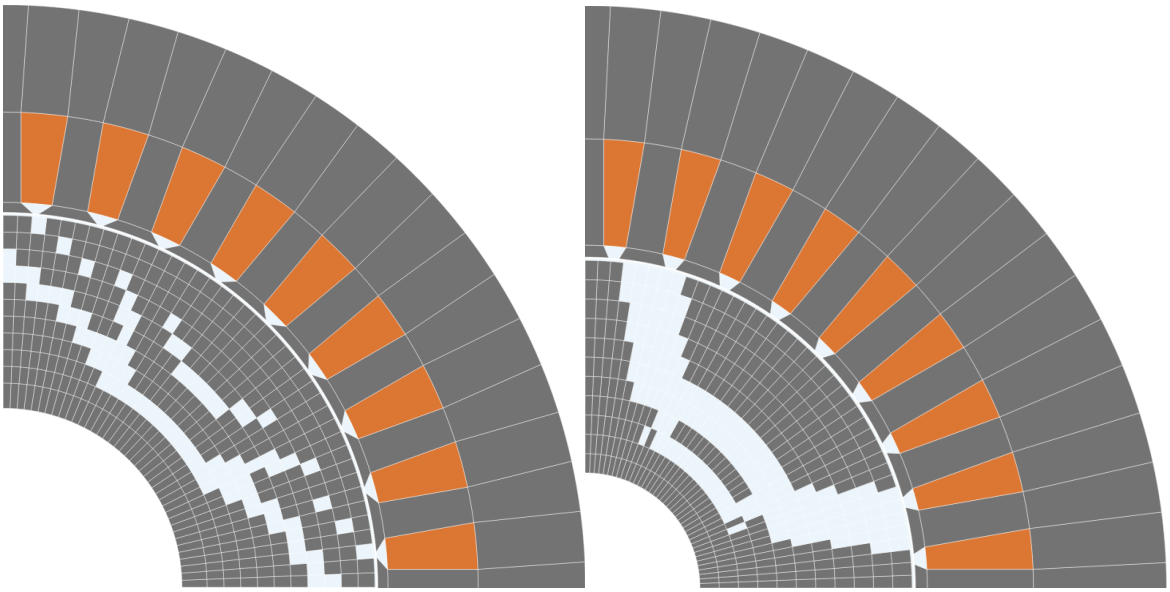

(a) (b)

Figure 4.17 MEC meshing of the solutions of the SynRM optimization displayed in Fig. 4.16: (a) nondominated solution with maximum efficiency; (b) nondominated solution with maximum power density.

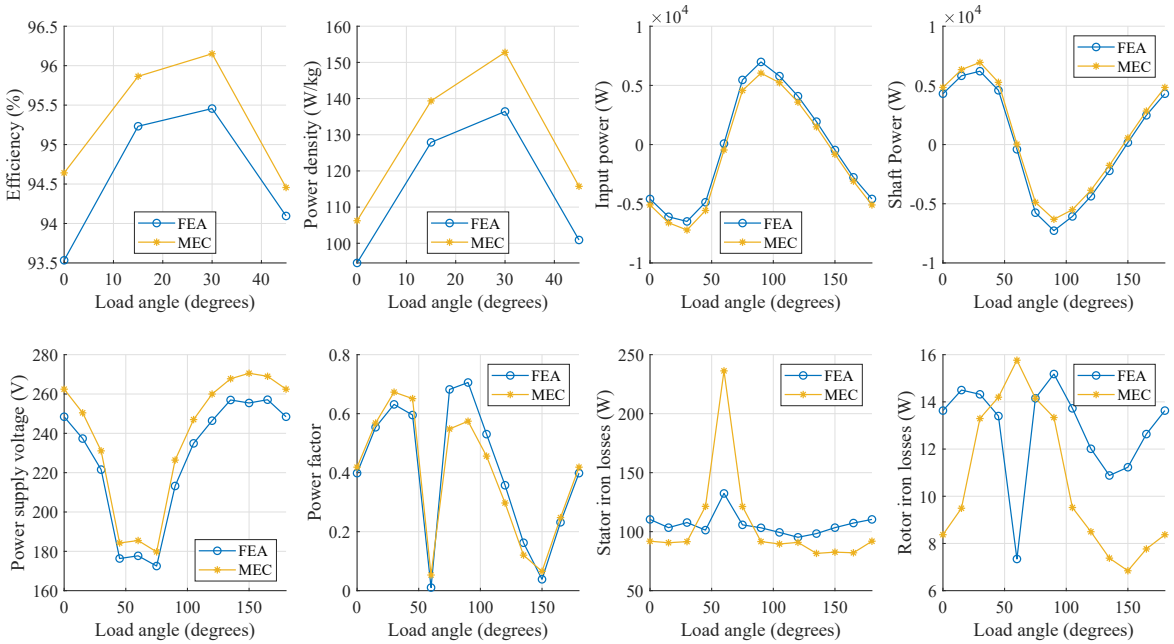

Figure 4.18 Verification of the SynRM performance curves of the nondominated solution with maximum efficiency of Fig. 4.16.

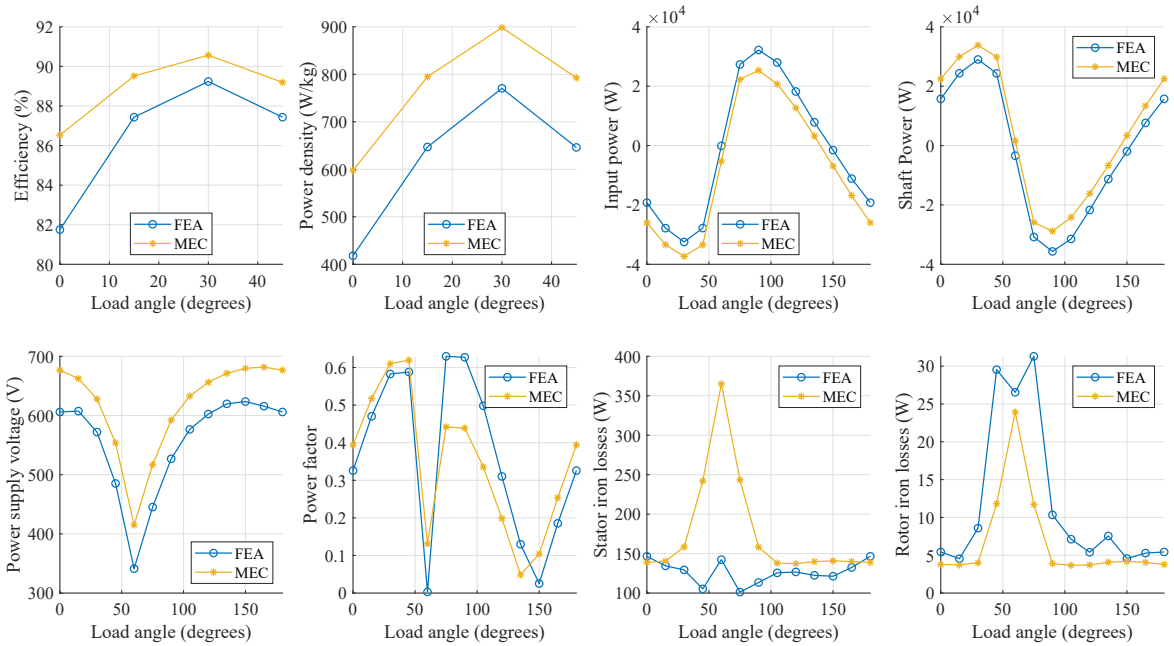

Figure 4.19 Verification of the SynRM performance curves of the nondominated solution with maximum power density of Fig. 4.16.

PMSM synchronous reluctance machine topological optimization

The parameterization of the design decision variables for the topological optimization of the PMSM was defined as described in Table 4.13. The optimization strategy adopted in this case study is the same illustrated in Fig. 4.1d. In this case, a ferrite permanent magnet and a neodymium permanent magnet design is optimized for power density improvement assessment.

The optimization was completed within 8 hours and 57 minutes and 9 hours and 12 minutes for the ferrite and neodymium designs, respectively. The evolution of the neodymium optimization and the resulting nondominated fronts of the ferrite and neodymium design optimizations are displayed in Fig. 4.20. The design decision variables of the most efficient and the most power-dense nondominated solutions of the neodymium design nondominated front are provided in Table 4.14. A comparison of the geometries of the high efficiency and high power density selected solutions is displayed in Fig. 4.21. The MEC and FEA performance analyses of the high efficiency and high power density neodymium selected solutions are compared in Fig. 4.22 and Fig. 4.23, respectively.

A diversified set of solutions was obtained by the proposed optimization methodology. In this case, a higher density of candidates populating the nearby region of the resulting neodymium nondominated front was achieved when compared to the SynRM with air-barriers optimization. The solutions clustering each end of the nondominated front have the following features:

1. High efficiency solutions have narrower and taller stator teeth, so the slot cross section area is increased to allow for the reduction of the stator winding Joule losses or to compensate solutions with higher ampere.turn value.

2. Generally, the back-iron height is larger in the cluster of the high power density solutions.

3. The lower number of turns and the narrower airgap is also a characteristic of the high efficiency solutions.

4. Generally, higher power density solutions have thicker and smoother air-barriers. Conversely, high efficiency solutions have thinner and thuggish air-barriers.

5. Generally, high power density solutions have the lightest machine designs.

Also in this case, the MEC performance simulation resulted satisfactorily accurate when compared to the FEA results, as depicted in Figs. 4.18 and 4.19.

Table 4.13 Design decision variables setup of the PMSM case study.

Property	Min. Value	Max. Value	Unit
Current	20	50	A
Turns	10	40	
Stator backiron height	10	43	mm
Stator tooth height	20	43	mm
Stator tooth width	3	11	mm
Stator slot opening width	1	7	mm
Airgap length	0.4	2	mm
Rotor design height	25	55	mm
Rotor back-iron height	3	15	mm
Design line start position	0	100	%
Design line length	0	100	%
Design line slope	0	80	degrees
Permanent magnet region	from the third to last active design layer		

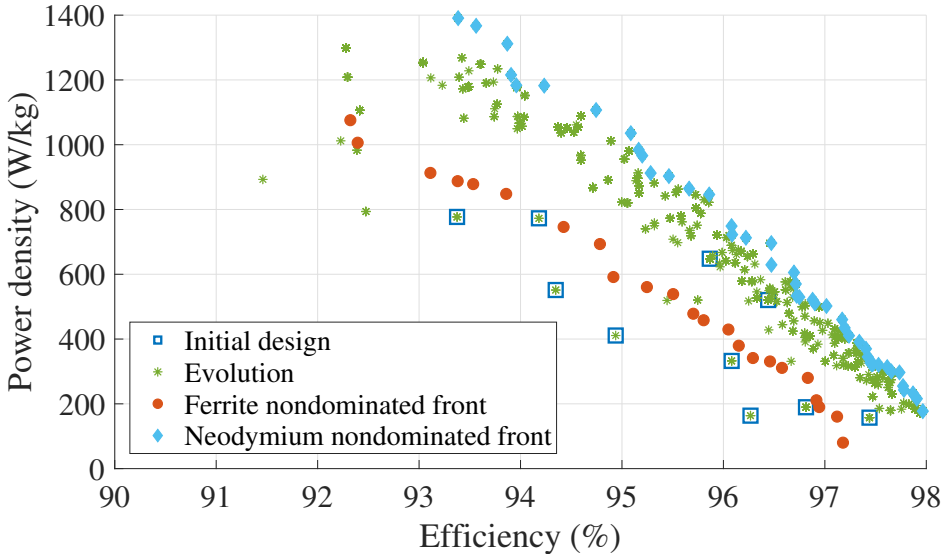

Figure 4.20 Optimization evolution and resulting nondominated front of a PMSM packed in a cylinder with 160 mm of radius and 100 mm of length.

Table 4.14 Design decision variables of the most efficient and power-dense designs of the PMSM case study.

Property	Most efficient design	Most power-dense design	Unit
Current	35.00	49.87	A
Turns	11	40	
Stator backiron height	24.68	37.30	mm
Stator tooth height	42.76	29.80	mm
Stator tooth width	7.46	7.98	mm
Stator slot opening width	1.34	4.15	mm
Airgap length	1.24	1.16	mm
Rotor design height	42.19	35.97	mm
Rotor back-iron height	13.34	12.31	mm

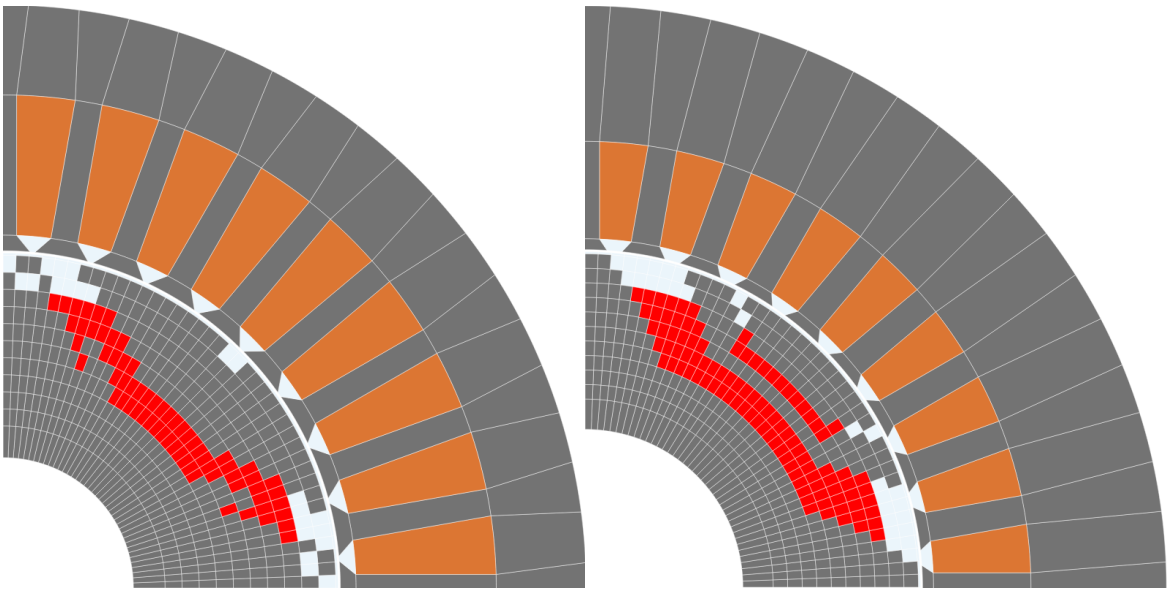

(a) (b)

Figure 4.21 MEC meshing of the solutions of the PMSM optimization displayed in Fig. 4.20: (a) nondominated solution with maximum efficiency; (b) nondominated solution with maximum power density.

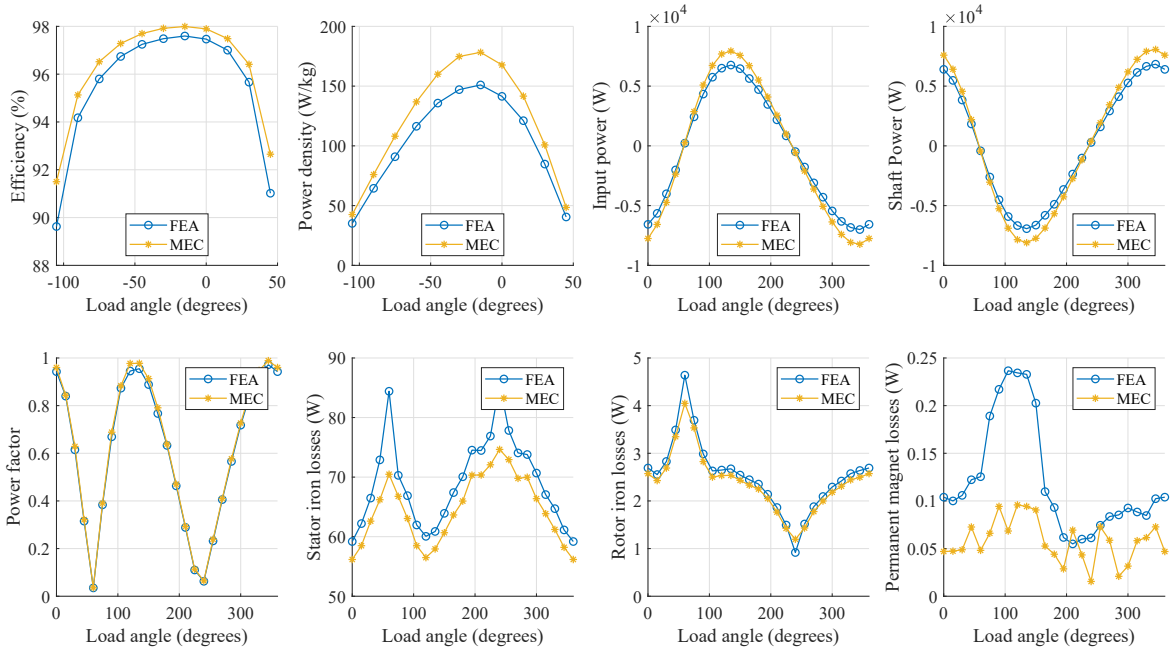

Figure 4.22 Verification of the PMSM performance curves of the nondominated solution with maximum efficiency of Fig. 4.20.

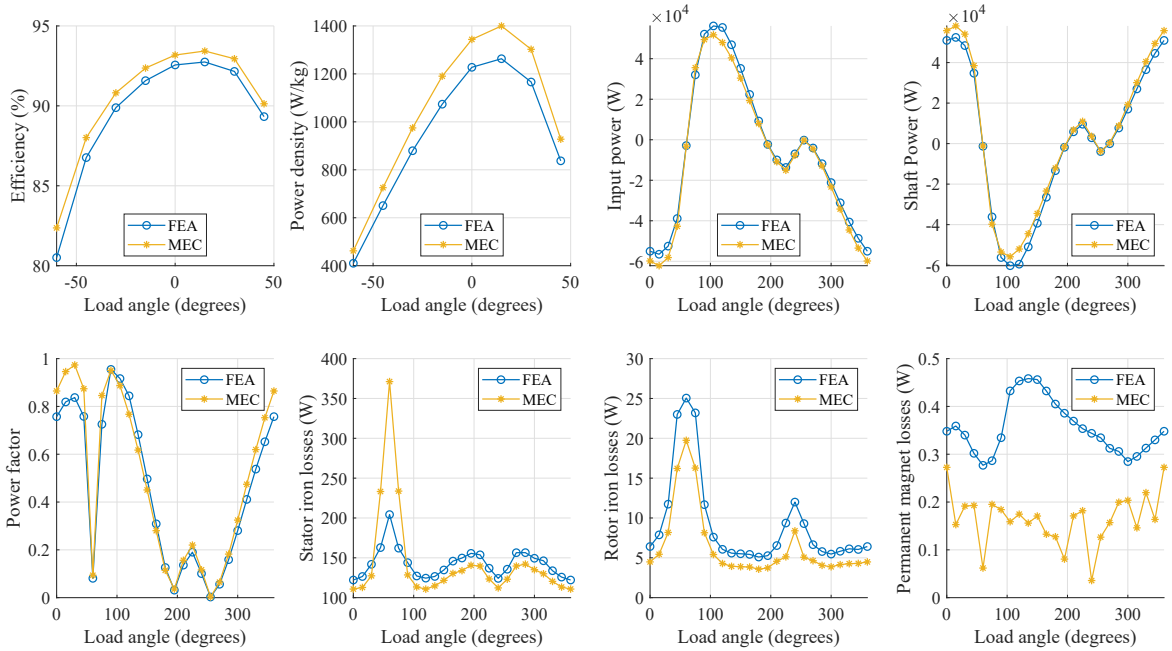

Figure 4.23 Verification of the PMSM performance curves of the nondominated solution with maximum power density of Fig. 4.20.

Comparison of the different machine optimization results

A comparison of the nondominated fronts obtained in this section is displayed in Fig. 4.24.

As expected, the most efficient solutions found for the SCIM and SynRM optimization cases have the same maximum efficiency potential, reaching values slightly above the 96 %, which is only surpassed by the ferrite and neodymium PMSM technologies. Regarding the power density potential, the PMSM technology dominates all the other technologies evaluated, reaching power densities near the 1.4 kW/kg for the low speed of 1500 rpm. In this case, the SCIM obtained designs show lower power density potential when compared to SynRM technologies. This can be justified by the following reasons:

1. The fitness assessing of the candidates puts increased pressure on the efficiency improvements, rather than power density improvement as the other SynRM and PMSM optimization scenarios.

2. The operating points of the SCIM nondominated solutions obtained correspond to the slip values which maximize efficiency, therefore, for most of these solutions there is still potential to further increased the power density by operating them at slightly higher slips, while the SynRM and PMSM solutions displayed correspond to their near maximum power density potential.

3. In addition to the restrained current density in the stator winding conductors, also the supply voltage is limited in the SCIM optimization scenario, which is an additional power constraint that is not limited in the SynRM and PMSM optimization scenarios.

Previously in this section, some coherent geometrical patterns defining the high efficiency and high power density clusters have been identified for each optimization case. The following list summarizes the most relevant electrical and geometrical characteristics perceived by the optimizer throughout the optimization cases assessed:

- High efficiency designs have enhanced slot cross sectional area for reduced winding Joule losses.

- High power density designs have enhanced back-iron and tooth thickness for improved accommodation of the higher ampere-turn per volume value.

- Also in high power density designs, the airgap and slot opening widths tend to be higher. One justification for this pattern could be the necessity to reduce the zig-zag and slot leakage fluxes, thus increasing the active versus the total magnetic flux ratio of the high power density design.

- In the SCIM designs, the shape characteristics for the high efficiency and high power density designs are not evident. A possible reason is that only the bar cross-sectional area influences the motor developed torque. Such characteristic is preferred smaller in the high power density designs.
- In the salient-pole SynRM designs, the pole surface spans practically the same number of stator teeth and the depth of the saliency is also similar for the high efficiency and high power density designs. However, in high power density designs, generally the variation of the pole saliency depth takes place in the elements rather close to the pole surface.
- In the air-barrier SynRM and PMSM designs, higher power density solutions have thicker and smoother air-barriers. Conversely, high efficiency solutions have thinner and more thuggish air-barriers.

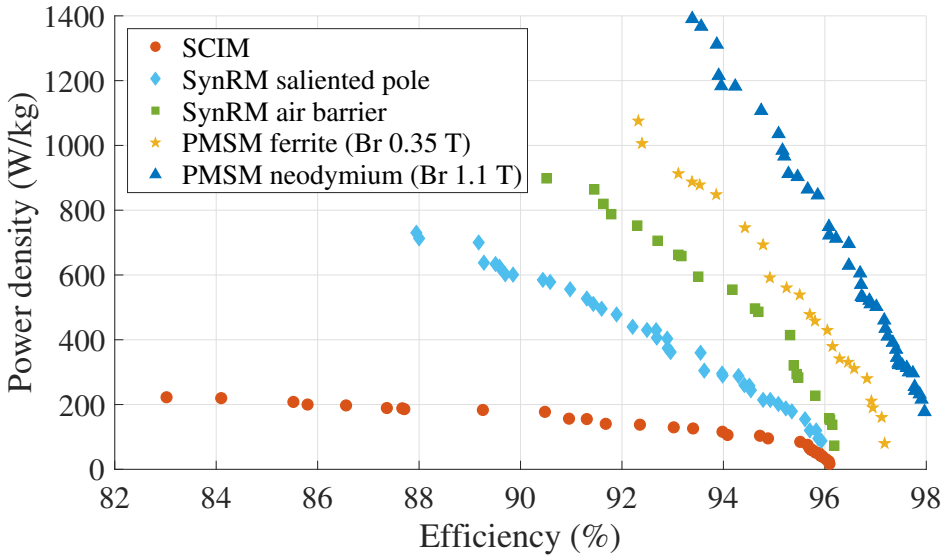

Figure 4.24 Comparison of the resulting nondominated fronts of the different motor technologies optimized for the same external package.

4.4 Conclusions

In this chapter, a review of the major contributions in literature was conducted for a comprehensive recognition of modern trends in electric machine topological optimization. The aim of this study was to analyze the main strategies proposed to deal with such high number of

decision variables and complex optimization problem. It has been concluded that: (i) the most complete analyses in terms of higher number of design decision variables and more general machine performance assessment metrics, such as efficiency and output power, are carried out in parametric topological optimization strategies; (ii) non-parametric optimization strategies are only employed in the optimization of a specific part of the machine and the performance assessment metrics used are much more specialized, such as iron losses or torque ripple.

From this perspective, and considering that an initial machine design requires the simultaneous analysis of a very large number of design decision variables for general performance optimization objectives, three novel topological optimization strategies have been proposed in this chapter for the design of the SCIM, SynRM and PMSM technologies. Hence, the proposed non-parametric design approach combined with a multiobjective optimization approach tries to exhaustively investigate, in the most complete and comprehensive manner, the best initial designs possible for a given application. The case studies provided in this chapter aim to validate the applicability of the proposed methodologies and the following conclusions can be drawn:

- The proposed methodologies allow for an exhaustive investigation of SCIM, SynRM and PMSM designs which meet a desired set of objectives and constraints.
- The main contributions of the novel methodologies proposed are: (i) the state-of-the-art vast number of design decision variables, which allow for a complete sensitivity analysis of whole machine components; (ii) the unbiased design strategy adopted by the non parametric approaches, which enhances the search space to promote state-of-the-art design diversity; (iii) the MEC solver integration allows for ultra-fast fitness assessment of the candidates with fair accuracy when compared to FEA, which is a relevant characteristic in pre-design of electric machines.
- The coarse mesh employed in this chapter case studies was sufficient to validate the methodologies proposed. However, in a real-world situation, the mesh must be refined to not only obtain more accurate performance data, but also to take full advantage of the design diversification capabilities of the proposed methodologies.

The following further developments can be outlined:

- In the SCIM optimization cases, mesh enhancement can be achieved by employing additional tangential elements in both the stator and rotor tooth regions, thus promoting improved accuracy of the performance quantities assessed.

- Likewise, in the SynRM and PMSM optimization cases, mesh enhancement can be achieved by additional tangential elements in the stator tooth region.
- In all optimization cases, a bridge layer (ferromagnetic elements only) can be added to airgap surface of the rotor, where its height is controlled by the optimizer. This allows for a better definition of buried rotor bars in SCIM designs and promotes structural feasibility of the SynRM and PMSM air-barrier designs.
- Improved solving speed can be achieved by multicore parallellization; in the proposed methodology speedups can be attained up to a maximum of one candidate per the number of cores available.
- Alternatively, computation time reduction by multi-thread solving of the linear system of equations could be investigated and compared to single-thread, but multi-candidate simultaneous solving, to select the most advantageous option.
- In the most time consuming optimization scenario, the time-step complete electromagnetic analysis of more than 2000 candidates was achieved in less than 9 hours by a standard personal computer. Therefore, more complex optimization approaches, including finer meshing for higher design resolution and the simulation of a higher number of operating points for variable speed machine applications, can be easily developed by high performance workstation, thus increasing the applicability range of the methodologies proposed.

Chapter 5

Conclusions

In this thesis, novel methodologies for the performance optimization of electric rotating machines were investigated for the application at two different stages. The first research line was dedicated to the development of stator winding optimization strategies for efficiency improvement of machines currently operating or requiring repair/rewinding actions. The second research line was dedicated to the development of strategies for the topological optimization of the machine at its design stage.

In Chapter 2, a general multiphase, multilayer winding design optimization strategy was conceived for the mitigation of the magnetomotive force spatial harmonic content and the reduction of the end-winding resistance and the amount of active material. This design strategy generates solutions through a vast cutting-edge collection of winding topologies by combining simultaneously concentrated and distributed configurations in a general multilayer topology. Further generalization was enabled by the phase-shifting concept, which promotes new opportunities for efficiency improvement and winding material savings in any multiphase winding system. The optimization was conducted by using a custom multiobjective differential evolution algorithm, which featured best convergence performance when compared to other metaheuristics as shown in Appendix A. This strategy can be applied in the electric rotating machine repairing/rewinding services opportunities, as it only requires motor data easily obtained by motor users and repair shops. It has been experimentally demonstrated that the proposed strategy may allow technicians to achieve, within few minutes, new winding designs capable to improve machine efficiency and reduce winding material. Moreover, when used to readapt the magnetizing flux of induction motors, as proposed in [16], this strategy enhances the flux matching by enabling a finer discreterization of flux levels.

In Chapter 3, a non-parametric MEC was developed for a simpler electromagnetic modeling of any radial-flux rotating machine design. For this purpose, three main contributions were proposed. The first contribution was the introduction of a novel trapezoidal sector

shaped reluctance element, which allows for a better fitting of the curvatures of radial-flux machines, especially the back-iron and tooth tip regions. This shape becomes even more accurate when considering coarser meshes, where simpler models, such as regular trapezoidal, significantly fail to model machine curvatures. The second contribution was the formulation of a novel airgap function which can emulate the permeance exponential decay as a function of misalignment between two elements at opposite sides of the airgap periphery, thus improving accuracy. The third main contribution was the redefinition of the rotor bar circuits for a more accurate calculation of the non-uniform electric current distribution occurring in the rotor solid bars for high slip values. This was achieved by allowing for multiple electric current parallel paths, instead of only one path as proposed in many other literature works. In each parallel path, the electric current is calculated independently on the basis of its magnetic flux linkage. Hence, the proposed method approximates the magnetic shielding effect caused by eddy currents occurring within the rotor bars, which is an electromagnetic effect that is not captured by other MEC approaches. The method proposed was thoroughly validated with 2-D time-harmonic and time-step FEA, comparing the results for a state-of-the-art vast and comprehensive performance analysis of three different electric machine technologies, namely the SCIM, PMSM, and SynRM. The proposed MEC resulted in a very good compromise between accuracy and computational speed, which is the fundamental characteristic of a solver for design optimization strategies. Moreover, the proposed MEC could also be applied in real-time analysis applications, due to the cutting-edge computation time achieved.

In Chapter 4, topological optimization strategies were investigated and implemented for a general design of squirrel-cage induction, synchronous salient-pole reluctance, synchronous air-barrier/slit reluctance, and synchronous permanent magnet rotor configurations. In all these topological optimization strategies developed, cutting-edge set of design decision variables was included for improved design comprehensiveness, namely the winding number of turns, power supply rated current/voltage value, stator and rotor volume ratio, stator tooth geometry, and airgap length, as well as non-parametric topological characteristics of the rotor for three different machine technologies. Performance optimization was carried out by a customized differential evolution algorithm for the maximization of efficiency and power density ($\mathrm{W/kg}$). A model constraint was utilized to make the resulting designs thermally feasible by limiting the winding current density to a maximum admissible value. The performance of the optimal designs selected was compared and validated with 2-D FEA. The simulation results showed that these strategies are capable to improve the industrial electric motor designs and are powerful tools for the initial design conceptual analyses, by providing automatic evaluation of a very wide topological variety for radial-flux SCIMs, SynRMs, and PMSMs.

Many relevant works can derive from these general methodologies. The most straightforward are the following:

- The MEC framework developed in chapter 3 can be adapted to a thermal lumped parameter equivalent circuit to enable more complex optimization methodologies where temperature is a critical constraint to be assessed.

- Likewise, a 3-D MEC can be derived from the proposed 2-D MEC framework to enable systematic topological optimization of axial-flux machines, which is currently impractical with 3-D FEA methods due to the excessive computational time and resources required. Such adaptation would require an additional flux dimension and the readaptation of the magnetomotive and electromotive force equations, as well as the airgap permeance function.

- Given the relatively fast convergence observed for the general topological optimization strategies proposed in Chapter 4, more complex optimization schemes can be devised for applications demanding more challenging designs. Strategic modifications can include an additional set of constraints to ensure, for instance, (i) that a certain torque/power profile for a specific speed range is met, (ii) no demagnetization occurs by analyzing the magnetic flux density within the magnets, and (iii) no excessive AC losses could negatively compromise the accuracy of the electric power characteristics predicted by the MEC. This can be achieved by setting a maximum threshold for eddy current Joule losses occurring in solid conductor elements of the model, namely permanent magnets, hairpin winding, and rotor bars.

- Machines with multiphase winding configurations feature excellent fault-tolerant capability and improve efficiency. By splitting the electric power by each additional phase, it drastically reduces the Joule losses in semiconductors of the VSD, leading to a higher efficiency of the power drive system. Under adverse operating conditions, a more suitable multiphase winding configuration capable to maintain power delivery can be investigated. An optimization scheme to investigate multiple arrangements of the winding connections for minimal performance loss in a specific and likely fault operating condition can be developed.

Bibliography

[1] O. Jefimenko, "Franklin's electric motors," *American Journal of Physics*, vol. 39, no. 10, pp. 1139–1140, 1971. [Online]. Available: https://doi.org/10.1119/1.1976588

[2] M. Guarnieri, "Electricity in the age of enlightenment [historical]," *IEEE Industrial Electronics Magazine*, vol. 8, no. 3, pp. 60–63, 2014.

[3] ——, "Revolving and evolving-early dc machines [historical]," *IEEE Industrial Electronics Magazine*, vol. 12, no. 3, pp. 38–43, 2018.

[4] Blundel, Stephen J., *Magnetism A Very Short Introduction*. Oxford University Press, 2012.

[5] M. Guarnieri, "The development of ac rotary machines [historical]," *IEEE Industrial Electronics Magazine*, vol. 12, no. 4, pp. 28–32, 2018.

[6] P. Alger and R. Arnold, "The history of induction motors in america," *Proceedings of the IEEE*, vol. 64, no. 9, pp. 1380–1383, 1976.

[7] A. T. de Almeida, F. J. T. E. Ferreira, and G. Baoming, "Beyond induction motors—technology trends to move up efficiency," *IEEE Transactions on Industry Applications*, vol. 50, no. 3, pp. 2103–2114, 2014.

[8] M. Yilmaz, "Limitations/capabilities of electric machine technologies and modeling approaches for electric motor design and analysis in plug-in electric vehicle applications," *Renewable and Sustainable Energy Reviews*, vol. 52, pp. 80–99, 2015. [Online]. Available: https://www.sciencedirect.com/science/article/pii/S1364032115006802

[9] C. Parag Jose and S. Meikandasivam, "A review on the trends and developments in hybrid electric vehicles," in *Innovative Design and Development Practices in Aerospace and Automotive Engineering*, R. P. Bajpai and U. Chandrasekhar, Eds. Singapore: Springer Singapore, 2017, pp. 211–229.

[10] P. Guedes-Pinto. (2022) This axial-flux motor with a pcb stator is ripe for an electrified world - it saves weight, energy, and space. [Online]. Available: https://spectrum.ieee.org/axial-flux

[11] H. Ritchie, M. Roser, and P. Rosado, "Co2 and greenhouse gas emissions," *Our World in Data*, 2020, https://ourworldindata.org/co2-and-other-greenhouse-gas-emissions.

[12] IEA. (2021) Solar pv tracking report — november 2021. [Online]. Available: https://www.iea.org/reports/solar-pv

[13] M. Khanna, "Digital transformation of the agricultural sector: Pathways, drivers and policy implications," *Applied Economic Perspectives and Policy*, vol. 43, no. 4, pp. 1221–1242, 2021. [Online]. Available: https://onlinelibrary.wiley.com/doi/abs/10.1002/aepp.13103

[14] E. Scolaro, M. Beligoj, M. P. Estevez, L. Alberti, M. Renzi, and M. Mattetti, "Electrification of agricultural machinery: A review," *IEEE Access*, vol. 9, pp. 164 520–164 541, 2021.

[15] I. E. Agency, *Key World Energy Statistics 2010*, 2010. [Online]. Available: https://www.oecd-ilibrary.org/content/publication/9789264095243-en

[16] F. Ferreira and A. de Almeida, "Induction motor downsizing as a low-cost strategy to save energy," *Journal of Cleaner Production*, vol. 24, p. 117–131, 03 2012.

[17] ——, "Method for in-field evaluation of the stator winding connection of three-phase induction motors to maximize efficiency and power factor," *IEEE Transactions on Energy Conversion*, vol. 21, no. 2, pp. 370–379, 2006.

[18] J. A. Sanguesa, V. Torres-Sanz, P. Garrido, F. J. Martinez, and J. M. Marquez-Barja, "A review on electric vehicles: Technologies and challenges," *Smart Cities*, vol. 4, no. 1, pp. 372–404, 2021. [Online]. Available: https://www.mdpi.com/2624-6511/4/1/22

[19] Canalys. (2021) Global electric vehicle sales up 109% in 2021, with half in mainland china. [Online]. Available: https://www.canalys.com/newsroom/global-electric-vehicle-market-2021

[20] S. Enyedi, "Electric cars — challenges and trends," in *2018 IEEE International Conference on Automation, Quality and Testing, Robotics (AQTR)*, 2018, pp. 1–8.

[21] G. Hill, O. Heidrich, F. Creutzig, and P. Blythe, "The role of electric vehicles in near-term mitigation pathways and achieving the uk's carbon budget," *Applied Energy*, vol. 251, p. 113111, 2019. [Online]. Available: https://www.sciencedirect.com/science/article/pii/S0306261919307834

[22] Z. Cao, A. Mahmoudi, S. Kahourzade, and W. L. Soong, "An overview of electric motors for electric vehicles," in *2021 31st Australasian Universities Power Engineering Conference (AUPEC)*, 2021, pp. 1–6.

[23] S. Sahoo, X. Zhao, and K. Kyprianidis, "A review of concepts, benefits, and challenges for future electrical propulsion-based aircraft," *Aerospace*, vol. 7, no. 4, 2020. [Online]. Available: https://www.mdpi.com/2226-4310/7/4/44

[24] R. Kolano, K. Krykowski, A. Kolano-Burian, M. Polak, J. Szynowski, and P. Zackiewicz, "Amorphous soft magnetic materials for the stator of a novel high-speed pmbldc motor," *IEEE Transactions on Magnetics*, vol. 49, no. 4, pp. 1367–1371, 2013.

[25] R. McCallum, L. Lewis, R. Skomski, M. Kramer, and I. Anderson, "Practical aspects of modern and future permanent magnets," *Annual Review of Materials Research*, vol. 44, no. 1, pp. 451–477, 2014. [Online]. Available: https://doi.org/10.1146/annurev-matsci-070813-113457

[26] SciMO - Science for motion. (2022) Revolutionary winding technology. [Online]. Available: https://sci-mo.de/en/motors/

[27] K. Rajashekara, "Present status and future trends in electric vehicle propulsion technologies," *IEEE Journal of Emerging and Selected Topics in Power Electronics*, vol. 1, no. 1, pp. 3–10, 2013.

[28] Equipmake. (2022) Equipmake joins forces with hieta to create world's most power dense electric motor. [Online]. Available: https://equipmake.co.uk/equipmake-joins-forces-with-hieta-to-create-worlds-most-power-dense-electric-motor/

[29] I. Boldea and S. A. Nasar, *The Induction Machines Design Handbook*, C. Press, Ed. Taylor & Francis Group, 2010.

[30] G. Madescu, I. Boldea, and T. Miller, "An analytical iterative model (aim) for induction motor design," in *IAS '96. Conference Record of the 1996 IEEE Industry Applications Conference Thirty-First IAS Annual Meeting*, vol. 1, 1996, pp. 566–573 vol.1.

[31] I. Boldea and L. Tutelea, *Electric Machines: Steady State, Transients, and Design with MATLAB (1st ed.)*. CRC Press, 2009.

[32] T. Jokinen, V. Hrabovcova, and J. Pyrhonen, *Design of Rotating Electrical Machines*. Wiley, 2013. [Online]. Available: https://books.google.pt/books?id=4SUIAQAAQBAJ

[33] K. Davey, "Predicting induction motor circuit parameters," *IEEE Transactions on Magnetics*, vol. 38, no. 4, pp. 1774–1779, 2002.

[34] S. Sudhoff, D. Aliprantis, B. Kuhn, and P. Chapman, "Experimental characterization procedure for use with an advanced induction machine model," *IEEE Transactions on Energy Conversion*, vol. 18, no. 1, pp. 48–56, 2003.

[35] L. J. Wu, Z. Q. Zhu, D. Staton, M. Popescu, and D. Hawkins, "An improved subdomain model for predicting magnetic field of surface-mounted permanent magnet machines accounting for tooth-tips," *IEEE Transactions on Magnetics*, vol. 47, no. 6, pp. 1693–1704, 2011.

[36] T. Lubin, S. Mezani, and A. Rezzoug, "Two-dimensional analytical calculation of magnetic field and electromagnetic torque for surface-inset permanent-magnet motors," *IEEE Transactions on Magnetics*, vol. 48, no. 6, pp. 2080–2091, 2012.

[37] N. Bianchi, *Electrical Machine Analysis Using Finite Elements*, ser. Power Electronics and Applications Series. CRC Press, 2017. [Online]. Available: https://books.google.pt/books?id=n5fMBQAAQBAJ

[38] S. J. Salon, *Finite Element Analysis of Electrical Machines*. Springer, New York, NY, 1995.

[39] E. Lwithwaite, "Magnetic equivalent circuits for electrical machines," *Proceedings of the Institution of Electrical Engineers*, vol. 114, pp. 1805–1809(4), November 1967. [Online]. Available: https://digital-library.theiet.org/content/journals/10.1049/piee.1967.0344

[40] V. Ostovic, *Dynamics of Saturated Electric Machines*. Springer-Verlag New York, 1989.

[41] J. Perho, "Reluctance network for analysing induction machines," Ph.D. dissertation, Helsinki University of Technology, 2002.

[42] M. L. Bash, J. M. Williams, and S. D. Pekarek, "Incorporating motion in mesh-based magnetic equivalent circuits," *IEEE Transactions on Energy Conversion*, vol. 25, no. 2, pp. 329–338, 2010.

[43] V. Ostovic, "A novel method for evaluation of transient states in saturated electric machines," *IEEE Transactions on Industry Applications*, vol. 25, no. 1, pp. 96–100, 1989.

[44] W. Gutjahr, "Recent trends in metaheuristics for stochastic combinatorial optimization," *Open Computer Science*, vol. 1, pp. 58–66, Mar. 2011.

[45] El-Ghazali Talbi, *Metaheuristics: From Design to Implementation*. Wiley Publishing, 2009.

[46] J. Vesterstrom and R. Thomsen, "A comparative study of differential evolution, particle swarm optimization, and evolutionary algorithms on numerical benchmark problems," in *Proceedings of the 2004 Congress on Evolutionary Computation (IEEE Cat. No.04TH8753)*, vol. 2, June 2004, pp. 1980–1987 Vol.2.

[47] S. Bandyopadhyay, S. Saha, U. Maulik, and K. Deb, "A simulated annealing-based multiobjective optimization algorithm: Amosa," *IEEE Transactions on Evolutionary Computation*, vol. 12, no. 3, pp. 269–283, 2008.

[48] K. Deb, A. Pratap, S. Agarwal, and T. Meyarivan, "A fast and elitist multiobjective genetic algorithm: NSGA-II," *IEEE Transactions on Evolutionary Computation*, vol. 6, no. 2, pp. 182–197, April 2002.

[49] J. D. Knowles and D. W. Corne, "Approximating the nondominated front using the pareto archived evolution strategy," *Evolutionary Computation*, vol. 8, no. 2, pp. 149–172, June 2000.

[50] A. M. EL-Refaie, "Fractional-slot concentrated-windings synchronous permanent magnet machines: Opportunities and challenges," *IEEE Transactions on Industrial Electronics*, vol. 57, no. 1, pp. 107–121, Jan 2010.

[51] A. O. D. Tommaso, F. Genduso, and R. Miceli, "A new software tool for design, optimization, and complete analysis of rotating electrical machines windings," *IEEE Transactions on Magnetics*, vol. 51, no. 4, pp. 1–10, April 2015.

[52] A. Tessarolo, "A survey of state-of-the-art methods to compute rotor eddy-current losses in synchronous permanent magnet machines," in *2017 IEEE Workshop on Electrical Machines Design, Control and Diagnosis (WEMDCD)*, April 2017, pp. 12–19.

[53] A. Cavagnino, S. Vaschetto, L. Ferraris, Z. Gmyrek, E. B. Agamloh, and G. Bramerdorfer, "Striving for the highest efficiency class with minimal impact for induction motor manufacturers," *IEEE Transactions on Industry Applications*, vol. 56, no. 1, pp. 194–204, Jan 2020.

[54] L. Alberti and N. Bianchi, "Theory and design of fractional-slot multilayer windings," *IEEE Transactions on Industry Applications*, vol. 49, no. 2, pp. 841–849, March 2013.

[55] V. Kindl, K. Hruska, R. Pechanek, J. Sobra, and B. Skala, "The effect of space harmonic components in the air gap magnetic flux density on torque characteristic of a squirrel-cage induction machine," in *2015 17th European Conference on Power Electronics and Applications (EPE'15 ECCE-Europe)*, Sept 2015, pp. 1–5.

[56] Y. Wang, R. Qu, and J. Li, "Multilayer windings effect on interior pm machines for ev applications," *IEEE Transactions on Industry Applications*, vol. 51, no. 3, pp. 2208–2215, May 2015.

[57] E. Levi, "Multiphase electric machines for variable-speed applications," *IEEE Transactions on Industrial Electronics*, vol. 55, no. 5, pp. 1893–1909, 2008.

[58] A. S. Abdel-Khalik, S. Ahmed, and A. M. Massoud, "Low space harmonics cancelation in double-layer fractional slot winding using dual multiphase winding," *IEEE Transactions on Magnetics*, vol. 51, no. 5, pp. 1–10, 2015.

[59] F. Barrero and M. J. Duran, "Recent advances in the design, modeling, and control of multiphase machines—part i," *IEEE Transactions on Industrial Electronics*, vol. 63, no. 1, pp. 449–458, 2016.

[60] M. J. Duran and F. Barrero, "Recent advances in the design, modeling, and control of multiphase machines—part ii," *IEEE Transactions on Industrial Electronics*, vol. 63, no. 1, pp. 459–468, 2016.

[61] W. Kong, M. Kang, D. Li, R. Qu, D. Jiang, and C. Gan, "Investigation of spatial harmonic magnetic field coupling effect on torque ripple for multiphase induction motor under open fault condition," *IEEE Transactions on Power Electronics*, vol. 33, no. 7, pp. 6060–6071, 2018.

[62] A. S. Al-Adsani and O. Beik, "Design of a multiphase hybrid permanent magnet generator for series hybrid ev," *IEEE Transactions on Energy Conversion*, vol. 33, no. 3, pp. 1499–1507, 2018.

[63] L. Cheng, Y. Sui, P. Zheng, Z. Yin, and C. Wang, "Influence of stator mmf harmonics on the utilization of reluctance torque in six-phase pma-synrm with fscw," *Energies*, vol. 11, no. 1, 2018. [Online]. Available: https://www.mdpi.com/1996-1073/11/1/108

[64] M. Slunjski, O. Dordevic, M. Jones, and E. Levi, "Symmetrical/asymmetrical winding reconfiguration in multiphase machines," *IEEE Access*, vol. 8, pp. 12 835–12 844, 2020.

[65] Y. Demir and M. Aydin, "A novel dual three-phase permanent magnet synchronous motor with asymmetric stator winding," *IEEE Transactions on Magnetics*, vol. 52, no. 7, pp. 1–5, 2016.

[66] P. F. Gonçalves, S. M. Cruz, and A. M. Mendes, "Design of a six-phase asymmetrical permanent magnet synchronous generator for wind energy applications," *The Journal of Engineering*, vol. 2019, no. 17, pp. 4532–4536, 2019.

[67] T. Zhao, S. Wu, and S. Cui, "Multiphase pmsm with asymmetric windings for more electric aircraft," *IEEE Transactions on Transportation Electrification*, vol. 6, no. 4, pp. 1592–1602, 2020.

[68] G. Dajaku and D. Gerling, "A novel 24-slots/10-poles winding topology for electric machines," in *2011 IEEE International Electric Machines Drives Conference (IEMDC)*, 2011, pp. 65–70.

[69] P. B. Reddy, K.-K. Huh, and A. M. EL-Refaie, "Generalized approach of stator shifting in interior permanent-magnet machines equipped with fractional-slot concentrated windings," *IEEE Transactions on Industrial Electronics*, vol. 61, no. 9, pp. 5035–5046, 2014.

[70] G. Dajaku, S. Spas, and D. Gerling, "Advanced optimization methods for fractional slot concentrated windings," *Electrical Engineering*, vol. 101, no. 1, pp. 103–120, Apr 2019. [Online]. Available: https://doi.org/10.1007/s00202-019-00760-6

[71] B. Zhao, J. Gong, T. Tong, Y. Xu, E. Semail, N. K. Nguyen, and F. Gillon, "A novel five-phase fractional slot concentrated winding with low space harmonic contents," *IEEE Transactions on Magnetics*, vol. 57, no. 6, pp. 1–5, 2021.

[72] V. I. Patel, J. Wang, W. Wang, and X. Chen, "Six-phase fractional-slot-per-pole-per-phase permanent-magnet machines with low space harmonics for electric vehicle application," *IEEE Transactions on Industry Applications*, vol. 50, no. 4, pp. 2554–2563, July 2014.

[73] B. Chalmers, "A.c. machine windings with reduced harmonic content," *Proceedings of the Institution of Electrical Engineers*, vol. 111, pp. 1859–1863(4), November 1964. [Online]. Available: https://digital-library.theiet.org/content/journals/10.1049/piee.1964.0304

[74] M. V. Cistelecan, F. J. Ferreira, and M. Popescu, "Three phase tooth-concentrated interspersed windings with low space harmonic content," in *The XIX International Conference on Electrical Machines - ICEM 2010*, 2010, pp. 1–6.

[75] D. Hiramatsu, K. F. Sutrisna, T. Tokumasu, H. Ishizuka, M. Okubo, K. Tsujikawa, T. Ueda, H. Hachiya, T. Aso, and T. Otaka, "Novel interspersed windings to reduce space flux harmonics caused by fractional-slot of synchronous machine," in *2013 International Electric Machines Drives Conference*, 2013, pp. 634–639.

[76] D. Hiramatsu, K. Tsujikawa, T. Ueda, M. Fujita, H. Ishizuka, M. Okubo, H. Hachiya, J. Mori, D. Nozaki, D. Iwashita, and T. Tokumasu, "Winding method to reduce vibration and loss caused by fractional slot of synchronous machine," *Electrical Engineering in Japan*, vol. 198, no. 2, pp. 39–49, 2017. [Online]. Available: https://onlinelibrary.wiley.com/doi/abs/10.1002/eej.22897

[77] D. A. Kocabas, "Novel winding and core design for maximum reduction of harmonic magnetomotive force in ac motors," *IEEE Transactions on Magnetics*, vol. 45, no. 2, pp. 735–746, Feb 2009.

[78] N. Bekka, M. E. H. Zaïm, N. Bernard, and D. Trichet, "A novel methodology for optimal design of fractional slot with concentrated windings," *IEEE Transactions on Energy Conversion*, vol. 31, no. 3, pp. 1153–1160, 2016.

[79] A. Tessarolo, "A quadratic-programming approach to the design optimization of fractional-slot concentrated windings for surface permanent-magnet machines," *IEEE Transactions on Energy Conversion*, vol. 33, no. 1, pp. 442–452, March 2018.

[80] A. Tessarolo, C. Ciriani, M. Bortolozzi, M. Mezzarobba, and N. Barbini, "Investigation into multi-layer fractional-slot concentrated windings with unconventional slot-pole combinations," *IEEE Transactions on Energy Conversion*, vol. 34, no. 4, pp. 1985–1996, 2019.

[81] A. Tessarolo, C. Ciriani, N. Elloumi, and M. Mezzarobba, "Potentials and limits of three-phase fractional-slot concentrated winding optimization," in *2021 IEEE Workshop on Electrical Machines Design, Control and Diagnosis (WEMDCD)*, 2021, pp. 143–148.

[82] M. A. Kabir and I. Husain, "New multilayer winding configuration for distributed mmf in ac machines with shorter end-turn length," in *2016 IEEE Power and Energy Society General Meeting (PESGM)*, July 2016, pp. 1–5.

[83] M. A. Kabir and I. Husain, "Application of a multilayer ac winding to design synchronous reluctance motors," *IEEE Transactions on Industry Applications*, vol. 54, no. 6, pp. 5941–5953, 2018.

[84] M. A. Kabir, M. Z. M. Jaffar, Z. Wan, and I. Husain, "Design, optimization, and experimental evaluation of multilayer ac winding for induction machine," *IEEE Transactions on Industry Applications*, vol. 55, no. 4, pp. 3630–3639, July 2019.

[85] Z. Guo, Y. Liang, X. Bian, and D. Wang, "Multiobjective optimization for arrangement of the asymmetric-paths winding based on improved discrete particle swarm approach," *IEEE Transactions on Energy Conversion*, vol. 33, no. 3, pp. 1571–1578, 2018.

[86] N. Tang and I. P. Brown, "A systematic approach for developing electric machine windings with suppressed mmf space harmonics," *Electric Power Components and Systems*, vol. 45, no. 20, pp. 2327–2338, 2017. [Online]. Available: https://doi.org/10.1080/15325008.2017.1378950

[87] N. Tang and I. P. Brown, "Framework and solution techniques for suppressing electric machine winding mmf space harmonics by varying slot distribution and coil turns," *IEEE Transactions on Magnetics*, vol. 54, no. 5, pp. 1–12, May 2018.

[88] ——, "Family phenomenon in electric machine winding mmf space harmonics: Attribution and applications," *IEEE Transactions on Magnetics*, vol. 55, no. 5, pp. 1–10, May 2019.

[89] S. Wang, Y. Guo, P. Jin, and R. Xu, "Theory and design of a novel multi-layer modular modulation winding," *IEEE Access*, vol. 9, pp. 115 442–115 452, 2021.

[90] F. Luise, A. Tessarolo, F. Agnolet, S. Pieri, M. Scalabrin, M. Di Chiara, and M. De Martin, "Design optimization and testing of high-performance motors: Evaluating a compromise between quality design development and production costs of a halbach-array pm slotless motor," *IEEE Industry Applications Magazine*, vol. 22, no. 6, pp. 19–32, 2016.

[91] G. Burnand, D. M. Araujo, and Y. Perriard, "Optimization of shape and topology for slotless windings in bldc machines," in *2018 21st International Conference on Electrical Machines and Systems (ICEMS)*, 2018, pp. 31–36.

[92] A. Boglietti, A. Cavagnino, and M. Lazzari, "Computational algorithms for induction-motor equivalent circuit parameter determination—part i: Resistances and leakage reactances," *IEEE Transactions on Industrial Electronics*, vol. 58, no. 9, pp. 3723–3733, Sept 2011.

[93] D. Ban, D. Zarko, and I. Mandic, "Turbogenerator end-winding leakage inductance calculation using a 3-D analytical approach based on the solution of Neumann Integrals," *IEEE Transactions on Energy Conversion*, vol. 20, no. 1, pp. 98–105, March 2005.

[94] M. Bortolozzi, A. Tessarolo, and C. Bruzzese, "Analytical computation of end-coil leakage inductance of round-rotor synchronous machines field winding," *IEEE Transactions on Magnetics*, vol. 52, no. 2, pp. 1–10, 2016.

[95] F. W. Grover, *Inductance Calculations*, C. Corporation, Ed. Dover Books on Electrical Engineering, 2013.

[96] K. V. Price, *Differential Evolution*. Berlin, Heidelberg: Springer Berlin Heidelberg, 2013, pp. 187–214.

[97] M. Yang, C. Li, Z. Cai, and J. Guan, "Differential evolution with auto-enhanced population diversity," *IEEE Transactions on Cybernetics*, vol. 45, no. 2, pp. 302–315, Feb 2015.

[98] Y. G. Woldesenbet, G. G. Yen, and B. G. Tessema, "Constraint handling in multiobjective evolutionary optimization," *IEEE Transactions on Evolutionary Computation*, vol. 13, no. 3, pp. 514–525, June 2009.

[99] "Rotating electrical machines - part 2-1: Standard methods for determining losses and efficiency from tests (excluding machines for traction vehicles)," International Electrotechnical Commission (IEC), Standard, Jun. 2014.

[100] A. Tessarolo, M. Mezzarobba, and N. Barbini, "Improved four-layer winding design for a 12-slot 10-pole permanent magnet machine using unequal tooth coils," in *IECON 2016 - 42nd Annual Conference of the IEEE Industrial Electronics Society*, Oct 2016, pp. 1686–1691.

[101] T. J. Juha Pyrhonen and V. Hrabovcova, *Design of Rotating Electrical Machines*. John Wiley & Sons, Ltd, 2013. [Online]. Available: https://onlinelibrary.wiley.com/doi/abs/10.1002/9781118701591

[102] T. A. Lipo, *Introduction to AC machine design*, ser. IEEE Press series on power engineering. John Wiley & Sons, Ltd, 2017. [Online]. Available: https://onlinelibrary.wiley.com/doi/abs/10.1002/9781119352181

[103] G. Watthewaduge, E. Sayed, A. Emadi, and B. Bilgin, "Electromagnetic modeling techniques for switched reluctance machines: State-of-the-art review," *IEEE Open Journal of the Industrial Electronics Society*, vol. 1, pp. 218–234, 2020.

[104] S. Sato, T. Sato, and H. Igarashi, "Topology Optimization of Synchronous Reluctance Motor Using Normalized Gaussian Network," *IEEE Transactions on Magnetics*, vol. 51, no. 3, pp. 1–4, 2015.

[105] G. Bramerdorfer, J. A. Tapia, J. J. Pyrhonen, and A. Cavagnino, "Modern electrical machine design optimization: Techniques, trends, and best practices," *IEEE Transactions on Industrial Electronics*, vol. 65, no. 10, pp. 7672–7684, 2018.

[106] M. Moallem and G. Dawson, "An improved magnetic equivalent circuit method for predicting the characteristics of highly saturated electromagnetic devices," *IEEE Transactions on Magnetics*, vol. 34, no. 5, pp. 3632–3635, 1998.

[107] M. Amrhein and P. T. Krein, "Magnetic equivalent circuit simulations of electrical machines for design purposes," in *2007 IEEE Electric Ship Technologies Symposium*, 2007, pp. 254–260.

[108] M. Amrhein, "Induction machine performance improvements – design oriented approaches," Ph.D. dissertation, University of Illinois at Urbana-Champaign, 2007.

[109] S. D. Sudhoff, B. T. Kuhn, K. A. Corzine, and B. T. Branecky, "Magnetic equivalent circuit modeling of induction motors," *IEEE Transactions on Energy Conversion*, vol. 22, no. 2, pp. 259–270, 2007.

[110] M. Amrhein and P. T. Krein, "3-d magnetic equivalent circuit framework for modeling electromechanical devices," *IEEE Transactions on Energy Conversion*, vol. 24, no. 2, pp. 397–405, 2009.

[111] S.-H. Mao, D. Dorrell, and M.-C. Tsai, "Fast analytical determination of aligned and unaligned flux linkage in switched reluctance motors based on a magnetic circuit model," *IEEE Transactions on Magnetics*, vol. 45, no. 7, pp. 2935–2942, 2009.

[112] M. L. Bash and S. Pekarek, "Analysis and validation of a population-based design of a wound-rotor synchronous machine," *IEEE Transactions on Energy Conversion*, vol. 27, no. 3, pp. 603–614, 2012.

[113] H. Gorginpour, H. Oraee, and R. A. McMahon, "A novel modeling approach for design studies of brushless doubly fed induction generator based on magnetic equivalent circuit," *IEEE Transactions on Energy Conversion*, vol. 28, no. 4, pp. 902–912, 2013.

[114] F. E. Fleming and C. S. Edrington, "Real-Time Emulation of Switched Reluctance Machines via Magnetic Equivalent Circuits," *IEEE Transactions on Industrial Electronics*, vol. 63, no. 6, pp. 3366–3376, 2016.

[115] S. S. R. Bonthu, S. Choi, and J. Baek, "Design Optimization With Multiphysics Analysis on External Rotor Permanent Magnet-Assisted Synchronous Reluctance Motors," *IEEE Transactions on Energy Conversion*, vol. 33, no. 1, pp. 290–298, 2018.

[116] S. Li, S. Zhang, T. G. Habetler, and R. G. Harley, "Modeling, Design Optimization, and Applications of Switched Reluctance Machines—A Review," *IEEE Transactions on Industry Applications*, vol. 55, no. 3, pp. 2660–2681, 2019.

[117] V. Naeini, "A detailed magnetic equivalent circuit modeling for torque ripples minimizing of a switched reluctance motor," *International Transactions on Electrical Energy Systems*, vol. 29, no. 10, p. e12067, 2019, e12067 ITEES-19-0051.R1. [Online]. Available: https://onlinelibrary.wiley.com/doi/abs/10.1002/2050-7038.12067

[118] G. Liu, S. Jiang, W. Zhao, and Q. Chen, "Modular reluctance network simulation of a linear permanent-magnet vernier machine using new mesh generation methods," *IEEE Transactions on Industrial Electronics*, vol. 64, no. 7, pp. 5323–5332, 2017.

[119] D. Cao, W. Zhao, J. Ji, L. Ding, and J. Zheng, "A generalized equivalent magnetic network modeling method for vehicular dual-permanent-magnet vernier machines," *IEEE Transactions on Energy Conversion*, vol. 34, no. 4, pp. 1950–1962, 2019.

[120] L. Ding, G. Liu, Q. Chen, and G. Xu, "A novel mesh-based equivalent magnetic network for performance analysis and optimal design of permanent magnet machines," *IEEE Transactions on Energy Conversion*, vol. 34, no. 3, pp. 1337–1346, 2019.

[121] M. Amrhein and P. T. Krein, "Induction machine modeling approach based on 3-d magnetic equivalent circuit framework," *IEEE Transactions on Energy Conversion*, vol. 25, no. 2, pp. 339–347, 2010.

[122] S. Asfirane, S. Hlioui, Y. Amara, O. De La Barriere, G. Barakat, and M. Gabsi, "Global quantities computation using mesh-based generated reluctance networks," *IEEE Transactions on Magnetics*, vol. 54, no. 11, pp. 1–4, 2018.

[123] ANSYS Maxwell. (2021) Motor-cad. [Online]. Available: https://www.ansys.com/products/electronics/ansys-motor-cad

[124] Motor Design Limited. (2021) Motor-cad. [Online]. Available: https://www.motor-design.com/motor-cad/

[125] G2Elab. (2021) Reluctool.

[126] Altair. (2021) Fluxmotor.

[127] S. Sudhoff. (2021) Magnetic equivalent circuit toolbox 3.2. [Online]. Available: https://engineering.purdue.edu/ECE/Research/Areas/PES/Software/MEC_toolbox

[128] J. Kokernak and D. Torrey, "Magnetic circuit model for the mutually coupled switched-reluctance machine," *IEEE Transactions on Magnetics*, vol. 36, no. 2, pp. 500–507, 2000.

[129] N. R. Tavana and V. Dinavahi, "Real-time nonlinear magnetic equivalent circuit model of induction machine on fpga for hardware-in-the-loop simulation," *IEEE Transactions on Energy Conversion*, vol. 31, no. 2, pp. 520–530, 2016.

[130] A. R. Tariq, C. E. Nino-Baron, and E. G. Strangas, "Iron and magnet losses and torque calculation of interior permanent magnet synchronous machines using magnetic equivalent circuit," *IEEE Transactions on Magnetics*, vol. 46, no. 12, pp. 4073–4080, 2010.

[131] J. Nazarzadeh and V. Naeini, "Magnetic reluctance method for dynamical modeling of squirrel cage induction machines," in *Electric Machines and Drives*, M. Chomat, Ed. Rijeka: IntechOpen, 2011, ch. 3. [Online]. Available: https://doi.org/10.5772/14798

[132] M. Zhu, Y. Fang, X. Huang, and X. Yin, "Dynamic reluctance mesh modeling and losses evaluation of permanent magnet traction motor," in *2016 IEEE Conference on Electromagnetic Field Computation (CEFC)*, 2016, pp. 1–1.

[133] P. Naderi, "Modified magnetic-equivalent-circuit approach for various faults studying in saturable double-cage-induction machines," *IET Electric Power Applications*, vol. 11, no. 7, pp. 1224–1234, 2017. [Online]. Available: https://ietresearch.onlinelibrary.wiley.com/doi/abs/10.1049/iet-epa.2016.0782

[134] J. Gyselinck and R. Sabariego, "Airgap reluctance identification for the magnetic equivalent circuit modelling of induction machines," in *Conference on the Computation of Electromagnetic Fields (COMPUMAG)*, 2013.

[135] Q. Yu, X. Wang, and Y. Cheng, "Magnetic modeling of saliency effect for saturated electrical machines with a new calculation method," *IEEE Transactions on Magnetics*, vol. 52, no. 6, pp. 1–6, 2016.

[136] E. Severson, R. Nilssen, T. Undeland, and N. Mohan, "Magnetic equivalent circuit modeling of the ac homopolar machine for flywheel energy storage," *IEEE Transactions on Energy Conversion*, vol. 30, no. 4, pp. 1670–1678, 2015.

[137] D. Caballero, B. Prieto, G. Artetxe, I. Elosegui, and M. Martinez-Iturralde, "Node mapping criterion for highly saturated interior pmsms using magnetic reluctance network," *Energies*, vol. 11, no. 9, 2018. [Online]. Available: https://www.mdpi.com/1996-1073/11/9/2294

[138] G. Forstner, A. Kugi, and W. Kemmetmüller, "A Magnetic Equivalent Circuit Based Modeling Framework for Electric Motors Applied to a PMSM With Winding Short Circuit," *IEEE Transactions on Power Electronics*, vol. 35, no. 11, pp. 12 285–12 295, 2020.

[139] X. Han and A. Palazzolo, "Unstable force analysis for induction motor eccentricity," *Journal of Sound and Vibration*, vol. 370, pp. 230–258, 2016. [Online]. Available: https://www.sciencedirect.com/science/article/pii/S0022460X16000948

[140] R. Deeb, "Calculation of eddy current losses in permanent magnets of servo motor," 2011.

[141] Fausto Fiorillo, *Characterization and Measurement of Magnetic Materials*. Academic Press, 2004.

[142] J. Lannoo, D. Vanoost, J. Peuteman, S. Debruyne, H. De Gersem, and D. Pissoort, "Improved air gap permeance model to characterise the transient behaviour of electrical machines using magnetic equivalent circuit method," *International Journal of Numerical Modelling: Electronic Networks, Devices and Fields*, vol. 33, no. 5, p. e2749, 2020. [Online]. Available: https://onlinelibrary.wiley.com/doi/abs/10.1002/jnm.2749

[143] X. Li, J. Demmel, J. Gilbert, iL. Grigori, M. Shao, and I. Yamazaki, "SuperLU Users' Guide," Lawrence Berkeley National Laboratory, Tech. Rep. LBNL-44289, September 1999, https://portal.nersc.gov/project/sparse/superlu/. Last update: August 2011.

[144] J. W. Demmel, S. C. Eisenstat, J. R. Gilbert, X. S. Li, and J. W. H. Liu, "A supernodal approach to sparse partial pivoting," *SIAM J. Matrix Analysis and Applications*, vol. 20, no. 3, pp. 720–755, 1999.

[145] A. M. Silva, F. J. T. E. Ferreira, M. V. Cistelecan, and C. H. Antunes, "Multiobjective design optimization of generalized multilayer multiphase ac winding," *IEEE Transactions on Energy Conversion*, vol. 34, no. 4, pp. 2158–2167, 2019.

[146] K. T. Chau, D. Zhang, J. Z. Jiang, C. Liu, and Y. Zhang, "Design of a magnetic-geared outer-rotor permanent-magnet brushless motor for electric vehicles," *IEEE Transactions on Magnetics*, vol. 43, no. 6, pp. 2504–2506, 2007.

[147] V. M. Sundaram and H. A. Toliyat, "A fractional slot concentrated winding (fscw) configuration for outer rotor squirrel cage induction motors," in *2015 IEEE International Electric Machines Drives Conference (IEMDC)*, 2015, pp. 20–26.

[148] T.-Y. Lee, M.-K. Seo, Y.-J. Kim, and S.-Y. Jung, "Motor design and characteristics comparison of outer-rotor-type bldc motor and blac motor based on numerical analysis," *IEEE Transactions on Applied Superconductivity*, vol. 26, no. 4, pp. 1–6, 2016.

[149] S. S. R. Bonthu, M. T. B. Tarek, and S. Choi, "Optimal torque ripple reduction technique for outer rotor permanent magnet synchronous reluctance motors," *IEEE Transactions on Energy Conversion*, vol. 33, no. 3, pp. 1184–1192, 2018.

[150] D.-K. Woo, I.-W. Kim, D.-K. Lim, J.-S. Ro, and H.-K. Jung, "Cogging torque optimization of axial flux permanent magnet motor," *IEEE Transactions on Magnetics*, vol. 49, no. 5, pp. 2189–2192, 2013.

[151] B. Dianati, S. Kahourzade, and A. Mahmoudi, "Optimization of axial-flux induction motors for the application of electric vehicles considering driving cycles," *IEEE Transactions on Energy Conversion*, vol. 35, no. 3, pp. 1522–1533, 2020.

[152] J. Mei, Y. Zuo, C. H. T. Lee, and J. L. Kirtley, "Modeling and optimizing method for axial flux induction motor of electric vehicles," *IEEE Transactions on Vehicular Technology*, vol. 69, no. 11, pp. 12 822–12 831, 2020.

[153] M. V. Cistelecan, M. Popescu, L. Melcescu, and T. Tudorache, "Three phase line start claw poles permanent magnet motor with pole changing winding," in *2008 International Symposium on Power Electronics, Electrical Drives, Automation and Motion*, 2008, pp. 245–249.

[154] F. Ferreira, M. Cistelecan, and A. de Almeida, "Voltage unbalance impact on the performance of line-start permanent-magnet synchronous motors," *International Conference on Energy Efficiency in Motor Driven Systems (EEMODS'09)*.

[155] Y. Guo, J. Zhu, and D. G. Dorrell, "Design and analysis of a claw pole permanent magnet motor with molded soft magnetic composite core," *IEEE Transactions on Magnetics*, vol. 45, no. 10, pp. 4582–4585, 2009.

[156] Y. Zhang, D. Li, P. Yan, X. Ren, R. Qu, and J. Ma, "A high torque density claw pole permanent-magnets vernier machine," *IEEE Journal of Emerging and Selected Topics in Power Electronics*, pp. 1–1, 2021.

[157] M.-R. Park, J.-W. Jung, D.-Y. Kim, J.-P. Hong, and M.-S. Lim, "Design of high torque density multi-core concentrated flux-type synchronous motors considering vibration characteristics," *IEEE Transactions on Industry Applications*, vol. 55, no. 2, pp. 1351–1359, 2019.

[158] R. R. Kumar, C. Chetri, P. Devi, and A. Dwivedi, "Design and analysis of dual stator dual rotor six-phase i-shaped permanent magnet synchronous motor for electric vehicles application," in *2020 IEEE International Conference on Power Electronics, Drives and Energy Systems (PEDES)*, 2020, pp. 1–6.

[159] F. E. Hunstable, "Multi-tunnel electric motor/generator," 2017, US Patent US9729016B1. [Online]. Available: https://patents.google.com/patent/US9729016

[160] A. Boglietti, A. Cavagnino, L. Ferraris, M. Lazzari, and G. Luparia, "No tooling cost process for induction motors energy efficiency improvements," *IEEE Transactions on Industry Applications*, vol. 41, no. 3, pp. 808–816, May 2005.

[161] L. Alberti, N. Bianchi, A. Boglietti, and A. Cavagnino, "Core axial lengthening as effective solution to improve the induction motor efficiency classes," *IEEE Transactions on Industry Applications*, vol. 50, no. 1, pp. 218–225, Jan 2014.

[162] Jae-Woo Kim, Byung-Taek Kim, and Byung Il Kwon, "Optimal stator slot design of inverter-fed induction motor in consideration of harmonic losses," *IEEE Transactions on Magnetics*, vol. 41, no. 5, pp. 2012–2015, May 2005.

[163] S. Ghosh, H. Memane, M. Karpe, R. Birajdar, V. K. Yadav, and V. Mukherjee, "Design of high performance induction motor through multi objective and multi domain optimization," in *2015 5th International Electric Drives Production Conference (EDPC)*, 2015, pp. 1–6.

[164] D. Zhang, C. S. Park, and C. S. Koh, "A new optimal design method of rotor slot of three-phase squirrel cage induction motor for nema class d speed-torque characteristic using multi-objective optimization algorithm," *IEEE Transactions on Magnetics*, vol. 48, no. 2, pp. 879–882, Feb 2012.

[165] H. J. Lee, S. H. Im, D. Y. Um, and G. S. Park, "A design of rotor bar for improving starting torque by analyzing rotor resistance and reactance in squirrel cage induction motor," *IEEE Transactions on Magnetics*, vol. 54, no. 3, pp. 1–4, 2018.

[166] A.-I. Constantin and V. Fireţeanu, "Hyperstudy optimization of induction motors finite element assisted design," in *2021 International Aegean Conference on Electrical Machines and Power Electronics (ACEMP) 2021 International Conference on Optimization of Electrical and Electronic Equipment (OPTIM)*, 2021, pp. 191–197.

[167] M. Di Nardo, A. Marfoli, M. Degano, and C. Gerada, "Open and closed rotor slots design of single and double cages induction motor," in *2021 IEEE Workshop on Electrical Machines Design, Control and Diagnosis (WEMDCD)*, 2021, pp. 125–130.

[168] J. Chen, Y. Fujii, M. W. Johnson, A. Farhan, and E. L. Severson, "Optimal design of the bearingless induction motor," *IEEE Transactions on Industry Applications*, vol. 57, no. 2, pp. 1375–1388, 2021.

[169] G. Lee, S. Min, and J.-P. Hong, "Optimal shape design of rotor slot in squirrel-cage induction motor considering torque characteristics," *IEEE Transactions on Magnetics*, vol. 49, no. 5, pp. 2197–2200, 2013.

[170] A. Marfoli, M. D. Nardo, M. Degano, C. Gerada, and W. Chen, "Rotor design optimization of squirrel cage induction motor - part i: Problem statement," *IEEE Transactions on Energy Conversion*, vol. 36, no. 2, pp. 1271–1279, 2021.

[171] M. D. Nardo, A. Marfoli, M. Degano, C. Gerada, and W. Chen, "Rotor design optimization of squirrel cage induction motor - part ii: Results discussion," *IEEE Transactions on Energy Conversion*, vol. 36, no. 2, pp. 1280–1288, 2021.

[172] J. Barta, N. Uzhegov, P. Losak, C. Ondrusek, M. Mach, and J. Pyrhönen, "Squirrel-cage rotor design and manufacturing for high-speed applications," *IEEE Transactions on Industrial Electronics*, vol. 66, no. 9, pp. 6768–6778, 2019.

[173] S. F. Contreras, C. A. Cortes, and M. A. Guzmán, "Modelling of squirrel cage induction motors for a bio-inspired multi-objective optimal design," *IET Electric Power Applications*, vol. 11, no. 4, pp. 512–523, 2017.

[174] M. J. Akhtar and R. K. Behera, "Optimal design of stator and rotor slot of induction motor for electric vehicle applications," *IET Electrical Systems in Transportation*, vol. 9, no. 1, pp. 35–43, 2019.

[175] Y. Li, G. Lei, G. Bramerdorfer, S. Peng, X. Sun, and J. Zhu, "Machine learning for design optimization of electromagnetic devices: Recent developments and future directions," *Applied Sciences*, vol. 11, no. 4, 2021. [Online]. Available: https://www.mdpi.com/2076-3417/11/4/1627

[176] N. Bianchi and S. Bolognani, "Design optimisation of electric motors by genetic algorithms," *IEE Proceedings - Electric Power Applications*, vol. 145, no. 5, pp. 475–483, Sep. 1998.

[177] M. E. Beniakar, A. G. Sarigiannidis, P. E. Kakosimos, and A. G. Kladas, "Multiobjective evolutionary optimization of a surface mounted pm actuator with fractional slot winding for aerospace applications," *IEEE Transactions on Magnetics*, vol. 50, no. 2, pp. 665–668, Feb 2014.

[178] G. Dajaku, W. Xie, and D. Gerling, "Reduction of low space harmonics for the fractional slot concentrated windings using a novel stator design," *IEEE Transactions on Magnetics*, vol. 50, no. 5, pp. 1–12, May 2014.

[179] A. Belahcen, F. Martin, M. E.-H. Zaim, E. Dlala, and Z. Kolondzovski, "Combined fe and particle swarm algorithm for optimization of high speed pm synchronous machine," *COMPEL - The international journal for computation and mathematics in electrical and electronic engineering*, vol. 34, no. 2, pp. 475–484, 2015. [Online]. Available: https://doi.org/10.1108/COMPEL-07-2014-0168

[180] C. A. Lopez and E. G. Strangas, "Optimization of pmsm performance with torque ripple reduction and loss considerations," in *2018 XIII International Conference on Electrical Machines (ICEM)*, Sep. 2018, pp. 899–905.

[181] W. Ouyang, D. Zarko, and T. A. Lipo, "Permanent magnet machine design practice and optimization," in *Conference Record of the 2006 IEEE Industry Applications Conference Forty-First IAS Annual Meeting*, vol. 4, Oct 2006, pp. 1905–1911.

[182] Y. Yang, S. M. Castano, R. Yang, M. Kasprzak, B. Bilgin, A. Sathyan, H. Dadkhah, and A. Emadi, "Design and comparison of interior permanent magnet motor topologies for traction applications," *IEEE Transactions on Transportation Electrification*, vol. 3, no. 1, pp. 86–97, March 2017.

[183] P. Di Barba, M. E. Mognaschi, N. Rezaei, D. Alister Lowther, and T. Rahman, "Many-objective shape optimisation of ipm motors for electric vehicle traction," *International Journal of Applied Electromagnetics and Mechanics*, vol. 60, pp. s1–s14, 05 2019.

[184] G. Lei, C. Liu, J. Zhu, and Y. Guo, "Techniques for multilevel design optimization of permanent magnet motors," *IEEE Transactions on Energy Conversion*, vol. 30, no. 4, pp. 1574–1584, 2015.

[185] D. Gope and S. K. Goel, "Design optimization of permanent magnet synchronous motor using taguchi method and experimental validation," *International Journal of Emerging Electric Power Systems*, vol. 22, no. 1, pp. 9–20, 2021. [Online]. Available: https://doi.org/10.1515/ijeeps-2020-0169

[186] S. Vaez-Zadeh and A. Ghasemi, "Design optimization of permanent magnet synchronous motors for high torque capability and low magnet volume," *Electric Power Systems Research*, vol. 74, no. 2, pp. 307–313, 2005. [Online]. Available: https://www.sciencedirect.com/science/article/pii/S0378779605000271

[187] X. Sun, Z. Shi, G. Lei, Y. Guo, and J. Zhu, "Analysis and design optimization of a permanent magnet synchronous motor for a campus patrol electric vehicle," *IEEE Transactions on Vehicular Technology*, vol. 68, no. 11, pp. 10 535–10 544, 2019.

[188] P. Barbaa, M. E. Mognaschi, R. Palka, P. Paplicki, and S. Szkolny, "Design optimization of a permanent-magnet excited synchronous machine for electrical automobiles," *International Journal of Applied Electromagnetics and Mechanics*, vol. 39, 09 2012.

[189] L. Yang, S. L. Ho, W. N. Fu, and W. Li, "Design optimization of a permanent magnet motor derived from a general magnetization pattern," *IEEE Transactions on Magnetics*, vol. 51, no. 11, pp. 1–4, 2015.

[190] J. Wang, X. Yuan, and K. Atallah, "Design optimization of a surface-mounted permanent-magnet motor with concentrated windings for electric vehicle applications," *IEEE Transactions on Vehicular Technology*, vol. 62, no. 3, pp. 1053–1064, 2013.

[191] J. Y. Alsawalhi and S. D. Sudhoff, "Design optimization of asymmetric salient permanent magnet synchronous machines," *IEEE Transactions on Energy Conversion*, vol. 31, no. 4, pp. 1315–1324, 2016.

[192] S. Günther, S. Ulbrich, and W. Hofmann, "Driving cycle-based design optimization of interior permanent magnet synchronous motor drives for electric vehicle application," in *2014 International Symposium on Power Electronics, Electrical Drives, Automation and Motion*, 2014, pp. 25–30.

[193] K. M. Cisse, S. Hlioui, M. Belhadi, G. Mermaz Rollet, M. Gabsi, and Y. Cheng, "Design optimization of multi-layer permanent magnet synchronous machines for electric vehicle applications," *Energies*, vol. 14, no. 21, 2021. [Online]. Available: https://www.mdpi.com/1996-1073/14/21/7116

[194] F. Parasiliti, M. Villani, S. Lucidi, and F. Rinaldi, "Finite-element-based multiobjective design optimization procedure of interior permanent magnet synchronous motors for wide constant-power region operation," *IEEE Transactions on Industrial Electronics*, vol. 59, no. 6, pp. 2503–2514, 2012.

[195] T. Song, Z. Zhang, H. Liu, and W. Hu, "Multi-objective optimisation design and performance comparison of permanent magnet synchronous motor for evs based on fea," *IET Electric Power Applications*, vol. 13, no. 8, pp. 1157–1166, 2019. [Online]. Available: https://ietresearch.onlinelibrary.wiley.com/doi/abs/10.1049/iet-epa.2019.0069

[196] Y. Ma, Y. Xiao, J. Wang, and L. Zhou, "Multicriteria optimal latin hypercube design-based surrogate-assisted design optimization for a permanent-magnet vernier machine," *IEEE Transactions on Magnetics*, vol. 58, no. 2, pp. 1–5, 2022.

[197] X. Sun, B. Wan, G. Lei, X. Tian, Y. Guo, and J. Zhu, "Multiobjective and multiphysics design optimization of a switched reluctance motor for electric vehicle applications," *IEEE Transactions on Energy Conversion*, vol. 36, no. 4, pp. 3294–3304, 2021.

[198] Q. Ma, A. EL-Refaie, and A. Fatemi, "Multi-objective design optimization of a blended permanent magnet assisted synchronous reluctance machine," in *2021 IEEE International Electric Machines Drives Conference (IEMDC)*, 2021, pp. 1–7.

[199] P. Asef, R. B. Perpiñà, M. R. Barzegaran, A. Lapthorn, and D. Mewes, "Multiobjective design optimization using dual-level response surface methodology and booth's algorithm for permanent magnet synchronous generators," *IEEE Transactions on Energy Conversion*, vol. 33, no. 2, pp. 652–659, 2018.

[200] P. Asef, R. B. Perpiñà, S. Moazami, and A. C. Lapthorn, "Rotor shape multi-level design optimization for double-stator permanent magnet synchronous motors," *IEEE Transactions on Energy Conversion*, vol. 34, no. 3, pp. 1223–1231, 2019.

[201] O. Ocak and M. Aydin, "An innovative semi-fea based, variable magnet-step-skew to minimize cogging torque and torque pulsations in permanent magnet synchronous motors," *IEEE Access*, vol. 8, pp. 210 775–210 783, 2020.

[202] I. Petrov, P. Ponomarev, Y. Alexandrova, and J. Pyrhönen, "Unequal teeth widths for torque ripple reduction in permanent magnet synchronous machines with fractional-slot non-overlapping windings," *IEEE Transactions on Magnetics*, vol. 51, no. 2, pp. 1–9, Feb 2015.

[203] T. Matsuo and T. A. Lipo, "Rotor design optimization of synchronous reluctance machine," *IEEE Transactions on Energy Conversion*, vol. 9, no. 2, pp. 359–365, June 1994.

[204] G. Pellegrino, F. Cupertino, and C. Gerada, "Automatic design of synchronous reluctance motors focusing on barrier shape optimization," *IEEE Transactions on Industry Applications*, vol. 51, no. 2, pp. 1465–1474, March 2015.

[205] F. Cupertino, G. Pellegrino, and C. Gerada, "Design of synchronous reluctance motors with multiobjective optimization algorithms," *IEEE Transactions on Industry Applications*, vol. 50, no. 6, pp. 3617–3627, Nov 2014.

[206] Y. Bao, M. Degano, S. Wang, C. Liu, H. Zhang, Z. Xu, and C. Gerada, "A novel concept of ribless synchronous reluctance motor for enhanced torque capability," *IEEE Transactions on Industrial Electronics*, pp. 1–1, 2019.

[207] A. Credo, G. Fabri, M. Villani, and M. Popescu, "Adopting the topology optimization in the design of high-speed synchronous reluctance motors for electric vehicles," *IEEE Transactions on Industry Applications*, vol. 56, no. 5, pp. 5429–5438, 2020.

[208] A. Credo, M. Villani, M. Popescu, and N. Riviere, "Synchronous reluctance motors with asymmetric rotor shapes and epoxy resin for electric vehicles," in *2019 IEEE Energy Conversion Congress and Exposition (ECCE)*, 2019, pp. 4463–4469.

[209] R. Moghaddam, "Novel rotor design optimization of synchronous reluctance machine for high torque density," *IET Conference Proceedings*, pp. 32–32(1), January 2012. [Online]. Available: https://digital-library.theiet.org/content/conferences/10.1049/cp.2012.0256

[210] B. Son, J. Kim, J. Kim, Y. Kim, and S. Jung, "Adaptive particle swarm optimization based on kernel support vector machine for optimal design of synchronous reluctance motor," *IEEE Transactions on Magnetics*, vol. 55, no. 6, pp. 1–5, June 2019.

[211] Y. Yamamoto, S. Morimoto, M. Sanada, and Y. Inoue, "Reduction of torque ripple in synchronous reluctance motor by combining different flux barrier structures," *IEEJ Journal of Industry Applications*, vol. 8, no. 3, pp. 430–436, 2019.

[212] C. López, T. Michalski, A. Espinosa, and L. Romeral, "Rotor of synchronous reluctance motor optimization by means reluctance network and genetic algorithm," in *2016 XXII International Conference on Electrical Machines (ICEM)*, 2016, pp. 2052–2058.

[213] Y. Hidaka and H. Igarashi, "Topology optimization of synchronous reluctance motors considering localized magnetic degradation caused by punching," *IEEE Transactions on Magnetics*, vol. 53, no. 6, pp. 1–4, 2017.

[214] H. Sasaki and H. Igarashi, "Topology optimization accelerated by deep learning," *IEEE Transactions on Magnetics*, vol. 55, no. 6, pp. 1–5, 2019.

[215] Y. Yamashita and Y. Okamoto, "Design optimization of synchronous reluctance motor for reducing iron loss and improving torque characteristics using topology optimization based on the level-set method," *IEEE Transactions on Magnetics*, vol. 56, no. 3, pp. 1–4, 2020.

[216] T.-H. Lee, J.-H. Lee, K.-P. Yi, and D.-K. Lim, "Optimal design of a synchronous reluctance motor using a genetic topology algorithm," *Processes*, vol. 9, no. 10, 2021. [Online]. Available: https://www.mdpi.com/2227-9717/9/10/1778

[217] Y. Otomo and H. Igarashi, "Topology optimization using gabor filter: Application to synchronous reluctance motor," *IEEE Transactions on Magnetics*, vol. 57, no. 6, pp. 1–4, 2021.

[218] J. Baek, S. S. R. Bonthu, and S. Choi, "Design of five-phase permanent magnet assisted synchronous reluctance motor for low output torque ripple applications," *IET Electric Power Applications*, vol. 10, no. 5, pp. 339–346, 2016.

[219] M. Barcaro, N. Bianchi, and F. Magnussen, "Permanent-magnet optimization in permanent-magnet-assisted synchronous reluctance motor for a wide constant-power speed range," *IEEE Transactions on Industrial Electronics*, vol. 59, no. 6, pp. 2495–2502, June 2012.

[220] Y. Wang, G. Bacco, and N. Bianchi, "Geometry analysis and optimization of pm-assisted reluctance motors," *IEEE Transactions on Industry Applications*, vol. 53, no. 5, pp. 4338–4347, Sep. 2017.

[221] C. López-Torres, A. Garcia, J. Riba, G. Lux, and L. Romeral, "Computationally efficient design and optimization approach of pma-synrm in frequent operating torque–speed range," *IEEE Transactions on Energy Conversion*, vol. 33, no. 4, pp. 1776–1786, Dec 2018.

[222] D. Mingardi and N. Bianchi, "Line-start pm-assisted synchronous motor design, optimization, and tests," *IEEE Transactions on Industrial Electronics*, vol. 64, no. 12, pp. 9739–9747, Dec 2017.

[223] Y. G. Woldesenbet, G. G. Yen, and B. G. Tessema, "Constraint handling in multiobjective evolutionary optimization," *IEEE Transactions on Evolutionary Computation*, vol. 13, no. 3, pp. 514–525, June 2009.

[224] K. Price, R. Storn, and J. Lampinen, *Differential Evolution: A Practical Approach to Global Optimization*, ser. Natural Computing Series. Springer, 2005.

[225] R. Storn and K. Price, "Differential evolution – a simple and efficient heuristic for global optimization over continuous spaces," *Journal of Global Optimization*, vol. 11, no. 4, pp. 341–359, Dec 1997. [Online]. Available: https://doi.org/10.1023/A:1008202821328

[226] S. Kirkpatrick, C. D. Gelatt, and M. P. Vecchi, "Optimization by simulated annealing," *Science*, vol. 220, no. 4598, pp. 671–680, 1983. [Online]. Available: https://science.sciencemag.org/content/220/4598/671

[227] A. K. Jain and R. C. Dubes, *Algorithms for Clustering Data*. Upper Saddle River, NJ, USA: Prentice-Hall, Inc., 1988.

[228] E. Zitzler and L. Thiele, "An evolutionary algorithm for multiobjective optimization: The strength pareto approach," 1998.

[229] I. Ono, H. Kita, and S. Kobayashi, *A Real-coded Genetic Algorithm using the Unimodal Normal Distribution Crossover*. Berlin, Heidelberg: Springer Berlin Heidelberg, 2003, pp. 213–237. [Online]. Available: https://doi.org/10.1007/978-3-642-18965-4_8

[230] R. Sarker and C. A. Coello Coello, *Assessment Methodologies for Multiobjective Evolutionary Algorithms*. Boston, MA: Springer US, 2002, pp. 177–195. [Online]. Available: https://doi.org/10.1007/0-306-48041-7_7

[231] E. Zitzler and L. Thiele, "Multiobjective evolutionary algorithms: a comparative case study and the strength pareto approach," *IEEE Transactions on Evolutionary Computation*, vol. 3, no. 4, pp. 257–271, Nov 1999.

[232] N. Riquelme, C. V. Lücken, and B. Baran, "Performance metrics in multi-objective optimization," in *2015 Latin American Computing Conference (CLEI)*, Oct 2015, pp. 1–11.

[233] C. M. Fonseca and P. J. Fleming, "On the performance assessment and comparison of stochastic multiobjective optimizers," in *Parallel Problem Solving from Nature — PPSN IV*, H.-M. Voigt, W. Ebeling, I. Rechenberg, and H.-P. Schwefel, Eds. Berlin, Heidelberg: Springer Berlin Heidelberg, 1996, pp. 584–593.

[234] H. Ishibuchi and T. Murata, "A multi-objective genetic local search algorithm and its application to flowshop scheduling," *IEEE Transactions on Systems, Man, and Cybernetics, Part C (Applications and Reviews)*, vol. 28, no. 3, pp. 392–403, Aug 1998.

Appendix A

Evolutionary algorithms for design optimization of electric machines

Three multiobjective metaheuristics, namely DE, SA, and GA, have been developed to solve winding design optimization problems. Herein, these algorithms are generically described. In the final part of this appendix a performance comparison of the algorithms is provided.

A.1 Constraints handling

There are several strategies for constraints handling: a simple approach is the reject strategy, which rejects infeasible individuals. This is conceivable if the infeasible space occupies a small portion of the objective functions landscape. Otherwise, relevant information that conveys the search towards global optima, which may be on the boundary between feasible and infeasible solutions, is discarded [45].

Instead of discarding infeasible individuals, a penalty strategy can be adopted, exploiting all individuals, by penalizing the evaluation functions with a weighted sum of the constraints violations, thus converting a constrained problem into an unconstrained one. The penalty mechanism can be *static* if the penalty weights are constant for the whole search, although the determination of such weights is problematic; or *dynamic* if the penalty weights are modified during the search. For example, the severity of the constraints violation may increase with time, by means of progressively increasing the penalty weights. Moreover, both mechanisms display two characteristics that may affect negatively the converge of the algorithm: the algorithm convergence is highly dependent on the weight parameters initial values; and they do not provide any search space sensitivity analysis feature that could enhance the algorithm convergence [45].

In this setting, a self-adaptive strategy gathers information from the individuals to determine the quantity of penalty to be added to the evolution functions, requiring no initial parameters to be tuned. The variant developed in [223] uses two penalty functions added to a distance function to deal with constraints. The distance value is calculated as

$$\mathrm{d}_i(x) = \begin{cases} v(x) & ,r_f = 0 \\ \sqrt{\widetilde{f}_i(x)^2 + v(x)^2} & ,\text{otherwise} \end{cases}, \tag{A.1}$$

where $r_f =$ number of feasible individuals / population size, $\widetilde{f}_i(x)$ is the i^{th} objective function normalized value of the x individual, which is calculated as

$$\widetilde{f}_i(x) = \frac{f_i(x) - f^i_{\min}}{f^i_{\max} - f^i_{\min}} \tag{A.2}$$

where $f_i(x)$ is the i^{th} objective function non-normalized value, and $f^i_{\min}$ and $f^i_{\max}$ are the minimum and maximum values of the i^{th} objective function values for the current population, respectively. The violation function $v(x)$ is given by

$$v(x) = \frac{1}{m}\sum_{j=1}^{m} \frac{c_j(x)}{c_j^{\max}}, \tag{A.3}$$

where $c_j(x)$ is the j-constraint violation severity for the individual x, and $c_j^{\max} = \max_x c_j(x)$.

The distance value introduces small penalties to the infeasible individual's fitness. Further penalization is obtained by a two penalty function. The first penalty function is based on the constraints violation severity, and the second is based on the objective functions, being formulated for the x individual of the i^{th} objective function as follows

$$\mathrm{p}_i(x) = (1 - r_f)\mathrm{X}_i(x) + r_f \mathrm{Y}_i(x), \tag{A.4}$$

where

$$\mathrm{X}_i(x) = \begin{cases} 0 & ,r_f = 0 \\ v(x) & ,\text{otherwise} \end{cases}, \tag{A.5}$$

and

$$\mathrm{Y}_i(x) = \begin{cases} 0 & ,\text{if } x \text{ feasible} \\ \widetilde{f}_i(x) & ,\text{otherwise} \end{cases}. \tag{A.6}$$

In (A.4), the balance between the two components is controlled by the number of feasible individuals in the current population. The two penalty mechanisms have two major purposes: (i) to further reduce the fitness of infeasible individuals, as the penalty added by the distance

function alone is small; (ii) to identify the best infeasible individuals in the population by adding different amounts of penalty to each infeasible individual's fitness. In addition, this mechanism has the following proprieties: (i) if there is no single feasible individual in the population ($r_f = 0$) the individuals are evaluated based on their constraint violation severity, thus preferring individuals which are closer to the feasible region and avoiding premature convergence; (ii) if there are feasible individuals in the population, then individuals with lower constraint violation severity and better objective function values are preferred, thus enhancing flexibility, by allowing for the contribution of infeasible individuals in the search for global optima; (iii) if there are no infeasible individuals in the population, then their fitness is based only on their objective functions values.

Finally, the fitness of an individual for the i^{th} objective function is calculated as the sum of the distance value and the two-penalty mechanism, thus

$$\mathrm{F}_i(x) = \mathrm{d}_i(x) + \mathrm{p}_i(x). \tag{A.7}$$

Some optimization problems may have their decision variables restrained within specific bounds, which is the case of the stator winding optimization problem.

Offspring generated by mutation and crossover operators, or other metaheuristic method, may fall out of bounds and, consequently, they have to be regenerated into the feasible region. For this purpose, the bounce-back reinitialization [224] is employed. This method randomly selects a value that lies between the base value and the bound being violated. Hence, the progress toward best values is taken into account.

A.2 Multiobjective differential evolution approach

Differential evolution is a metaheuristic with outstanding convergence performance and easy implementation to solve mainly continuous optimization problems. DE was originally proposed by Storn and Price [225]. The main idea of the real-coded DE is to apply vector differences to a current population of solutions to generate the offspring population, which is most commonly known as the mutant population.

As any evolutionary algorithm the initial population can be created randomly (uniformly distributed), although other strategies may be adopted such as sequential diversification and parallel diversification [45].

The classic crossover method generates a new offspring by randomly selecting one individual from the current population, or parent population, and by applying a weighted difference between two parents with a predefined probability. This mutation operator is

named DE/rand/1/bin: the base vector is selected randomly; one difference vector is applied; and the crossover scheme is an independent binomial experiment. Other mutation operators may be found in Table A.1.

Table A.1 Examples of mutation operators.

Mutation operator	**Description**
DE/rand/1/bin	$u_{i,j} = x_{r_1,j} + F \cdot \left(x_{r_2,j} - x_{r_3,j}\right)$
DE/best/1/bin*	$u_{i,j} = x_{r_{\text{best}},j} + F \cdot \left(x_{r_2,j} - x_{r_3,j}\right)$
DE/mean/1/bin	$u_{i,j} = \frac{1}{NP}\sum_{k=1}^{NP} x_{r_k,j} + F \cdot \left(x_{r_2,j} - x_{r_3,j}\right)$
DE/rand-to-best/1/bin*	$u_{i,j} = x_{r_1,j} + \lambda \cdot \left(x_{r_{\text{best}},j} - x_{r_1,j}\right) + F \cdot \left(x_{r_2,j} - x_{r_3,j}\right)$
DE/current-to-best/1/bin*	$u_{i,j} = x_{i,j} + \lambda \cdot \left(x_{r_{\text{best}},j} - x_{r_1,j}\right) + F \cdot \left(x_{r_2,j} - x_{r_3,j}\right)$
DE/rand/2/bin	$u_{i,j} = x_{r_1,j} + F_1 \cdot \left(x_{r_2,j} - x_{r_4,j}\right) + F_2 \cdot \left(x_{r_3,j} - x_{r_5,j}\right)$

Notes: * Not suited for multiobjective optimization. i is the i^{th} individuals of a population with NP individuals; j is the j^{th} dimension of the problem (the number of dimensions correspond to the number of decision variable); $x_{r_{1,\ldots,5}}$ are randomly selected vectors; and λ, F, F_1, and F_2 are scaling factors.

The replacement of solutions occurs when an offspring has better fitness than the parent (base vector).

The layout of the proposed multiobjective differential evolution (MODE) is described in Algorithm 3. The algorithm main procedures are briefly explained:

- **Algorithm inputs** - the algorithm requires the number of individuals NP, the problem dimension D (value equal to the number of decision variables), the scaling factor F, and the crossover probability C_r;
- **Algorithm initialization** - a random uniform distribution of NP individuals is generated to initialize the current population;
- **Stopping criterion** - several techniques may be adopted, such as the algorithm runs until a maximum number of iterations is met, or until the current population does not change for a specified number of iterations;
- **Mutation** - the mutant population is generated as described in Algorithm 3, lines 6 to 16, where $\mathcal{V}_{[0,1]}$ is a random uniformly distributed value in the interval $[0,1]$. The mutation operator is one which can be selected from Table A.1, and during this process some differential-vectors may fall out of bounds, thus the bounce-back reinitialization (Section A.1) is employed to deal with infeasibility;

- **Evaluation** - after all mutants have been generated, the two populations, current and mutant, are unified into $\mathcal{P}$, and the objective functions and constraints are evaluated. Infeasibility is solved by the self-adaptive technique described in Section A.1;

- **Replacement** - NP individuals from $\mathcal{P}$ are selected to move to the next iteration. In Algorithm 3, line 20, the selection$(I_f, \delta_k, \mathrm{R}, \mathcal{P}, N)$ function is the NSGA-II [48] based mechanism, which selects the individuals from $\mathcal{P}$ that occupy the first NP positions in the rank $\mathrm{R}(I_f, \delta_k)$. The ranking mechanism layout is described in Algorithm 4. It uses two indexes to sort the individuals: (i) *frontier index* (I_f), whose value increases as further frontiers of nondominated solutions are selected; (ii) *k-neighbor index* (δ_k) which for each individual the Euclidean distance to its nearest k^{th} neighbor, with equal I_f, is calculated, and the farthest individuals are indexed first. If two individuals are equally distanced, then one is selected randomly to be indexed first. Finally, the individuals are sorted by increasing I_f indexes, and then by increasing δ_k (Fig. A.1), thus preferring highly diversified nondominated solutions;

- **Algorithm termination** - Upon a successful termination of the algorithm, the resulting nondominated front is stored in $\mathcal{X}$. Then, the best compromise solution can be selected by the user, according to their design preferences.

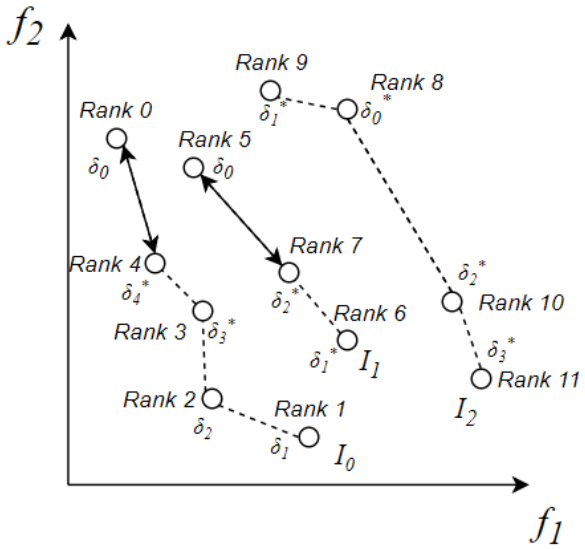

Figure A.1 Ranking mechanism for two objective functions (individuals ranked randomly are identified with *). Rank 0 means best individual and rank 11 means worst individual.

Algorithm 3 MODE optimizer

1: Inputs: F and $C_r \in [0,1]$, the population size NP, and the problem dimensions D

$\mathcal{X} \leftarrow$ random(NP) /* Generate the initial population */
$\mathcal{U} \leftarrow \emptyset(NP)$ /* Allocate the mutant population */
while stopping criterion not met **do**
    /* Mutation procedure */
    for $i \leftarrow 1$ up to NP **do**
        Select randomly base and differential vectors
        Select randomly $\delta \in \{1, ..., D\}$
        for $j \leftarrow 1$ up to D **do**
            if $\mathcal{V}_{[0,1]} \leq C_r \vee j = \delta$ **then** /* Crossover */
                $u_{i,j} \leftarrow$ mutate$(x_{i,j})$
            else
                $u_{i,j} \leftarrow x_{i,j}$
            end if
        end for
    end for
    /* End mutation procedure */
    $\mathcal{P} \leftarrow \mathcal{X} \cup \mathcal{U}$ /* Unify current and mutant populations */
    Evaluate $\mathcal{P}$ /* Evaluate individuals' fitness */
    $\mathcal{X} \leftarrow$ selection$(I_f, \delta_k, \mathrm{R}, \mathcal{P}, NP)$ /* NSGA-II based selection mechanism */
end while

Algorithm 4 NSGA-II based selection mechanism.

Inputs: $\mathcal{P}$ and N
$\mathcal{Q} \leftarrow \mathcal{P}$
$\mathcal{P} \leftarrow \emptyset$
while $\mathcal{Q} \neq \emptyset$ **do**
    $I \leftarrow \emptyset$
    for each $c \in \mathcal{Q}$ **do**
        Dominated $\leftarrow$ false
        for each $s \in \mathcal{Q}$ **do**
            if $s \prec c$ **then**
                Dominated $\leftarrow$ true
            end if
        end for
        if Dominated $=$ false **then**
            $I \leftarrow I \cup \{c\}$
        end if

```
16:     end for
17:     Q ← Q \ I
18:     for each i ∈ I do
19:         δ ← δ ∪ {distance_to_nearest_neighbour(i)}
20:     end for
21:     while δ ≠ ∅ do
22:         f ← k : max_k{δ_k}
23:         δ ← δ \ {δ_f}
24:         P ← P ∪ {I_f}
25:         if size(P) = N then
26:             return
27:         end if
28:     end while
29: end while
```

A.3 Multiobjective simulated annealing approach

Simulated annealing is a metaheuristic inspired on the physical annealing process applied to a material to obtain a state of low energy, i.e. a strong crystalline structure. This metaheuristic was introduced in [226]. Similarly to the metallurgic annealing, this stochastic technique set the objective function of the problem as a dynamic energy state system. Thus, an optimization problem's solution corresponds to a system state. The decision variables associated with a solution of the problem are analogous to the molecular positions. Finding a local minimum implies that a meta-stable state has been reached. Thus, escaping from sub-optimal states to find the global optima, means that the degradation of solutions may be allowed. The simulated annealing replacement scheme is based on the following criterion: moves which improve the cost functions are always accepted; otherwise, a neighbor solution is accepted with a given probability which depends on the system's energy, i.e. the temperature of the system at a given iteration. As the algorithm progresses, the probability of accepting dominated solutions decreases, in general.

Algorithm 5 shows the outline of the real-coded MOSA, which is based on the AMOSA algorithm. This algorithm requires, as initial parameters, the following information: HL the maximum size of the archive (which on termination is populated with nondominated solutions); SL the size which the archive is allowed to expand before reduced to the HL size; $T_{\max}$ the maximum (initial) temperature; $T_{\min}$ the minimum (final) temperature; $iter$ number

of iterations at a fixed temperature; α the SA cooling rate. The MOSA main procedures are explained next.

Firstly, the archive is populated with $\gamma \times SL (\gamma > 1)$ uniformly distributed random solutions, as previously described for the MODE. Then, each solution is refined by a hill-climbing procedure through a certain number of iterations, accepting a new solution only if it dominates the previous one. After that, only nondominated solutions are kept in the archive. If the number of the remaining solutions in the archive is larger than HL, a clustering technique is used to reduce the number of nondominated solutions to HL. In the original work [47], the clustering is used to promote diversity. The clustering technique employed is the single linkage algorithm [227], where the distance between two clusters corresponds to the length of the shortest link between them, which is similar to the clustering algorithm used in SPEA [228]. The purpose of the clustering technique is the aim of the mechanism that ranks solutions employed in MODE. Furthermore, the *k-neighbour index* used in this function is the same spread measure used in SPEA. Therefore, the clustering technique, herein employed, is the selection function described in Algorithm 4; however, only nondominated solutions are allowed to be selected (this is achieved by simply removing the outer while loop in Algorithm 4). In Algorithm 5 this mechanism has the selection $(I_f, \delta_k, \text{ND}, \text{Archive}, HL)$ notation. It is possible that at the termination of the archive initialization only one solution remains.

Secondly, the perturb is the perturbation function that generates a new individual by introducing small variations in the parameters of the decision variables, such that

$$\mathrm{x}_j = \mathrm{x}_j + p \cdot \mathcal{V}_{[-1,1]} \cdot \min\{\mathrm{x}_j - \mathrm{X}_j^{\mathrm{L}}, \mathrm{X}_j^{\mathrm{U}} - \mathrm{x}_j\}, j \in \{1, ..., D\}, \tag{A.8}$$

where p is the perturbation factor, $\mathrm{X}_j^{\mathrm{L}}$ and $\mathrm{X}_j^{\mathrm{U}}$ are the minimum and maximum acceptable values for the decision variable, respectively.

Finally, the probability of acceptance of a new solution is computed as proposed in the original work [47]. Thus, the acceptance probability is computed as a function of the amount of dominance between two solution a and b, which is given by

$$\Delta dom_{a,b} = \prod_{i=1, f_i(a) \neq f_i(b)}^{M} \left(\frac{|f_i(a) - f_i(b)|}{R_i} \right), \tag{A.9}$$

where M is the number of objective functions and R_i is the range of the i^{th} objective function. In the optimization problem here presented, the ranges of the objective functions is not known *a priori*. In this case, the objective functions values of the solutions in the archive along with the *parent* and *neighbour* are used to computing them.

Algorithm 5 MOSA optimizer.

Inputs: $T_{\max}$, $T_{\min}$, HL, SL, $iter$, α, p
$temp \leftarrow T_{\max}$
Initialize the Archive
$parent \leftarrow \text{random}(\text{Archive})$
while $temp > T_{\min}$ **do**
    for $i \leftarrow 1$ up to $iter$ **do**
        $neighbour \leftarrow \text{perturb}(parent)$ /* Mechanism of Eq. A.8 */
        Evaluate *neighbour* and check its dominance status w.r.t. *parent*
        if *parent* dominates *neighbour* **then**
            $\Delta dom_{\text{avg}} \leftarrow \frac{\left(\sum_{i=1}^{k} \Delta dom_{i,neighbour}\right) + \Delta dom_{parent,neighbour}}{k+1}$
            /* k is the no of solutions in the Archive which dominate *neighbour* */
            $prob \leftarrow \frac{1}{1+exp(\Delta dom_{\text{avg}} \cdot temp)}$
            $parent \leftarrow neighbour$, with probability = $prob$
        end if
        if *parent* and *neighbour* are non-dominating to each other **then**
            Check the dominance status of *neighbour* w.r.t. Archive
            if *neighbour* is dominated by $k \geq 1$ solutions of Archive **then**
                $\Delta dom_{\text{avg}} \leftarrow \frac{\sum_{i=1}^{k} \Delta dom_{i,neighbour}}{k}$
                $prob \leftarrow \frac{1}{1+exp(\Delta dom_{\text{avg}} \cdot temp)}$
                $parent \leftarrow neighbour$, with probability = $prob$
            end if
            if *neighbour* is non-dominated w.r.t. all solutions of Archive **then**
                $parent \leftarrow neighbour$ and $\text{Archive} \leftarrow \text{Archive} \cup \{neighbour\}$
                if $\text{size}(\text{Archive}) > SL$ **then**
                    $\text{Archive} \leftarrow \text{selection}(I_f, \delta_k, \text{ND}, \text{Archive}, HL)$
                end if
            end if
            if *neighbour* dominates $k \geq 1$ solutions of Archive **then**
                $parent \leftarrow neighbour$ and $\text{Archive} \leftarrow \text{Archive} \cup \{neighbour\}$
                Remove all k dominated solutions from Archive
            end if
        end if
        if *neighbour* dominates *parent* **then**
            Check the dominance status of *neighbour* w.r.t. Archive
            if *neighbour* is dominated by $k \geq 1$ solutions of Archive **then**

36: $\Delta dom_{\min} \leftarrow \min(\Delta dom_{neighbour,i}), i \in \{1,...,k\}$
37: $prob \leftarrow \frac{1}{1+exp(-\Delta dom_{\min})}$
38: Set solution of Archive which corresponds to $\Delta dom_{\min}$ as *parent*, with probability = *prob*, else *parent* $\leftarrow$ *neighbour*
39: **end if**
40: **if** *neighbour* is non-dominated w.r.t. all solutions of Archive **then**
41: If *parent* is in the Archive, remove it from the Archive
42: *parent* $\leftarrow$ *neighbour* and Archive $\leftarrow$ Archive $\cup \{neighbour\}$
43: **if** size(Archive) $> SL$ **then**
44: Archive $\leftarrow$ selection$(I_f, \delta_k, \text{ND}, \text{Archive}, HL)$
45: **end if**
46: **end if**
47: **if** *neighbour* dominates $k \geq 1$ solutions of Archive **then**
48: *parent* $\leftarrow$ *neighbour* and Archive $\leftarrow$ Archive $\cup \{neighbour\}$
49: Remove all k dominated solutions from Archive
50: **end if**
51: **end if**
52: **end for**
53: $temp \leftarrow temp \cdot \alpha$
54: **end while**
55: **if** size(Archive) $> SL$ **then**
56: Archive $\leftarrow$ selection$(I_f, \delta_k, \text{ND}, \text{Archive}, HL)$
57: **end if**

A.4 Multiobjective genetic algorithm approach

Genetic Algorithms were originally developed in the 1970s to replicate the adaptive processes of biological systems in the optimization domain [45]. In 1980s, GAs have been applied to solve optimization problems and rapidly became a very popular class of EAs. The traditional form of decision variables representation is binary-coded, although others types of representation are also possible. The main idea behind GA is to apply a crossover operator to two or more solutions (parents), which usually are of major relevance. Then, a mutation operator that randomly modifies the individuals' contents is employed to enhance diversity. The selection of individuals is originally based on a proportional probabilistic scheme. The replacement is generational, i.e. the parent population is replaced by the offspring population, after each generation (iteration), even if parents have higher fitness. Traditionally, the

crossover operator is based on the n-point or uniform crossover [45], while the mutation is bit flipping. The crossover and mutation operators are executed with fixed probabilities.

The layout of the multiobjective genetic algorithm (MOGA) [45] developed is described in Algorithm 6.

The inputs of this approach are the maximum number of individuals per generation NP and the elite size $Elite$, which is the number of individuals allowed to survive to the next generation (elitism), such that $Elite < NP$.

The algorithm initialization consists of the generation of NP uniformly distributed random individuals, which are stored in $\mathcal{X}$ and evaluated.

Inside the main loop $Elite$, individuals from the $\mathcal{X}$ population are ranked and selected by the NSGA-II mechanism (Algorithm 4), and stored in the surviving population ($\mathcal{S}$). Thereafter, offspring are generated and stored in $\mathcal{S}$, while the surviving population has less than NP individuals. The main loop is executed until a stopping criterion is met.

The offspring generation is made through the crossover and mutation operators, both requiring a certain number of parents from $\mathcal{S}$. The parent selection is made by the stochastic universal sampling (SUS). Thereby, an outer roulette wheel is placed around a pie chart, where individuals with better fitness occupy larger slices, thus having higher chance to be selected. Considering f_i as the fitness function of the i^{th} individual in the $\mathcal{S}$ population, the probability of that individual to be selected is calculated by

$$p_i = \frac{f_i}{\sum_{j=1}^{\text{size}(\mathcal{S})} f_j}, \tag{A.10}$$

where f_i, for this case, is calculated considering the individuals *frontier index* (I_f), such that higher values of fitness are attributed to individuals with lower I_f values. In the SUS strategy, a single spin of the roulette allows for the selection of the desired number of individuals, through uniformly spaced pointers.

The crossover scheme generates two offspring by swapping, with a given probability, the representation of two parents. The mutation operator employs the same mechanism for solution perturbation developed for MOSA (A.8).

The crossover and mutation operators' probabilities (P_{c} and P_{m}) are modified at the end of each generation, by a self-adaptive technique which gathers information from the current population. This operation takes into account the maximum number of solutions that dominate the solution or solutions quantified with the highest frontier index ($I_f^{\max}$). When $I_f^{\max}$ is high, the probability for crossover is also higher, resulting in a rough way of generating new solutions (offspring may be positioned farther from their parents, exploring different regions of the objective function landscape). Otherwise, if $I_f^{\max}$ is low the probability for

mutation is higher. In this case, a more refined scheme of generating offspring is obtained, by applying small perturbations to the parents. Thereby, the crossover and mutation operators' probabilities are calculated by

$$\begin{cases} P_{\mathrm{c}} = 1 - 1/I_f^{\max} \\ P_{\mathrm{m}} = 1/I_f^{\max} \end{cases}, I_f^{\max} \geq 1. \tag{A.11}$$

Furthermore, the geometric operator unimodal normal distribution crossover (UNDX) [229] was applied, as an alternative scheme for the crossover operator. In a briefly manner, the UNDX generates new solutions within a centroid with normal distribution whose shape depends on the positions of the parents. The two crossover methods were tested for the winding design optimization problem. Surprisingly, the UNDX showed poorer performance. A justification may be due to the few number of offspring generated in each generation for this problem.

Algorithm 6 MOGA optimizer.

Inputs: N, $Elite$
$P_{\mathrm{c}} \leftarrow P_{\mathrm{m}} \leftarrow 0.5$
$\mathcal{X} \leftarrow \mathrm{random}(N)$ /* Generate the initial population */
Evaluate $\mathcal{X}$
while stopping criterion not met **do**
    $\mathcal{S} \leftarrow \mathrm{selection}(I_f, \delta_k, \mathrm{R}, \mathcal{X}, Elite)$
    while $\mathrm{size}(\mathcal{S}) < N$ **do**
        $\mathcal{P} \leftarrow \mathrm{SUS\_roulette}(\mathcal{S})$
        if $\mathcal{V}_{[0,1]} \leq P_{\mathrm{c}}$ **then**
            $\mathcal{P} \leftarrow \mathrm{crossover}(\mathcal{P})$
        end if
        if $\mathcal{V}_{[0,1]} \leq P_{\mathrm{m}}$ **then**
            $\mathcal{P} \leftarrow \mathrm{mutation}(\mathcal{P})$
        end if
        Evaluate and rank $\mathcal{P}$; $\mathcal{S} \leftarrow \mathcal{S} \cup \mathcal{P}$
    end while
    $\mathcal{X} \leftarrow \mathcal{S}$
    Update the P_{c} and P_{m} operators probabilities
end while

A.5 Performance analysis

The winding design optimization problem introduced in [145] is used as the performance comparison analysis benchmark test. For performance assessment the following metrics are used.

Efficient Set Space (ESS) [230] and *Hypervolume* [231]. The ESS indicator is used to evaluate the spread of the solutions in the non-dominated front. Smaller values mean that the solutions are distanced uniformly to their closest neighbors, and therefore are better distributed. The hypervolume measures the space of the dominated solutions (an area for two-dimensional problems), where higher values mean better performance. This indicator is the most used performance metric [232]. *Statistical Interpolation* (SI) [233] is used to statistically comparing different algorithms instead of comparing only scalar values. It is calculated by the sum of linear segments of a dominant attainment surface of a given algorithm, then divided by the length of the total dominant attainment surface. Non-parametric statistical procedures can be applied to assess which algorithm outperforms the other. *Purity* [234, 47] calculates the fraction between the number of non-dominated solutions and the total number of solutions that result from the unified set of solutions found at the end of each run for a given algorithm. A value near to 1 means better performance, since more solutions contributed to the unified non-dominated front.

The four winding configurations are the following: **Z96P8M3** with 4 decision variables, 9.057 % and 990 of initial airgap MMF THD and winding wire length, respectively, and 3418801 possible combinations. The input parameters of MODE are a scaling factor of 0.8, a crossover probability of 0.9, and 10 individuals, running for a total of 100 generations. The input parameters of MOSA are an initial temperature of 100, final temperature of 10×10^{-9}, a cooling factor of 0.8, an archive size of 5, expandable up to 10, a perturbation factor of 0.05 (same for all winding configurations) and 10 iterations at a fixed temperature. The number of individuals of MOGA is 20, running for 100 generations (the elite size is always half the current population size, and it has always the double of individuals of MODE). In this approach, the geometric operator showed weaker performance, with respect to the crossover operator, thereby the last one and the mutation operator were employed in MOGA. **Z48P4M3** with 4 decision variables, 8.584 % and 459 of initial airgap MMF THD and winding wire length, respectively, and 6765201 possible combinations. The input parameters are the same of the previous winding configuration, except that the number of generations and iterations are 200 and 20, respectively for MODE/MOGA and MOSA. **Z24P2M3** with 6 decision variables, 9.057 % and 933 of initial airgap MMF THD and winding wire length, respectively, and 6.32752E12 possible combinations. The number of generations for MODE and MOGA is 400, with a population size of 20 and 40, for MODE and MOGA, respectively. The

MOSA has an archive size of 10, expandable up to 20, and 60 iterations at fixed temperature. **Z9628M3** with 16 decision variables, 4.921 % and 2150 of initial airgap MMF THD and winding wire length, respectively, and 2.03805E35 possible combinations. The number of generations for MODE and MOGA is 1800. The number of iterations of MOSA at a fixed temperature is 250. All the remaining parameters are equal to the previous winding configuration.

Each algorithm was executed 20 times and the final fronts of each running were unified. Then the dominated solutions were removed from this new set (Fig. A.2). Thereafter, the results of the performance comparison analysis are provided in Table A.2.

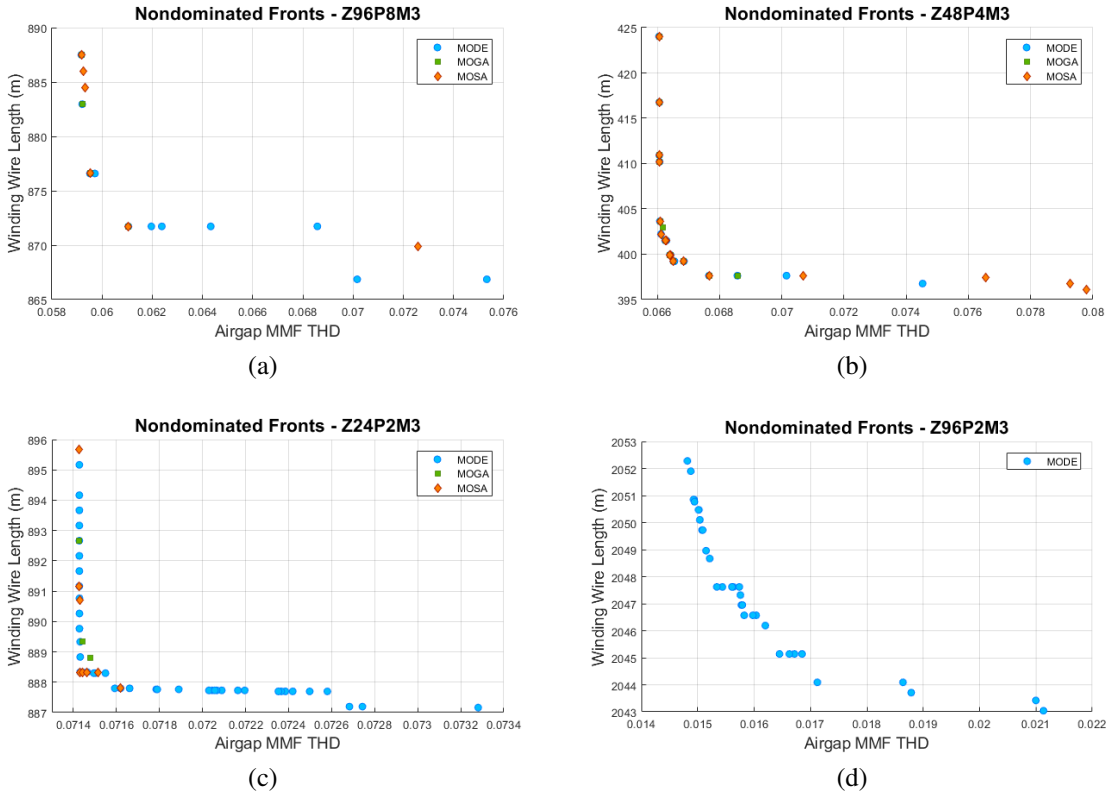

Figure A.2 Final nondominated fronts of each mutation variation obtained for the (a) Z96P8M3, (b) Z48P4M3, (c) Z24P2M3, and (d) Z96P2M3 windings.

From the results of Table A.2, it is clear that MODE is superior for practically all metrics. Concerning the SI metric, MODE outperformed the other algorithms for three winding configurations, except the Z48P4M3 where MOSA was superior. Furthermore, MODE was the single optimizer to generate the Pareto front of the Z96P2M3, which is the largest combinatorial problem here solved. With respect to the ESS and hypervolume metrics,

Table A.2 Comparative performance analysis for the optimizers.

Winding	Optimizer	SI	ESS	Hypervolume	Purity
Z96P8M3	MODE	**0.482**	**0.0007**	**0.317**	**92/200**
	MOSA	0.116	0.3784	0.206	24/60
	MOGA	0	0.9035	0.020	29/200
Z48P4M3	MODE	0.08	0.0778	0.225	**127/200**
	MOSA	**0.509**	0.0111	**0.379**	41/85
	MOGA	0.012	**0.0000**	0.065	57/200
	MODE	**0.875**	**0.0270**	**0.015**	**333/400**
Z24P2M3	MOSA	0.041	1.2401	0.001	13/74
	MOGA	0.005	0.3080	0.000	4/400
Z96P2M3	MODE	**1**	**0.1474**	**0.057**	**35/400**

MODE was also superior, denoting high diversification of the solutions generated. Regarding the purity metric, MODE was always superior followed by MOSA.

Considering the execution time of each algorithm (Table A.3), the results were similar in terms of computation speed. The MOGA is the fastest algorithm, but it is outperformed by the other algorithms, from the SI metric point of view.

Table A.3 Execution times of the three algorithms.

Winding	Arithmetic mean (s)			Standard deviation (s)		
	MODE	MOSA	MOGA	MODE	MOSA	MOGA
Z96P8M3	5.354	6.643	**4.423**	0.114	**0.088**	0.089
Z48P4M3	5.356	**3.889**	4.828	**0.073**	0.163	0.107
Z24P2M3	12.184	13.405	**11.369**	0.152	**0.115**	0.264
Z96P2M3	184.928	193.236	**175.7**	**3.086**	11.880	7.227